University of Alberta

Efficient Data Acquisition, Transmission and Post-Processing for Quality Spiral Magnetic Resonance Imaging

by

Jean-David Jutras

A thesis submitted to the Faculty of Graduate Studies and Research
in partial fulfillment of the requirements for the degree of

Master of Science
in
Medical Physics

Department of Oncology

Fall 2011
Edmonton, Alberta

Abstract

Spiral Magnetic Resonance Imaging (MRI) has traditionally presented more technical and computational challenges compared to its traditional Cartesian counterpart, notably a susceptibility to blurring artifacts, especially when scan parameters are non-optimal, and a heavier computational load both at the image reconstruction, and post-processing level. This research is aimed at improving the efficiency of data acquisition, transmission and post-processing for spiral MRI, which continues to become a more common sequence choice in applications where speed, signal-to-noise ratio and geometrical accuracy are key requirements. In the first part of this thesis, we cover the fundamentals of spiral trajectory design and acquisition, image reconstruction by means of fast Gaussian gridding, and a rapid method for deblurring a large *in vivo* dataset. In the second part, we introduce a novel technique for compressing spiral MR data acquired from a multi-channel coil array, with applications in wireless transmission and data storage. The compressed images are indistinguishable from the originals even though the data has been compressed by a factor of 3 or more.

Acknowledgements

I would like to first thank my supervisor Dr. Nicola DeZanche for his continuous support and guidance throughout this project. Thank you also to every other member of my supervisory committee, including Dr. Richard Thompson, Dr. Keith Wachowicz and Dr. B. Gino Fallone for the feedback provided throughout the project. I am also grateful to Dr. B. Gino Fallone as director of the Medical Physics Department, Cross Cancer Institute, for providing access to a Philips 3T Achieva MRI scanner. Thank you also to Dr. Atiyah Yahya, Dr. Keith Wachowicz and Philips Healthcare for the technical assistance in operating the scanner.

Contents

List of Tables

List of Figures

List of Symbols

$\lvert\uparrow\rangle$	spin-up
$\lvert\downarrow\rangle$	spin-down
α	flip angle, or dimensionless parameter
AP	artifact power
B_0	static magnetic field strength
$\mathbf{B}$	magnetic field strength vector
$\boldsymbol{B}_1^+$	time-varying transmit magnetic field
$\boldsymbol{B}_1^-$	time-varying receive magnetic field
BW	bandwidth
γ	gyromagnetic ratio
DR	dynamic range
δ	Dirac-delta function
Δ	difference in a given quantity
e	Euler's number ($= 2.718$)
$\boldsymbol{E}$	electric field
ϵ	electromagnetic force
f	frequency, or function
F	Fourier-transform of function f
FOV	field-of-view
$\boldsymbol{G}$	gradient strength
Γ	Gaussian kernel
$\mathbf{H}$	Hamiltonian
$\hbar$	reduced Planck constant
i	imaginary number ($= \sqrt{-1}$)
I	image
I_0	zeroth-order modified Bessel function

j	indexing variable
J	number of spiral turns
$\boldsymbol{J}$	conduction current
κ	spatial frequency space
k	number of bits, or indexing variable
K	constant, or number of κ-space samples
k_B	Boltzmann constant
L_{acq}	acquisition matrix size
M	downsampling factor
$\boldsymbol{M}$	net magnetization
m	magnetic moment induced in the receiver coil, or number of bits
$\boldsymbol{\mu}$	magnetic dipole moment matrix or vector
N	number of points
N_I	number of interleaves
NEX	number of experiments (a.k.a. number of averages)
$\boldsymbol{\psi}$	noise correlation matrix
ψ	monotonically-increasing function
Ψ	intrinsic coil SNR, or Kaiser-Bessel window
σ	noise standard deviation
ϕ	phase
$\boldsymbol{r}$	position vector
R	resistance (or real part of the impedance)
$\boldsymbol{S}$	spin angular momentum matrix
S, s	signal
t	time
τ	time or windowing parameter
T	thermodynamic temperature
T_{acq}	acquisition time
T_{scan}	total scan time
T_{tda}	total data acquisition time
T_E	echo-time
T_R	repetition time
T_1	spin-lattice relaxation constant
T_2	spin-spin relaxation constant
V	voxel size
W	sampling density compensation function, or probability of spin transition
ω	angular frequency
ω_0	Larmor angular frequency
x, y, z	spatial coordinates
χ	wave function

List of Abbreviations

ACR MRAP	American College of Radiology Magnetic Resonance Accreditation Phantom
AD	Analog Device
ADC	Analog-to-Digital Conversion
AP	Artifact Power
CT	Computed Tomography
CPR	Conjugate Phase Reconstruction
DC	Direct Current
DR	Dynamic Range
DFT	Discrete Fourier Transform
EPI	Echo-Planar Imaging
FOV	Field-of-View
FT	Fourier Transform
FFT	Fast Fourier Transform
FSORC	Frequency-Segmented Off-Resonance Correction
GRE	Gradient-Recalled Echo, a.k.a. Gradient Echo
MIP	Maximum Intensity Projection
MRI	Magnetic Resonance Imaging
MR	Magnetic Resonance
MSPS	Mega Sample Per Second
NMR	Nuclear Magnetic Resonance
NUFFT	Non-Uniform Fast Fourier Transform
RTP	Radiation Treatment Planning
PSF	Point-Spread Function
RF	Radio-Frequency
RSS	Root-Sum-of-Squares
SNR	Signal-to-Noise Ratio
SENSE	SENSitivity Encoding
UTE	Ultra-Short Echo-Time

CHAPTER 1

Overview of the Thesis

1.1 Motivation for the Project

Traditionally, Computed Tomography (CT) has been a 3D imaging modality of choice in many branches of medicine, partly because it provides useful images with high signal-to-noise ratio (SNR) and satisfactory contrast, but also because it is still available at a lower cost, is more user-friendly and has fewer contraindications than Magnetic Resonance Imaging (MRI). In recent years, however, MRI has rivaled the use of CT in certain applications of neurology and oncology, by virtue of its superior soft-tissue contrast, and its ability to display physiological information [1–4]. Furthermore, although traditionally bone has been difficult to image with MRI, new pulse sequences and hardware have been designed which now enable the visualization of bone, and the measurement of bone density [5], even permitting the diagnosis of dental cavities [6], thus leaving little behind that only CT can perform. Nevertheless, MRI is not about to replace CT in all areas of diagnostic imaging, because it cannot compete in terms of imaging speed, SNR and accuracy [7, 8]. Accuracy refers to how geometrically similar an image resembles the actual object, without taking random noise and spatial resolution into account. Geometrical distortions and artifacts degrade the accuracy of an image, by showing features that are distorted, blurred, or that do not exist in the object being imaged. As demonstrated in Tab. 1.1, for a given field-of-view (FOV) and pixel resolution, the intrinsic physics of MRI require a trade-off between imaging speed, SNR and accuracy. Consider for example a simple Cartesian gradient-echo image (to be discussed in the next chapter). We may achieve higher SNR by acquiring the whole dataset twice, and averaging the signal, which increases the scan time, but does not affect the accuracy; alternatively, we can decrease the sampling bandwidth so as to boost the SNR by the same amount, which does not affect the scan time substantially, but

Speed	SNR	Accuracy	Protocol
low	low	high	h-BW GRE
low	high	low	l-BW GRE
high	low	low	EPI

Table 1.1: Intrinsic trade-offs between imaging speed, SNR and geometrical accuracy in MRI, assuming the same repetition time T_R. Three protocols are given as an example: a highest-bandwidth gradient-echo (h-BW GRE), a lowest-bandwidth gradient-echo (l-BW GRE) and an echo-planar imaging (EPI) sequence.

causes the geometrical accuracy to deteriorate. Consequently, much MRI research is aimed at improving at least one of these three things.

In this thesis, I investigate how spiral MRI may be made efficient at three important levels: data acquisition, transmission and post-processing. A new technique of data compression is also explored, which could potentially enable the transmission of MRI data from a high-density detector array through a single wireless link, such as the presently-available IEEE 802.11n protocol. I use a gradient-echo spiral pulse sequence throughout the thesis, for three basic reasons. First, spiral MRI is one of the most efficient (ratio of total data acquisition time to the total scan time) sampling trajectories presently available [1, p.928]. In general, the more dead-time a sequence contains, such as the time needed to rewind the phase-encode gradient, the less efficient it is. Secondly, a spiral trajectory leads to an isotropic point-spread function (PSF) which does not cause sequence-dependent spatial distortions [1], but may instead require image post-processing to correct for blurring. Finally, non-Cartesian imaging is expected to become more prominent in the future, especially with the recent proliferation of Ultra-short echo-time (UTE) MRI, which enables the visualization of the musculoskeletal system and bone [9]. Techniques applied to spiral MRI are also applicable to other non-Cartesian pulse sequences, such as radial acquisitions used in UTE-MRI.

1.2 Organization of the Thesis

This thesis consists of three main chapters. Chapter 2 covers the basic theory of MRI physics behind modern MRI, serving as general background for the rest of the thesis.

Chapter 3 covers the advanced theory of data acquisition, image reconstruction and post-processing of spiral MRI in details, demonstrating how high-resolution, artifact-free images may be obtained provided that certain considerations are met. An important feature of this chapter includes a fast and reliable technique for deblurring a large spiral MR dataset, which is applicable to any situation where resolution and geometrical accuracy is crucial,

e.g., MRI-based Radiation Treatment Planning (RTP). Finally this chapter also serves as relevant background for the material presented in chapter 4.

Chapter 4 focuses on efficient data transmission, being motivated by the present technological race towards large multi-detector arrays. While parallel imaging with high-density arrays may be the key to speeding up MRI acquisition, it comes with its own set of challenges, which includes dealing with the bulkiness and interference of multi-coil coaxial cables, increased data memory and processing time. The bulkiness of multiple coaxial wires has motivated research in using digital wireless links or optical links on coils. Philips Healthcare have already manufactured an on-coil digitizer combined with a fiber-optical link (branded "DirectDigital RF" technology) as part of their new Ingenia MRI scanner, which is expected to improve image SNR by up to 40% (visit: http://www.healthcare.philips.com/us_en/products/mri/systems/Ingenia30T/index.wpd). As shown in Tab. 1.2, existing wireless links do not achieve sufficiently high data rates required by large multi-channel arrays at present. For instance, consider a typical sampling rate of 1000 samples taken in 5 ms for one channel (200 kHz bandwidth), each sample occupying 16 bits of memory for each of the real and imaginary part, as calculated in Eq. (1.1), this yields a data-rate requirement of 6.4 Megabits per second per channel used:

$$\frac{1000 \text{ samples/channel}}{5 \times 10^{-3} \text{ s}} \times 16 \text{ bits/samples} \times 2 = 6.4 \text{ Mbits/s/channel}. \tag{1.1}$$

Thus, given the presently-available IEEE 802.11n standard, and assuming that the digitized data from multiple MRI channels are combined prior to transmission over a single wireless link, 23 channels (= 147 Mbit/s) could be theoretically supported by the system. However, high-density arrays of up to 128 channels have been tested and found beneficial [10–12]. Also, the unconventional environment within the MRI suite (e.g., a large static magnetic field strength, and reflective walls shielded with copper) means that realistic transmission rates could be further reduced. The chapter presents a novel technique for compressing the data to be transmitted from a high-density array to the computer reconstruction console by up to a factor of 4, resulting in a potential increase in the maximum number of supported channels to 92, using typical 802.11n rates.

Wireless Standard	Theoretical max data-rate (Mbits/s)	Typical data-rate (Mbits/s)	Max # channels supported
IEEE 802.11a-1999	54	22	3
IEEE 802.11b-1999	11	6	1
IEEE 802.11g-2003	54	19	3
IEEE 802.11n-2009	600	**150**	23
WiMedia Alliance UWB	480	110	17

Table 1.2: List of wireless protocols with relevant specifications (see: http://en.wikipedia.org/wiki/IEEE_802.11#ref_80211ns_sgiB2 & http://en.wikipedia.org/wiki/Wireless_USB). Maximum number of supported MRI channels is calculated according to Eq. (1.1), assuming the typical data rate.

CHAPTER 2

Theory of Magnetic Resonance Imaging

2.1 History

Magnetic Resonance Imaging (MRI) is a field that grew out of the discovery of Nuclear Magnetic Resonance (NMR) by I. I. Rabi in 1938 [13]. In 1946, F. Bloch and E. M. Purcell applied the technique to liquids and solids, and successfully explained NMR as the precession of spins about a magnetic field [14]. R. R. Ernst improved the sensitivity of the NMR technique by means of RF pulses instead of the previously-used continuous-wave excitation method, and also applied the Fourier transform to analyze the MR signal [15]. The idea of using NMR to detect tumors *in vivo* came from the physician R. V. Damadian in 1971, when he observed that tumors in mice exhibited different MR relaxation constants compared to the healthy tissues [16]. Finally, the invention of the modern MRI scanner is attributed to P. C. Lauterbur and P. Mansfield in the 1970s, following their use of linear gradient magnetic fields to spatially encode an image in 2D [17, 18]. MRI scanners became commercially available in the 1980s. Well-known companies of today that manufacture whole-body MRI scanners include: General Electric, Philips, Siemens, Varian and Toshiba.

2.2 Nuclear Magnetic Resonance

2.2.1 The Concept of Spin

Elementary particles carry an intrinsic angular momentum called *spin*. The most common value of spin quantum number is that of particles that make up ordinary matter, including protons, neutrons and electrons, and consists of two eigenstates: spin up ($+1/2$) or down

$(-1/2)$ [19]. Isotopes that contain an odd number of protons and/or neutrons have a magnetic dipole moment and angular momentum, with a non-zero spin, which comes as a multiple of 1/2 (e.g. 1/2, 1, 3/2, etc). The most common such isotope found in nature is hydrogen (H_0^1), which makes it particularly well-suited for performing NMR. The magnetic dipole moment $\boldsymbol{\mu}$ is proportional to the spin angular momentum $\mathbf{S}$

$$\boldsymbol{\mu} = \gamma \boldsymbol{S}, \tag{2.1}$$

where the proportionality constant γ is called the *gyromagnetic ratio* ($\gamma = 2.675 \times 10^8$ rad $s^{-1}T^{-1}$ for protons). When a magnetic field interacts with a nucleus that exhibit magnetic dipole moment, it will exert a torque $\boldsymbol{\mu} \times \boldsymbol{B}$ on the dipole, with associated energy given by

$$H = -\boldsymbol{\mu} \cdot \boldsymbol{B} = -\gamma \boldsymbol{B} \cdot \boldsymbol{S}. \tag{2.2}$$

Without the presence of such a magnetic field, each proton spin is in an indeterminate sate, which means that its wave function is a linear combination of both the up state $|\uparrow\rangle = \begin{pmatrix} 1 \\ 0 \end{pmatrix}$ with eigenvalue $+\frac{\hbar}{2}$ and the down state $|\downarrow\rangle = \begin{pmatrix} 0 \\ 1 \end{pmatrix}$ with eigenvalue $-\frac{\hbar}{2}$, where $\hbar = 1.05 \times 10^{-34}$ J s, the reduced Planck constant. However, in the presence of a static magnetic field, each proton spin will collapse to one of the two possible states, one being parallel and the other being antiparallel to the magnetic field direction. The energy difference between the two states is

$$\Delta E = \gamma \hbar B_0. \tag{2.3}$$

All interactions of the proton spin with a magnetic field may be modelled from a quantum-mechanical point-of-view by means of the three Pauli spin matrices [19]:

$$\sigma_x = \begin{pmatrix} 0 & 1 \\ 1 & 0 \end{pmatrix}, \ \sigma_y = \begin{pmatrix} 0 & -i \\ i & 0 \end{pmatrix}, \ \sigma_z = \begin{pmatrix} 1 & 0 \\ 0 & -1 \end{pmatrix}, \tag{2.4}$$

one for each coordinate n, and the spin operator $\boldsymbol{S}_n = \hbar \sigma_n / 2$. To illustrate the simplest case, where a proton spin is subject to a static magnetic field along the z-direction ($\boldsymbol{B} = B_0 \hat{z}$), the wavefunction $\chi(t)$ of the spin obeys the Schrödinger equation [19]

$$i\hbar \frac{\partial \chi}{\partial t} = -\gamma B_0 \boldsymbol{S}_z \chi = -\frac{\gamma \hbar B_0}{2} \begin{pmatrix} 1 & 0 \\ 0 & -1 \end{pmatrix} \chi. \tag{2.5}$$

2.2.2 The Larmor Frequency

The general solution to Eq. 2.5 is the wave function of the proton spin given by

$$\chi(t) = a|\uparrow\rangle e^{i\gamma B_0 t/2} + b|\downarrow\rangle e^{-i\gamma B_0 t/2} = \begin{pmatrix} ae^{i\gamma B_0 t/2} \\ be^{-i\gamma B_0 t/2} \end{pmatrix}, \tag{2.6}$$

and subject to the normalization requirement $|a|^2 + |b|^2 = 1$, and initial condition $\chi(0) = \begin{pmatrix} a \\ b \end{pmatrix}$. Now letting $a = \cos(\alpha/2)$ and $b = \sin(\alpha/2)$, and solving for the expectation values $\langle\mu_z\rangle$, $\langle\mu_y\rangle$, and $\langle\mu_x\rangle$, we obtain

$$\langle\mu_z\rangle = \frac{\gamma\hbar}{2}\cos(\alpha), \tag{2.7}$$

$$\langle\mu_y\rangle = -\frac{\gamma\hbar}{2}\sin(\alpha)\sin(\gamma B_0 t), \tag{2.8}$$

$$\langle\mu_x\rangle = \frac{\gamma\hbar}{2}\sin(\alpha)\cos(\gamma B_0 t). \tag{2.9}$$

These equations basically model a magnetic moment vector $\boldsymbol{\mu}$ precessing about the z-axis at an azimuthal angle α and with a frequency

$$\omega_0 = \gamma B_0, \tag{2.10}$$

known as the Larmor frequency, as shown in Fig. 2.1 [19].

2.2.3 Probability Distribution of Nuclear Spin States

The population equilibrium of the proton spins within a magnetic field is given by the Boltzmann distribution

$$\frac{|\downarrow\rangle}{|\uparrow\rangle} = \exp\left(-\frac{\Delta E}{k_B T}\right) \approx 1 - \frac{\Delta E}{k_B T}, \tag{2.11}$$

where k_B is the Boltzmann constant, T is the thermodynamic temperature, and ΔE is the energy difference between the two spin states. Given a room temperature of 293 K, and a magnetic field strength B_0 of 3 T, the ratio of the two spin states will be

$$\frac{|\downarrow\rangle}{|\uparrow\rangle} = 1 - \frac{(2.675\times10^8)(1.05\times10^{-34})(3)}{(273)(2.38\times10^{-23})} = 1 - 4.32\times10^{-6}, \tag{2.12}$$

indicating that there is a slight excess of spins that point along the direction of the field. This spin excess is responsible for creating a net magnetization on the macroscopic scale, along the direction of the magnetic field denoted by $\sum \boldsymbol{\mu_{excess}} = \boldsymbol{M}$.

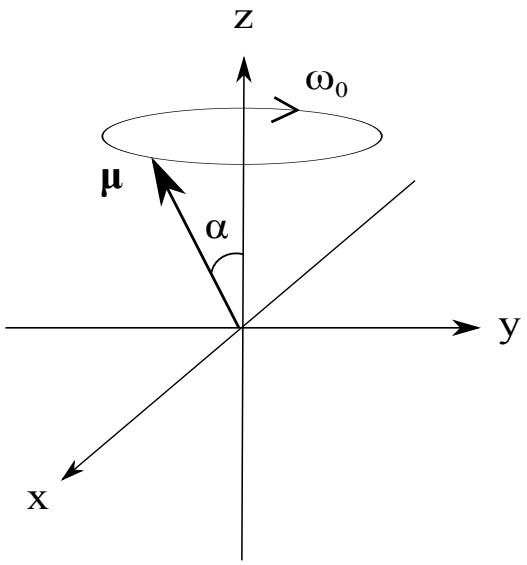

Figure 2.1: Precession of $\boldsymbol{\mu}$ in a uniform magnetic field. Although only the parallel configuration is shown here, the anti-parallel case is an equally valid solution, where $\alpha > 90^\circ$

2.2.4 Spin-Lattice Relaxation

Transitions of the spins from the +1/2 state to the -1/2 state and vice versa do occur due to the coupling of the spins to another system called the *lattice*, but which may be better thought as a reservoir, since it is equally applicable to liquids. One may think of a single proton as existing inside the energy reservoir. The energy shared between the proton and the reservoir must remain unchanged, such that if the proton spin undergoes an energy loss (from $1 \rightarrow 2$), the reservoir must also undergo an energy gain (from $b \rightarrow a$). However, the reservoir and the proton cannot both undergo an energy gain or loss, since that would violate conservation of energy. If we denote the probability per second of an upward transition as $W_\uparrow$ and that of a downward transition as $W_\downarrow$, a simple derivation by Slichter [20] reveals that the sum of both probabilities equals a constant

$$W_\downarrow + W_\uparrow = \frac{1}{T_1}, \tag{2.13}$$

known as the longitudinal, or spin-lattice relaxation constant T_1. This relaxation only affects the net magnetization that points along the z-direction. Thus if the net magnetization is perturbed from equilibrium M_0 by a certain means (to be seen in the following section), it will tend to return to its original position, in the direction parallel to the static magnetic

field, according to

$$\frac{dM_z}{dt} = \frac{M_0 - M_z}{T_1}. \tag{2.14}$$

Typical values for this longitudinal relaxation ranges *in vivo* from $\sim$ 220 ms for bone to $\sim$ 5600 ms for celebrospinal fluid at 3 T, and also increases with the static field strength B_0. (Values at 1.5 T range from $\sim$ 150 ms for bone to $\sim$ 4500 ms for celebrospinal fluid).

2.2.5 Radio-frequency Pulse Excitation

From classical mechanics, a time-varying magnetic field applies a torque on the net magnetization vector $\boldsymbol{M}$, according to

$$\frac{d\boldsymbol{M}}{dt} = \gamma \boldsymbol{M} \times \boldsymbol{B}. \tag{2.15}$$

If the magnetic field contains both a static component B_0 that points along z, and a transverse time-varying component $\boldsymbol{B}_1^+(t)$ along x and y, according to

$$\boldsymbol{B} = B_1(t)\left(\cos(\omega_{rf}t)\hat{\boldsymbol{x}} - \sin(\omega_{rf}t)\hat{\boldsymbol{y}}\right) + B_0\hat{\boldsymbol{z}}, \tag{2.16}$$

a change of coordinate system by taking the x-axis in the rotating frame along the $\boldsymbol{B}_1^+(t)$ direction yields

$$\frac{d\boldsymbol{M}}{dt} = \boldsymbol{M} \times \left[(\gamma B_0 - \omega_{rf})\hat{\boldsymbol{z}} + \gamma B_1(t)\hat{\boldsymbol{x}}\right]. \tag{2.17}$$

Equation (2.17) reveals that a time-varying magnetic field $B_1^+(t)$ with carrier frequency $\omega_{rf} = \gamma B_0$ can flip the magnetization onto the xy-plane. Defining $\Delta\omega = \gamma B_0 - \omega_{rf}$ and expanding Eq. (2.17) into three scalar equations, we obtain [1]

$$\frac{dM_x}{dt} = \Delta\omega M_y, \tag{2.18}$$

$$\frac{dM_y}{dt} = \gamma B_1(t) M_z - \Delta\omega M_x, \tag{2.19}$$

$$\frac{dM_z}{dt} = -\gamma B_1(t) M_y. \tag{2.20}$$

An important solution to Eqs. 2.20 involves the case of perfect on-resonance excitation where $\Delta\omega = 0$, with initial conditions $M_x(0) = 0$, $M_y(0) = 0$, and $M_z(0) = M_0$ for which the solution is [1]

$$M_x(t) = 0, \tag{2.21}$$

$$M_y(t) = M_0 \sin(\alpha(t)), \tag{2.22}$$

$$M_z(t) = M_0 \cos(\alpha(t)), \tag{2.23}$$

where $\alpha(t) = \gamma \int_0^t B_1(\tau)d\tau$, and is known as the *flip angle*.

2.2.6 Spin-Spin Relaxation

After being flipped along the x-axis, the magnetization M_x decays exponentially due to another mechanism of relaxation called spin-spin relaxation, denoted by the constant T_2. Slichter [20, p.34] explains that this second type of relaxation arises from the interaction of spins among themselves, where each nucleus experiences a local magnetic field $B_{loc} \sim \mu/r^3$ originating from its neighbors, located at an average distance r, and either aiding or opposing the static field B_0. If all the nuclei were precessing in phase at $t = 0$, there would be a time τ at which the net magnetization M_x would have been greatly reduced, such that $\gamma B_{loc}\tau \approx 1$. Thus the order of magnitude of the spin-spin relaxation constant is estimated by [20]

$$T_2 \sim \frac{1}{\gamma B_{loc}} = \frac{r^3}{\gamma^2 \hbar}, \tag{2.24}$$

and the transverse component M_{xy} of the magnetization relaxes according to

$$\frac{dM_{xy}}{dt} = -\frac{M_{xy}}{T_2}. \tag{2.25}$$

The subscript "xy" indicates that the transverse relaxation may lie anywhere on the xy-plane, and not necessarily along the x or y-axis alone.

In MRI, however, the static magnetic field B_0 is never perfectly homogeneous, resulting in an additional dephasing of the spins in the xy-plane. Assuming that the local field inhomogeneity also leads to an exponential decay, with a relaxation rate constant of T_2', the combined decay constant becomes [14, p.57]

$$\frac{1}{T_2^*} = \frac{1}{T_2} + \frac{1}{T_2'}. \tag{2.26}$$

An important difference between the dephasing arising from T_2 and T_2' is that the spins dephased by the T_2' component may be rephased by means of a second RF pulse that flips the magnetization by 180 degrees as shown in Fig. 2.2. This technique is known as a *spin echo*.

2.2.7 The Bloch Equations

All the previous effects of RF excitation and relaxation of the net magnetization may be incorporated into a set of three differential equations (one for each of the x, y, and z spatial

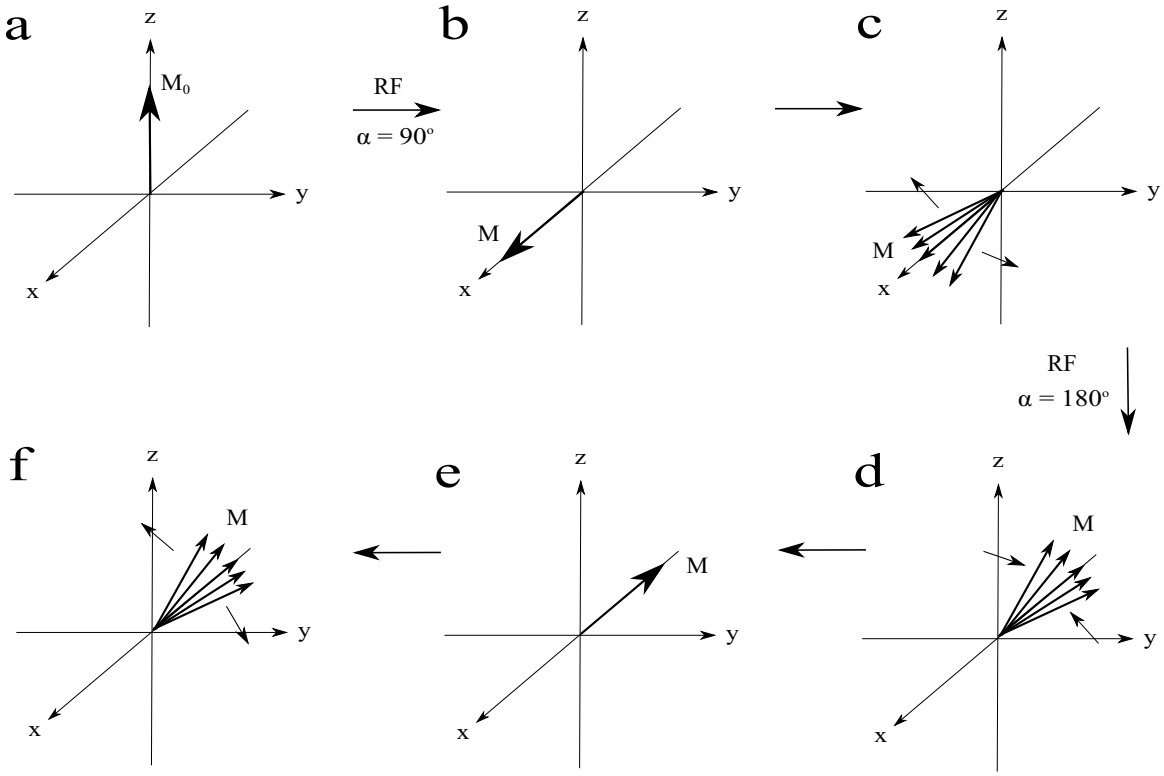

Figure 2.2: A spin echo illustrated in the rotating frame of reference: (a) The magnetization originally points along the static magnetic field direction. (b) A 90° RF pulse has flipped all the magnetization into the +x direction. (c) After a short time, individual spins have dephased because of the static field inhomogeneities, decreasing the net magnetization vector in the xy-plane. (d) A 180° RF pulse has flipped the spins into the -x direction, causing the spins to start refocussing. (e) An echo is formed as the spins have fully refocussed. (f) Following the echo, the spins will dephase again. The effect of spin-spin relaxation is not shown here, but would result in the net magnetization vector in (e) to be shorter than in (b).

component) which were originally derived by Felix Bloch, hence called the Bloch Equations [1]

$$\frac{d\boldsymbol{M}}{dt} = \gamma \boldsymbol{M} \times \boldsymbol{B} - \frac{M_x \hat{\boldsymbol{x}} + M_y \hat{\boldsymbol{y}}}{T_2} - \frac{(M_0 - M_z)\,\hat{\boldsymbol{z}}}{T_1}. \tag{2.27}$$

Equation (2.27) can be extended to account for other effects such as molecular self-diffusion.

2.2.8 Signal Detection

Once the net magnetization of a sample has been flipped into the xy-plane by a RF pulse, it will induce an electromagnetic force (voltage) ϵ within a conducting loop positioned in its vicinity, according to

$$\epsilon = \oint \frac{d}{dt} \left(\boldsymbol{M} \cdot \boldsymbol{B}_1^- \right) d^3 r, \tag{2.28}$$

where $\boldsymbol{M} = M_x \hat{\boldsymbol{x}} + M_y \hat{\boldsymbol{y}}$ is the rotating magnetization in the xy-plane, and $\boldsymbol{B}_1^-$ is the receive sensitivity of the probe [14]. Thus an NMR experiment consists of flipping a portion of the magnetization into the xy-plane by means of an RF pulse, sent by a transmitter probe, and then receiving the signal from the net rotating magnetization in the xy-plane with a receiver probe before it has fully decayed due to spin-spin relaxation. Certain probes are designed to serve as both transmitters and receivers, while other probes are only used for receiving the signal. High-density multi-channel surface coil arrays (see e.g., [10–12]) are an example of probes used only for signal reception.

2.3 The Physics of Magnetic Resonance Imaging

2.3.1 Linear Magnetic Field Gradients for Spatial Encoding

MRI basically consists of using the same method of RF excitation followed by a signal reception as in NMR, except that the signal received is also spatially-encoded (that is, assigned a position in space), rather than merely consisting of a volume average. In order to spatially-encode the signal transmitted and received, linear magnetic field gradients are utilized, one for each spatial coordinate (x, y, and z), such that the resulting gradient field is

$$\boldsymbol{G}(t) = G_x(t)\hat{\boldsymbol{x}} + G_y(t)\hat{\boldsymbol{y}} + G_z(t)\hat{\boldsymbol{z}}, \tag{2.29}$$

where

$$G_x = \frac{\partial B_z}{\partial x}, \quad G_y = \frac{\partial B_z}{\partial y}, \quad G_z = \frac{\partial B_z}{\partial z}. \tag{2.30}$$

Hence, the frequency of the rotating magnetization at a given point in time and space, will no longer be equal to the Larmor frequency ω_0, except at the system's origin. The frequency

of the rotating magnetization at a point (x, y, z) is now given by

$$\omega(x, y, z, t) = \gamma \left| \boldsymbol{B}(x, y, z, t) \right| \simeq \gamma \left(B_0 + \boldsymbol{G}(t) \cdot \boldsymbol{r} \right), \tag{2.31}$$

and the phase accumulation becomes

$$\phi(x, y, z, t) = \gamma B_0 t + \left[\gamma \int_0^t \boldsymbol{G}(\tau) d\tau \right] \cdot \boldsymbol{r}. \tag{2.32}$$

The quantity $\left(\gamma \int_0^t \boldsymbol{G}(\tau) d\tau \right)$ is commonly interpreted as the position in spatial frequency space [21] and is denoted in this thesis by $\boldsymbol{\kappa}(t)$.

2.3.2 The Imaging Equation

The MR signal $S(t)$ received by the coil within the imaging region of the MRI scanner is given by the *imaging equation*:

$$S(t) = e^{-i\omega_0 t} \int_V m(\boldsymbol{r}) e^{-i\boldsymbol{\kappa}(t)\cdot\boldsymbol{r}} d^3 r. \tag{2.33}$$

Sometimes, the $e^{-i\omega_0 t}$ term is included as part of the signal such that $S(t) = S'(t) e^{i\omega_0 t}$, where $S'(t)$ is the time-domain signal received by the RF coil, and ω_0 is the demodulation frequency, which is usually set equal to the Larmor frequency. The volume V over which the integration takes place is the excited slice, where at least a portion of the net magnetization has been flipped into the xy-plane, and $m(\boldsymbol{r})$ is the complex intensity distribution, which is proportional to the proton spin density, if the effects of relaxation are ignored.

2.3.3 The Fourier Transform

Image reconstruction in MRI consists of inverting the imaging equation to recover the quantity $m(\boldsymbol{r})$, which is proportional to the image intensity of a voxel at point $\boldsymbol{r}$. This inversion is performed by means of the Fourier transform (FT) or its inverse (FT^{-1}), defined analytically as

$$FT\{f(\boldsymbol{r})\} = F(\boldsymbol{\kappa}) = \frac{1}{2\pi} \int_{-\infty}^{\infty} f(\boldsymbol{r}) e^{-i\boldsymbol{\kappa}\cdot\boldsymbol{r}} d\boldsymbol{r}, \tag{2.34}$$

$$FT^{-1}\{F(\boldsymbol{\kappa})\} = f(\boldsymbol{r}) = \int_{-\infty}^{\infty} F(\boldsymbol{\kappa}) e^{+i\boldsymbol{\kappa}\cdot\boldsymbol{r}} d\boldsymbol{\kappa}, \tag{2.35}$$

where $\boldsymbol{\kappa}$ is the spatial frequency vector of the signal (with units [rad/m]) and $\boldsymbol{r}$ is the position vector (with units [m]). In Cartesian MRI, where the signal $S(t)$ is sampled on a uniform grid in κ-space (at regular intervals of $\Delta\boldsymbol{\kappa}$ along both the κ_x and κ_y directions), we may readily convert $S(t)$ into $S(\boldsymbol{\kappa})$. Taking the inverse Fourier transform of $S(\boldsymbol{\kappa})$, we obtain:

$$m(\boldsymbol{r}) = \int_{-\infty}^{\infty} S(\boldsymbol{\kappa}) e^{i\boldsymbol{\kappa}\cdot\boldsymbol{r}} d\boldsymbol{\kappa}. \tag{2.36}$$

Image processing, however, relies on digitized signal, which in turn requires a discrete version of Eq. (2.36). Given a vector of N uniformly-spaced complex data points $[d] = [d_0, d_1, d_2, ..., d_{N-1}]$ (such as a row of voxels in Fourier space), the j^{th} element of the discrete transform is given by [1]

$$DFT\{[d]\}_j = D_j = \frac{1}{N}\sum_{k=0}^{N-1} d_k e^{-i\frac{2\pi jk}{N}}, \quad j = 0, 1, 2, ..., N-1. \tag{2.37}$$

Similarly, the k^{th} element of the inverse discrete Fourier transform is given by

$$DFT^{-1}\{[D]\}_k = D_k = \sum_{j=0}^{N-1} d_k e^{+i\frac{2\pi jk}{N}}, \quad k = 0, 1, 2, ..., N-1. \tag{2.38}$$

For a list the analytical and the discrete Fourier transform properties, refer to Bernstein [1, pp.12-14]. In modern computer software (e.g., MATLAB), the discrete Fourier transform is typically computed by means of a fast algorithm known as the fast Fourier transform (FFT). Thus image reconstruction of Cartesian data can proceed very quickly.

2.3.4 Slice Selection

While the integral of a RF pulse envelope determines the flip angle α, the carrier frequency and the bandwidth of the pulse are responsible in turn for the slice location and thickness, respectively, when a gradient is applied along a direction orthogonal to the slice. For example, if we want to excite a transverse slice at a position z_c from the origin, a gradient along z with magnitude G_z must be applied, and the RF pulse transmitted must have a carrier frequency given by

$$\omega_{rf} = \gamma\left(B_0 + G_z z_c\right). \tag{2.39}$$

The slice thickness Δz is proportional to the bandwidth BW_{rf} of the pulse, which is given by

$$BW_{rf} = \frac{1}{\Delta t_{rf}} = \frac{\gamma}{2\pi} G_z \Delta z, \tag{2.40}$$

for a square pulse of duration Δt_{rf}, or by

$$BW_{rf} = \frac{N_L + N_R}{\Delta t_{rf}} = \frac{\gamma}{2\pi} G_z \Delta z, \tag{2.41}$$

for a sinc pulse of duration Δt_{rf}, where N_L and N_R are the number of left-side and right-side zero-crossings with respect to the central lobe. Because a sinc pulse must be transmitted in a finite time, some ringing will occur at the edges of the slice excitation profile, unless an apodization window is applied to the sinc pulse. A very short pulse in the time domain, will possess a large corresponding bandwidth in the frequency domain, and excite a thick slab of magnetization, while a longer pulse in the time domain will excite a thin slice. Sinc and square pulses (a.k.a. hard pulses) are two types of pulses commonly used in MRI. Hard pulses may be applied with or without a slice-selection gradient, such as in 3D volume acquisitions (i.e., 3D MRI), while sinc pulses are always accompanied by a slice-selection gradient followed by a rephasing gradient lobe. The rephasing gradient lobe, which is the shaded lobe in Fig. 2.3 is necessary to overcome the effect of phase dispersion of the spins along the slice thickness due to the finite time required to play out the RF pulse. The area under the rephasing lobe A_R is related to the *isodelay* Δt_I, according to [1, p.75]

$$G_z \Delta t_I + \frac{G_z r_z}{2} = A_R, \tag{2.42}$$

where r_z is the length of the gradient ramp, as shown in Fig. 2.3. The phase dispersion across the slice thickness $\Delta\phi$ may be written in terms of the isodelay Δt_I [1, p.272], such that

$$\Delta\phi = \gamma G_z \Delta z \Delta t_I. \tag{2.43}$$

The isodelay usually corresponds to the time elapsed from the peak to the end of the RF pulse.

2.3.5 Cartesian κ-space Sampling

Theoretically, there exits an infinite number of ways of sampling the κ-space signal, including random-walk sampling patterns, although in practice we are constrained by the gradient performance. However, the simplest and most common sampling trajectory uses separate frequency and phase encoding in the two Cartesian directions. The advantage of this method is that the samples are uniformly distributed over a grid in κ-space, and the images can be reconstructed by means of simple FFTs using Eqs. (2.37, 2.38). Frequency encoding occurs when the G_x gradient is applied during the readout, causing the frequency of the spins to vary along the field-of-view in the x direction (FOV_x) according to $\omega = \gamma G_x FOV_x$, while phase encoding takes place when the G_y gradient is applied prior to the acquisition, causing

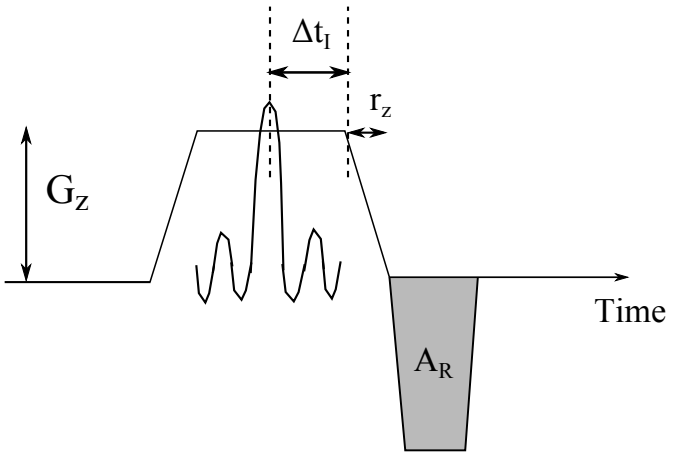

Figure 2.3: Relation between the slice-selective gradient lobe of strength G_z and the rephasing lobe (shown in gray) with respect to the sinc pulse location, and its isodelay Δt_I and ramp r_z. Adapted from [1, pp.75-76]

the phase of all the spins within the slice to be incremented by $\Delta\phi = \gamma FOV_y \int G_y(t)dt$. Because phase is periodic, it follows that the phase difference between two adjacent phase-encode lines must obey

$$\Delta\phi_y = \gamma \Delta G_y \frac{FOV_y}{2} \tau \leq \pi, \tag{2.44}$$

and the phase difference between two adjacent frequency-encode samples must be

$$\Delta\phi_x = \gamma G_x \frac{FOV_x}{2} \Delta t \leq \pi, \tag{2.45}$$

where $\Delta G_y \tau = \int G_y(t)dt$, and τ is the length of the square gradient pulse, and Δt is the time difference between two samples. The maximum frequency is $f_{max} = \frac{\gamma}{2\pi} G_x \frac{FOV_x}{2}$, and the sampling frequency is $f_s = N/T_{acq} = 1/\Delta t$, where N is the number of samples. Consequently, the sampling frequency must obey the relation

$$f_s \geq 2 f_{max} = \mathrm{BW}_s, \tag{2.46}$$

which means that the sampling frequency must be greater or equal to the signal bandwidth BW_s. The frequency at which it is equal to the signal bandwidth is known as the *Nyquist* rate. The concept of the Nyquist criterion may also be derived from the theory of the discrete Fourier transform. If the sampling frequency is less than the Nyquist rate, aliasing will occur, which means that the signal will fold-over from one end to the opposite end of the FOV. In order to prevent aliasing along the phase-encode direction, not only must the gradient pulse increments $\Delta G_y \tau$ be carefully chosen according to Eq. (2.44), but the object must also be fully contained within FOV_y. To avoid aliasing along the frequency-encode

direction, each interleaf is filtered by means of an anti-aliasing (low-pass) filter.

Figure 2.4 shows a typical Cartesian gradient-echo pulse sequence with the corresponding κ-space trajectory. In the trajectory shown, an interleaf corresponds to acquiring a horizontal line of samples in κ-space, starting at the bottom ($\kappa_{y_{min}}$) and moving towards the top ($\kappa_{y_{max}}$). Each interleaf begins with an RF excitation pulse, and ends with a spoiler gradient along the slice direction that dephases the remaining transverse magnetization in the slice. Two important time parameters that are part of any pulse sequence are the echo-time T_E, which is the time from the middle of the RF pulse to the point at which the centre of κ-space is traversed, and the repetition time T_R, which is defined as the time between the RF excitation pulses.

Another common type of Cartesian sampling trajectory known as echo-planar imaging (EPI) is shown in Fig. 2.5. In this sequence, several lines of κ-space are read within a single interleaf. A single-shot EPI sequence can also be devised, where desired κ-space samples are read following a single RF pulse excitation. Among all the types of Cartesian sequences, EPI is the most susceptible to image distortions, because of the low equivalent bandwidth in the phase-encode direction, allowing for more dephasing than the gradient-echo example in Fig. 2.4.

2.3.6 Factors that Affect the Signal-to-Noise Ratio

The signal-to-noise ratio (SNR) in Cartesian MR images is given by [22]

$$\mathrm{SNR} = \Psi \frac{V\sqrt{N_x N_y \mathrm{NEX}}}{F\sqrt{\mathrm{BW}_s}}, \tag{2.47}$$

where Ψ is the intrinsic SNR of the receiver coil, V is the voxel volume, N_x and N_y are the number of frequency samples and phase-encoding steps, respectively, NEX is the number of experiments (image repetitions), BW_s is the signal bandwidth and F is the system noise figure ($F \geq 1$) [22]. The noise figure is the ratio of input SNR to output SNR into the system's electronics. The SNR at the coil, given as the ratio of signal voltage v_s to the root-means-square (RMS) noise voltage v_n is

$$\Psi = \frac{v_s}{v_n} = \frac{\omega_0 \mu \left| \boldsymbol{B}_1^- \cdot \boldsymbol{M} \right|}{\sqrt{4k_B T R}} \propto \frac{B_1}{\sqrt{R}}, \tag{2.48}$$

where R is the real part of the input impedance (the resistance), T is the thermodynamic temperature, k_B is the Boltzmann constant, ω_0 is the Larmor frequency and μ is the magnetic permeability of the sample. Since $T_{acq} = N_x/\mathrm{BW}_s$, and the total data acquisition time is $T_{tda} = N_y T_{acq} \mathrm{NEX}$, for a given coil and MRI scanner, Eq. (2.47) may be simplified

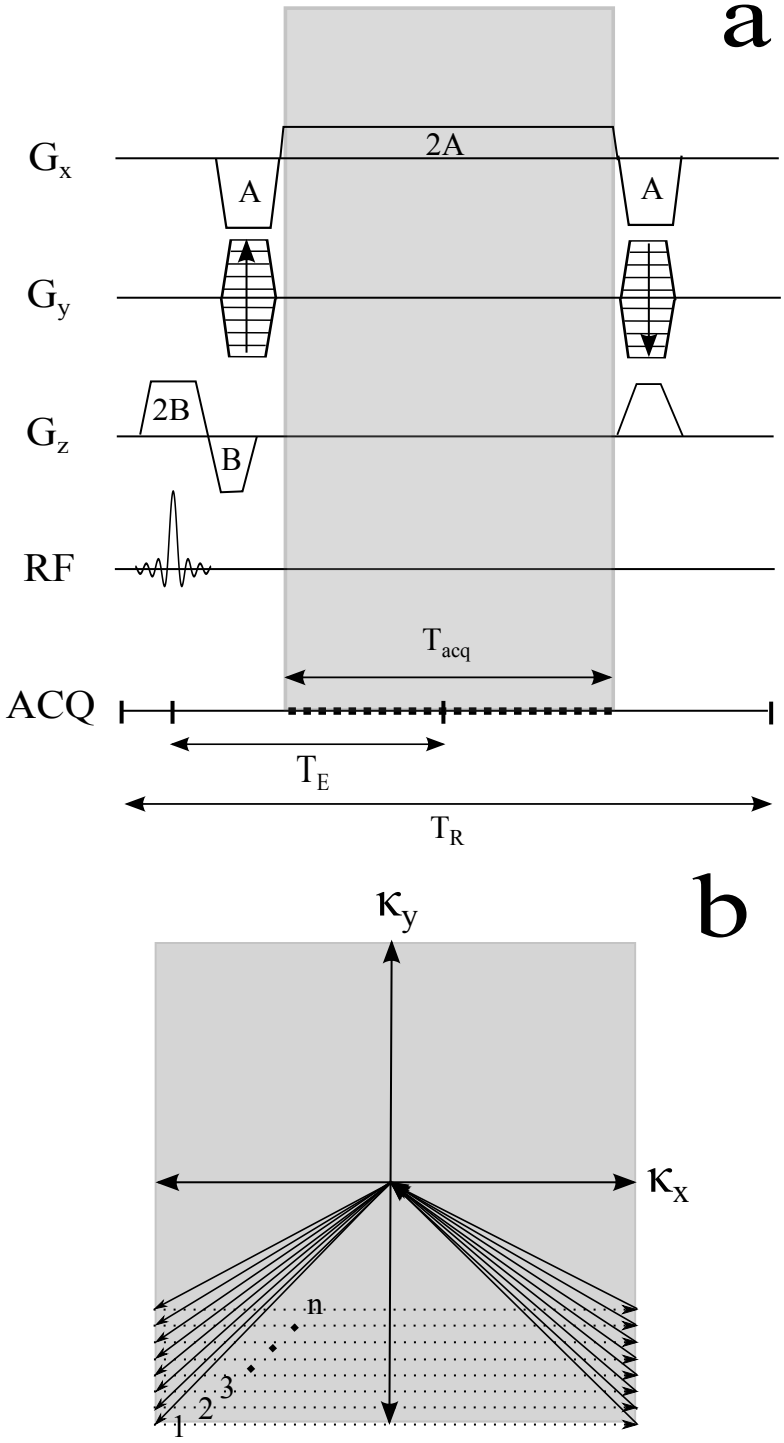

Figure 2.4: (a) A typical 2D gradient-echo pulse sequence for a transverse slice (in the xy-plane), including the rewinding and spoiling gradients, and showing the relative areas (A and B) under the gradient pulses. (b) The corresponding sampling trajectory for the gradient-echo sequence in (a). (Not drawn to scale).

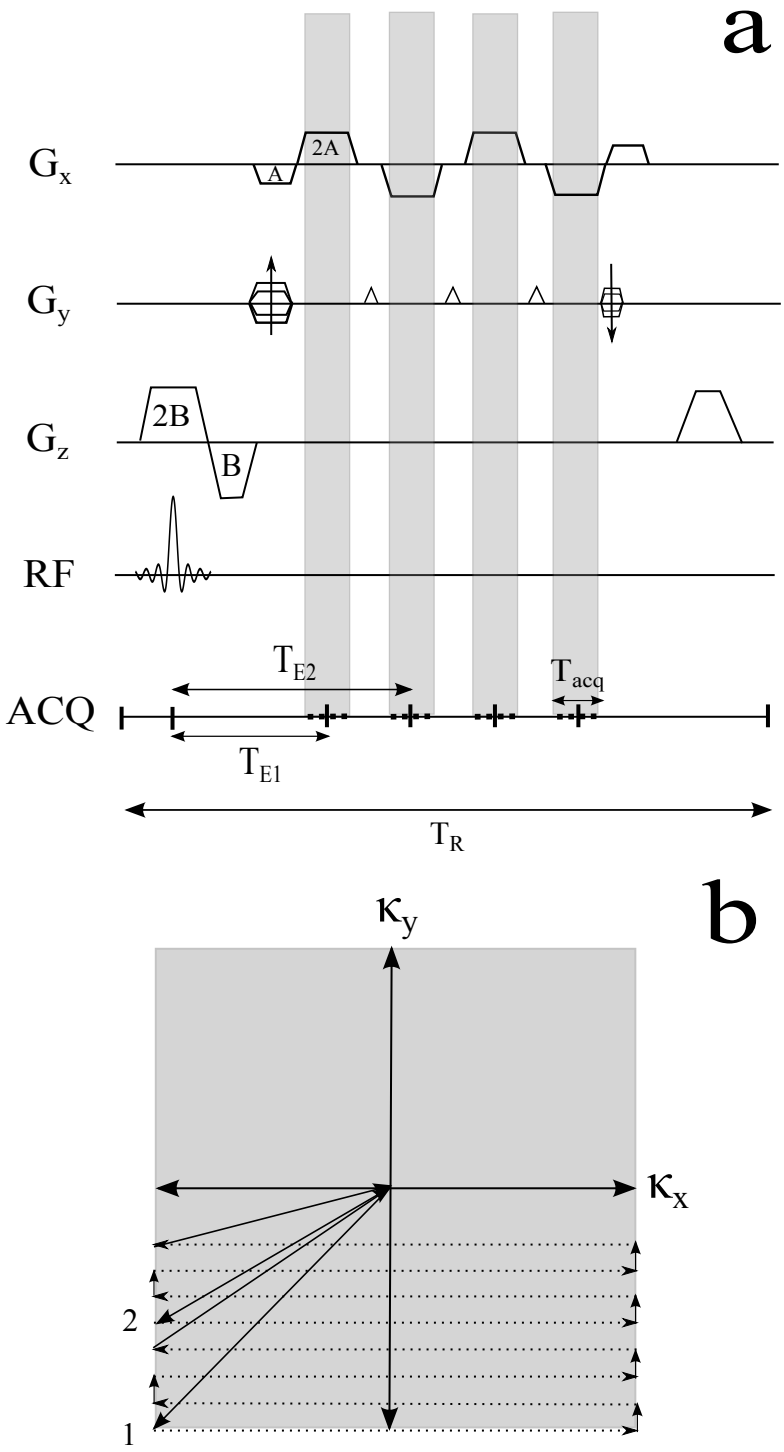

Figure 2.5: (a) A typical 2D EPI sequence for a transverse slice (in the xy-plane), including the rewinding and spoiling gradients, and showing the relative areas (A and B) under the gradient pulses. Each interleaf reads four horizontal lines in κ-space. (b) The corresponding sampling trajectory for the EPI sequence in (a). (Not drawn to scale).

as

$$\text{SNR} \propto M_{xy} V \sqrt{T_{tda}}. \tag{2.49}$$

It is important to point out that the voxel size V is a function of the data acquisition time T_{tda}, as smaller voxels require sampling a greater area of κ-space ($FOV_\kappa = 2\pi/\Delta x$), which leads to a longer T_{acq}. Moreover, the actual scan time T_{scan} may be much longer than the data acquisition time, because it contains some dead-time (such as time wasted during gradient-rewinding), and Eq. (2.49) does not take the effect of pulse-sequence design and relaxation (especially T_2^*) on the magnetization M_{xy}.

2.3.7 Multiple Coil Image Combination

The use of multiple surface receiver coils for MRI signal detection is becoming increasingly popular, as they offer both improved SNR and parallel imaging performance [23]. In this scenario, the complex image from each coil must be individually reconstructed, and all the coil images must be combined together in the image domain to form the final magnitude image. The simplest method of multiple coil image combination consists of taking the root-sum-of-squares (RSS) of the individual images $I_j(x, y)$ on a pixel-by-pixel basis, yielding the final magnitude image $I(x, y)$, according to

$$I(x, y) = \sqrt{\sum_j I_j^*(x, y) I_j(x, y)}, \tag{2.50}$$

where $I_j^*(x, y)$ is the complex conjugate of the pixel value at location (x, y). A weakness of this method is that it does not take into account the possibility of different noise variance σ_j^2 among the coils, yielding a magnitude image with sub-optimal SNR. Thus, a better alternative is to measure the noise variance σ_j^2 of each j^{th} coil, and compute the weighted RSS magnitude image defined by

$$I(x, y) = \sqrt{\sum_j \frac{I_j^*(x, y) I_j(x, y)}{\sigma_j^2}}. \tag{2.51}$$

The noise variance σ_j^2 may be obtained from the noise covariance matrix $\boldsymbol{\psi}$, calculated using the function *cov* in MATLAB. Each entry of the covariance matrix is given by

$$\psi_{j,k} = E(x_j^* x_k) - E(x_j^*) E(x_k), \tag{2.52}$$

where E is the expectation value and j, k are coil indices [1, p.501]. To compute the covariance matrix, a noise scan is performed (i.e., scanning the object without RF pulse

excitation), and the noise variances are given by the diagonal elements of the covariance matrix.

Roemer et al. [23] have shown that a combined image with better SNR than that of Eq. (2.51) may be obtained if the receive fields $B_{1,j}^{-}(x,y)$ are known. This "optimal SNR image" is calculated as

$$I(x,y) = \frac{\sum_{j,k} B_{1,j}^{-*}(x,y)\psi_{jk}^{-1} I_k(x,y)}{\left[\sum_{j,k} B_{1,j}^{-*}(x,y)\psi_{jk}^{-1} B_{1,k}^{-}(x,y)\right]^n}, \tag{2.53}$$

where j,k are coil indices, and n is an exponent. In matrix notation, Eq. (2.53) may be re-written as

$$I(x,y) = \frac{\boldsymbol{B}_1^{-*}(x,y)\cdot\boldsymbol{\psi}^{-1}\cdot\boldsymbol{I}(x,y)}{\left[\boldsymbol{B}_1^{-*}(x,y)\cdot\boldsymbol{\psi}^{-1}\cdot\boldsymbol{B}_1^{-}(x,y)\right]^n}, \tag{2.54}$$

where $\boldsymbol{B}_1^{-}(x,y)$ is a column vector with N entries (one for each coil at pixel location (x,y)), $\boldsymbol{\psi}$ is the $N\times N$ noise covariance matrix, and $\boldsymbol{I}(x,y)$ is a column vector consisting of the N complex image pixel values at (x,y). When $n=1$, Eq. (2.54) yields a "uniform sensitivity image," which implies that equal transverse magnetization will yield the same image intensity at every pixel. Roemer et al. also demonstrate that an alternative image weighting may be used to display the SNR variation within the combined image, by setting $n=1/2$. Such an image is referred to as a "uniform noise image." If $n=0$ both sensitivity and noise will vary across the image. Finally, because the exact receive fields $\boldsymbol{B}_1^{-}$ are difficult to measure or derive, a typical approximation involves calculating

$$B_{1,j}^{-} \approx \frac{I_j}{\sqrt{\sum_j \frac{I_j^* I_j}{\sigma_j^2}}}, \tag{2.55}$$

where the denominator is a reference image that, alternatively, may be acquired from a separate scan using the system's body coil rather than with the array. If Eq. (2.55) is used, and the non-diagonal elements in $\boldsymbol{\psi}$ are ignored, this approximation reduces to Eq. (2.51). Figure 2.6 shows a grid phantom image obtained from a 6-channel head array, where the coil images were combined using three of the methods described previously.

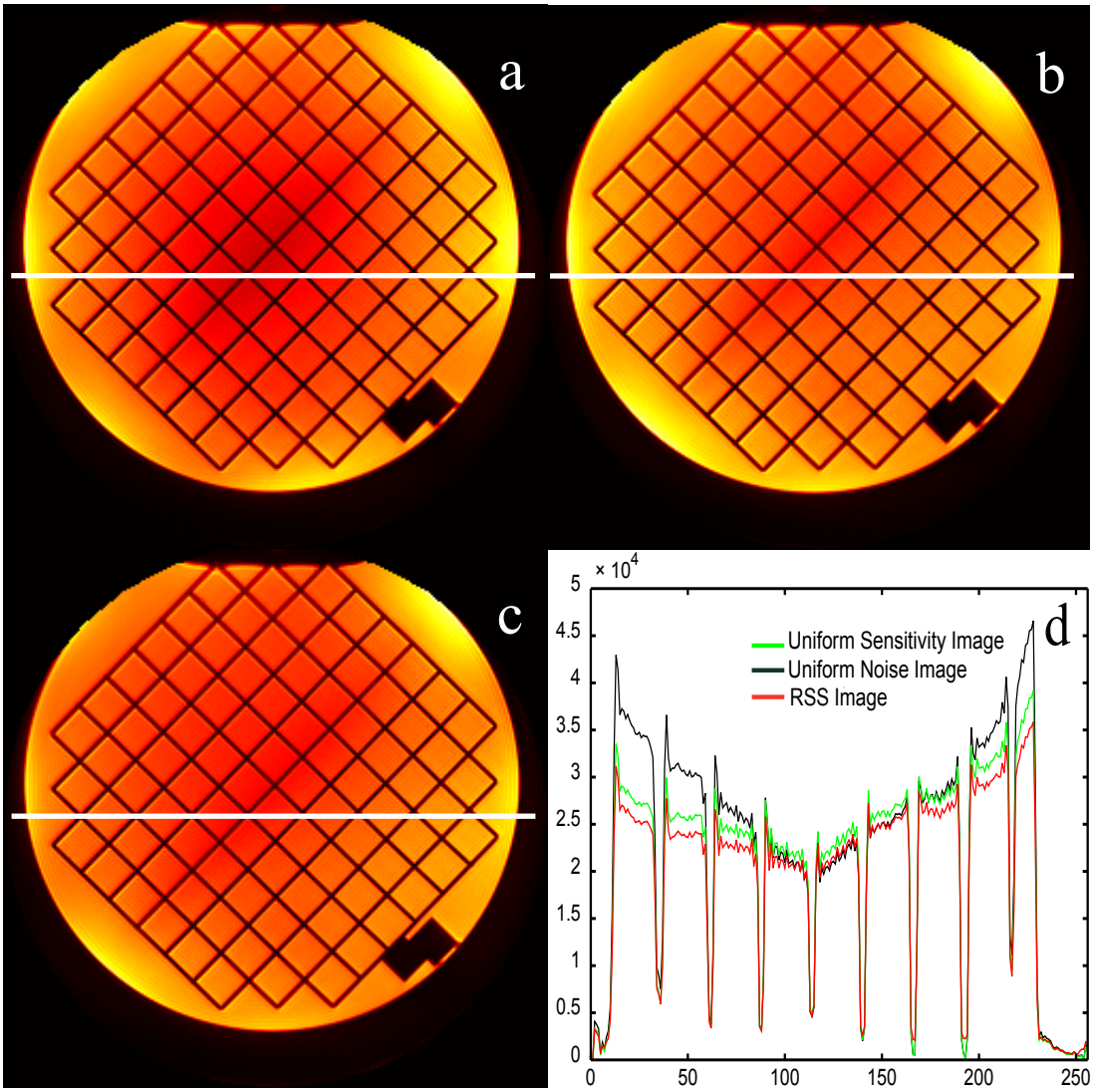

Figure 2.6: (a) Uniform noise image combination of eight coils obtained from Eq. (2.53) with $n = 1/2$. (b) Uniform sensitivity image combination obtained from Eq. (2.53) with $n = 1$. (c) RSS image obtained from Eq. (2.50). (d) Slice through the image in (a), (b) and (c), showing the signal intensity across the phantom.

CHAPTER 3

Acquisition and Reconstruction of Spiral Images with Artifact Corrections

3.1 Introduction

Spiral Magnetic Resonance Imaging (Spiral MRI) was first implemented in the late 1980s, and applied to coronary artery imaging [24]. Despite providing certain advantages over typical Cartesian sampling trajectories, including the ability to refocus flow and motion-induced phase errors [25, 26], and an efficient means of sampling κ-space, the technique never became a widely used method in the clinic due to its technical difficulties and sensitivity to blurring artifacts. More recently, with improvements in MR system hardware leading to more faithful κ-space trajectories, applications of spiral MRI have multiplied, notably in functional brain imaging and coronary imaging [26–28] where a rapid signal acquisition is required.

3.2 Spiral Trajectory

In a MRI pulse sequence, an interleaf refers to a segment of κ-space that is read (in an arbitrary direction) following an RF pulse excitation. A typical spiral trajectory for the n^{th} interleaf in κ-space is given in complex notation by Boernert et al. [29]:

$$\boldsymbol{\kappa}_n(t) = \kappa_{n,x} + i\kappa_{n,y} = \kappa_{max}\psi(t/T_{acq})e^{i2\pi J\psi(t/T_{acq})+i2\pi n/N_I} \tag{3.1}$$

where N_I is the number of spiral interleaves used to cover the whole κ-space, J is the number of revolutions of each interleaf (not necessarily an integer), T_{acq} is the acquisition time of one

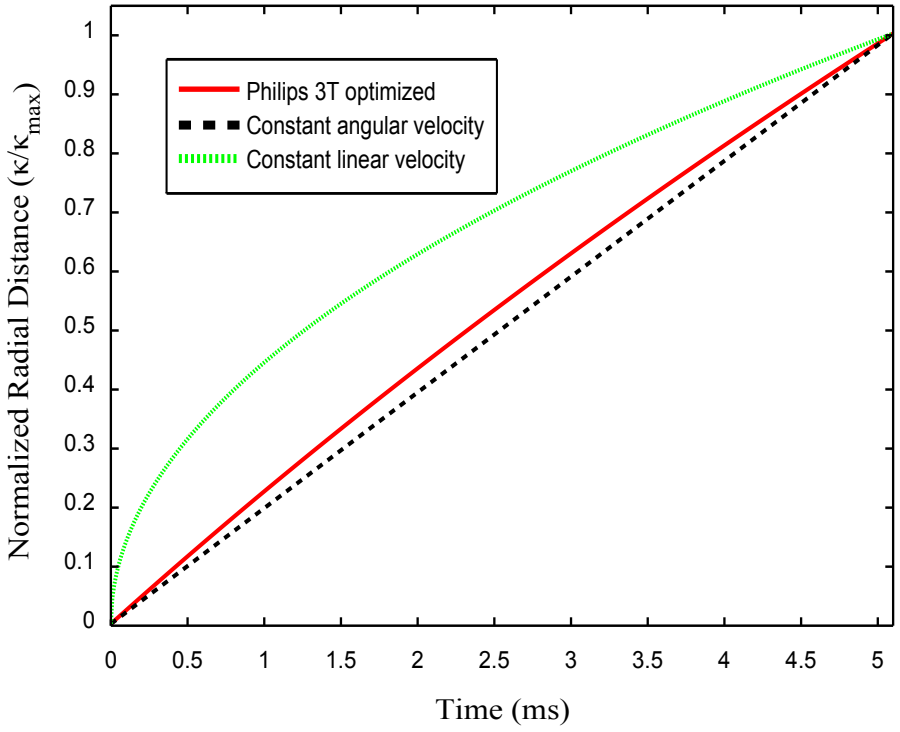

Figure 3.1: Comparison of $\psi(t/T_{acq})$ for the Philips 3T Achieva Scanner (solid red curve) in Eq. (3.2) with that for a constant linear velocity spiral (dotted green curve) and for a constant angular velocity spiral (dashed black curve). Here, $T_{acq} = 5.1$ ms, and $J = 2.133$.

interleaf, and $\psi(t/T_{acq})$ is a monotonically increasing function ranging from zero at $t = 0$ to unity at $t = T_{acq}$. Common choices include using $\psi = t/T_{acq}$, in which case, the spiral has constant angular velocity of the rotating gradient vector, or $\psi = \sqrt{t/T_{acq}}$ where the spiral has constant linear velocity. A choice for $\psi(t/T_{acq})$ that is optimal for the given scanner hardware typically lies in between those two extremes [29]. The spiral gradient waveforms programmed on the Philips 3T Achieva MRI scanner, correspond to the trajectory of Eq. (3.1) with

$$\psi(t/T_{acq}) = \frac{t}{T_{acq}} \sqrt{\frac{\frac{1}{\lambda T_{acq}} + 1}{\frac{1}{\lambda T_{acq}} + \frac{t}{T_{acq}}}}. \tag{3.2}$$

Note here that $\lambda = min\{3, J\}/T_{acq}$, a parameter facilitating the transition from a constant angular velocity to a variable angular velocity spiral. The function $\psi(t/T_{acq})$ has been plotted in Fig. 3.1 for a typical spiral trajectory consisting of 60 interleaves, a field-of-view (FOV) of 25 cm, and pixel resolution of 0.98 mm. Observe that it is quite close to being a constant angular velocity spiral. The gradient waveforms are readily obtained by differentiating Eq. (3.1), yielding

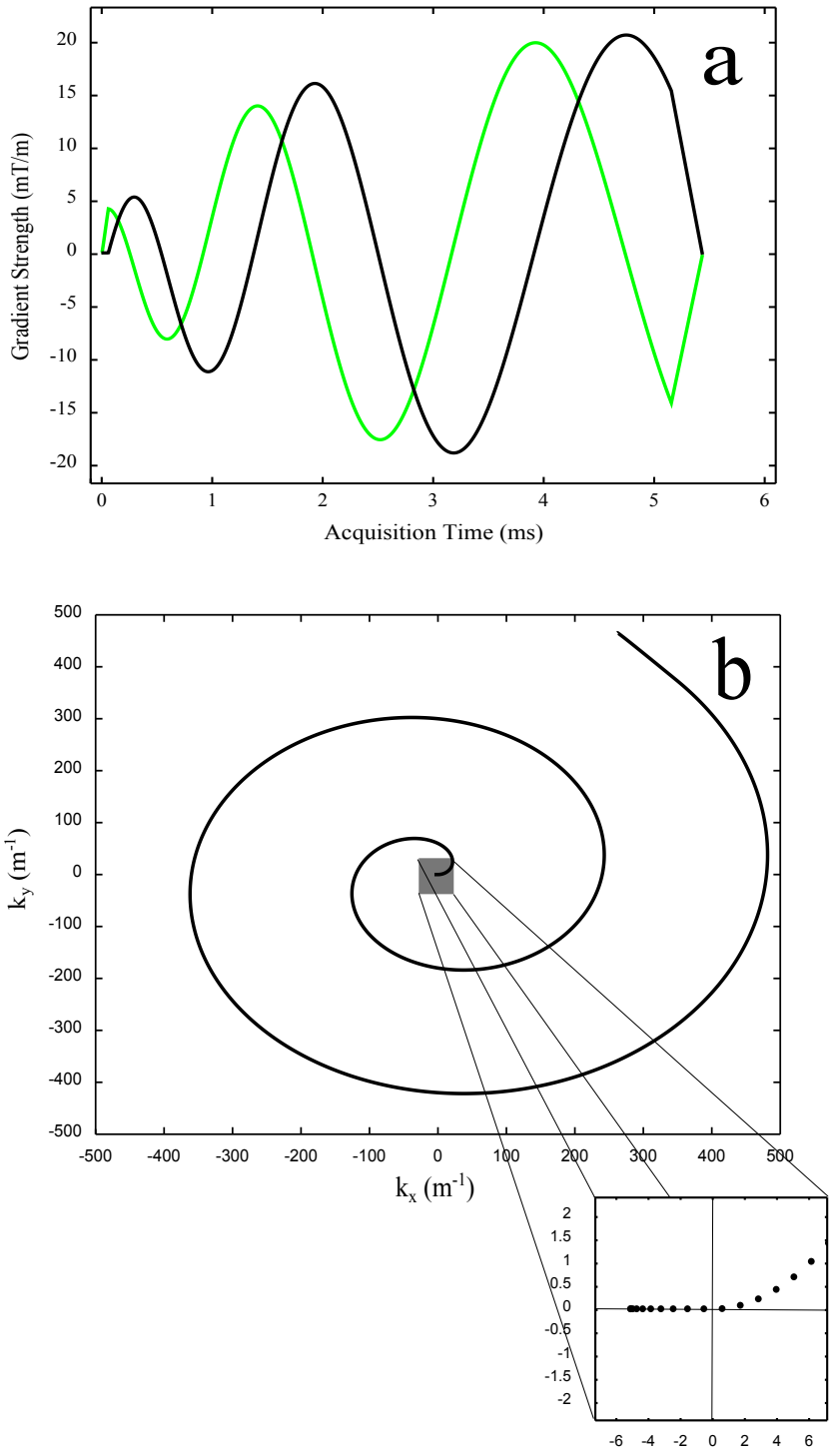

Figure 3.2: (a) Gradient waveforms of the first interleaf for $N_I = 60$, $FOV_d = 25$ cm, and $T_{acq} = 5.1$ ms: G_x (green) and G_y (black). (b) Plot of the κ-space trajectory obtained by numerical integration of the waveforms, including the back-swing which allows the acquisition to begin with a finite velocity at the origin.

$$\begin{aligned} G_x(t) &= \frac{2\pi J N_I}{2FOV_d\gamma}\dot{\psi}\left[\cos(2\pi J\psi) - (2\pi J\psi)\sin(2\pi J\psi)\right] \\ G_y(t) &= \frac{2\pi J N_I}{2FOV_d\gamma}\dot{\psi}\left[\sin(2\pi J\psi) + (2\pi J\psi)\cos(2\pi J\psi)\right], \end{aligned} \tag{3.3}$$

where $\dot{\psi}$ is the time-derivative of ψ, FOV_d is the diameter of the circular FOV in image space, and $\gamma = 267.4 \times 10^6 rad T^{-1} s^{-1}$ is the gyromagnetic ratio for protons. The κ-space trajectory was obtained by numerical integration of Eq. (3.3) after inserting ψ and $\dot{\psi}$ from Eq. (3.2):

$$\boldsymbol{\kappa}(t) = \gamma \int_0^t \boldsymbol{G}(\tau) d\tau. \tag{3.4}$$

All other interleaves $\boldsymbol{\kappa}_n$ are obtained readily by multiplying the first interleaf $\boldsymbol{\kappa}_0$ with the 2D rotation matrix

$$\begin{pmatrix} \kappa_{n,x} \\ \kappa_{n,y} \end{pmatrix} = \begin{pmatrix} \cos(\Delta\phi\, n) & \sin(\Delta\phi\, n) \\ -\sin(\Delta\phi\, n) & \cos(\Delta\phi\, n) \end{pmatrix} \begin{pmatrix} \kappa_{0,x} \\ \kappa_{0,y} \end{pmatrix}, \tag{3.5}$$

where $\Delta\phi = 2\pi/N_I$ is the angle between any two successive interleaves.

When performing a spiral scan on the Philips Achieva platform, the user must specify FOV_d, the size of the acquisition matrix (a square matrix of dimensions $L_{acq} \times L_{acq}$), the acquisition time, T_{acq}, and the number of interleaves, N_I. Note that $J = L_{acq}/(2N_I)$. The scanner software then uses these parameters to compute the required gradient waveforms. These parameters are constrained by the maximum slew rate and gradient strength of the system hardware, and thus certain combinations may be forbidden. In order to obtain the best image quality, one must select the desired FOV and acquisition matrix size, and minimize the acquisition time for a desired number of interleaves. In general,

$$\min\{T_{acq}\} \propto \frac{L_{acq}^2}{N_I FOV_d G_{max}}, \tag{3.6}$$

where G_{max} is the maximum strength of the spiral gradient waveform [30]. Thus, using more interleaves shortens the minimum possible acquisition time, reducing off-resonance artifacts, but also requiring a longer total scan time. For the Philips 3T Achieva scanner equipped with a maximum gradient strength of 21 mT/m and slew rate of 100 T/(m s) the proportionality constant of Eq. (3.6) is $\approx 2.4 \times 10^{-8}$ T s.

3.3 Spiral Pulse Sequence

The spiral pulse sequences studied in this thesis are shown in Fig. 3.3. For a given interleaf in the 2D case, it consists of a basic slice-selection RF sinc pulse that excites a slice, followed

by the spiral acquisition. Immediately following the acquisition, the read gradients are rewound and a spoiler gradient is applied along the direction of the slice in order to suppress stimulated echoes. In the 3D case, a thick slab is excited, followed by a phase-encoding step along the direction orthogonal to the slab. Spiral gradient waveforms are used to read the signal along the other two dimensions, similar to the 2D case. A rewinding gradient and a spoiler gradient are applied at the end.

Although the signal acquisition includes about 14 sample locations before the crossing of the κ-space origin, the first 15 samples are not included as part of the reconstruction because they are too densely spaced, (especially when a large number of interleaves is used) for the sampling density compensation (covered in §3.4.3) to be applied correctly. This may be understood from the fact that the signal samples at the centre of κ-space have a high amplitude and contribute to the bulk of the image intensity, while the density compensation weights are close to zero; hence any inaccuracy in the density compensation tends to be amplified.

3.4 Gridding Reconstruction

3.4.1 1D Non-Uniform Fast Fourier Transform of Type-1

Unlike Cartesian MRI sampling trajectories where the samples are spaced at regular intervals along the two κ-space directions, a spiral sampling trajectory is not uniform in κ-space. Consequently, image reconstruction cannot be performed by simply taking the discrete 2D Fourier transform of the κ-space signal. Instead, each acquired signal sample must be assigned to its corresponding position in κ-space and a non-uniform discrete Fourier transform must be employed. The following discussion is based on Greengard et al. [31] and outlines the theory behind one-dimensional non-uniform fast Fourier transform (NUFFT). The 2D version of the NUFFT used in 2D image reconstruction readily follows from the 1D case, by using a coordinate system where the kernel of the Fourier transform is separable.

The 1D NUFFT involves the computation of

$$f(x) = \frac{1}{N} \sum_{j=0}^{N-1} F_j e^{-i\kappa_j x}, \quad x = -M/2, \ldots, M/2 - 1 \tag{3.7}$$

where in the context of MRI reconstruction $f(x)$ is the complex image (in arbitrary units) and is uniformly sampled on a Cartesian grid of M points, while F_j is the complex signal, of N non-uniformly spaced samples κ_j in spatial-frequency space. F_j must also include a density compensation, which is discussed in §3.4.3. We may rewrite Eq. (3.7) in the form of

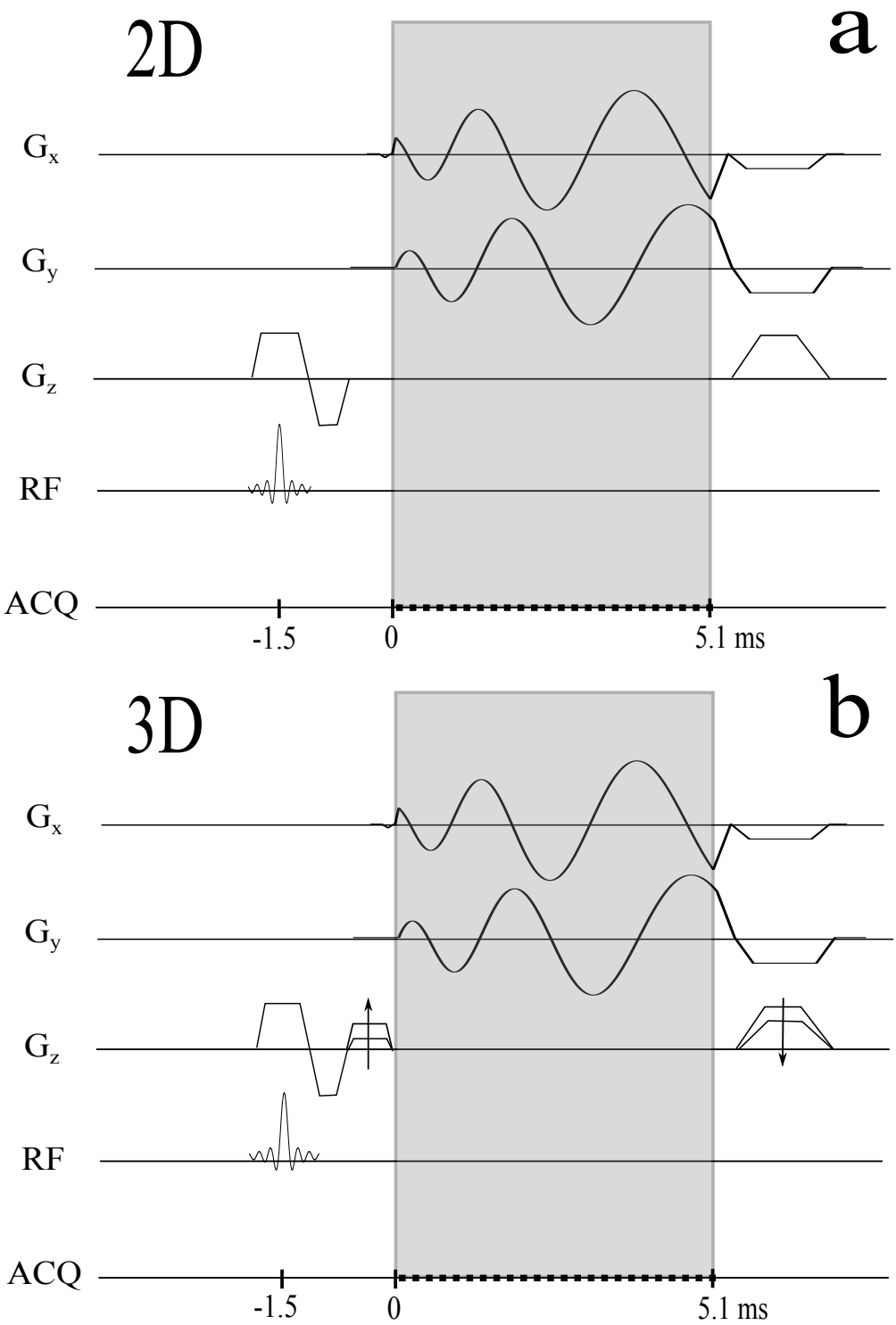

Figure 3.3: (a) 2D spiral pulse sequence for $N_I = 60$, $FOV_d = 25$ cm, $T_E = 1.5$ ms and $T_{acq} = 5.1$ ms. (b) Equivalent 3D spiral pulse sequence showing the phase-encoding step along the z direction. Note that the gradient pulses are not drawn to scale.

a convolution

$$f(x) = \int_0^{2\pi} \frac{1}{N} \sum_{j=0}^{N-1} F_j \delta(\kappa - \kappa_j) e^{-i\kappa x} d\kappa, \tag{3.8}$$

which is the Fourier transform of

$$F(\kappa) = \sum_{j=0}^{N-1} F_j \delta(\kappa - \kappa_j), \tag{3.9}$$

viewed as a periodic function on $[0, 2\pi]$. Note that δ is the Dirac-delta generalized function. The process of gridding consists of selecting a convolution kernel $\Gamma(\kappa)$, convolving it with the function $F(\kappa)$, resampling the signal onto an oversampled uniform grid of K points, taking the discrete Fourier transform, and finally deconvolving the result in order to recover the image $f(x)$ in Cartesian space. To accomplish this task, it is common to use a periodic Gaussian kernel

$$\Gamma_\tau(\kappa) = \sum_{l=-\infty}^{\infty} e^{-(\kappa - 2\pi l)^2/4\tau}, \tag{3.10}$$

where τ determines the spacing on a well-resolved uniform grid in κ. Now let

$$F_\tau(\kappa) = F(\kappa) * \Gamma_\tau(\kappa) = \sum_{j=0}^{N-1} F_j \Gamma_\tau(2\pi m/K - \kappa_j), \tag{3.11}$$

where $\kappa = 2\pi m/K$, the new sampled mesh with K samples. Taking the Fourier transform we have

$$f_\tau(x) = \frac{1}{K} \sum_{m=0}^{K-1} F_\tau(2\pi m/K) e^{-ix2\pi m/K}. \tag{3.12}$$

The final step consists of deconvolving $f_\tau(x)$ to obtain $f(x)$ by dividing by the Fourier transform of the Gaussian kernel

$$f(x) = \sqrt{\frac{\pi}{\tau}} e^{x^2\tau} f_\tau(x). \tag{3.13}$$

Dutt et al. [32] have shown that $K = 2M$ and $\tau = 6/M^2$, (Gaussian spreading of each source to the nearest 12 grid points) achieves an accuracy of 1 in 10^6. In MR image reconstruction, 3 digits of accuracy is more than sufficient given typical image SNR values around 100 or less.

3.4.2 Selection of the Convolution Kernel

As shown by O'Sullivan [33], the ideal convolution kernel would be an infinite sinc function, whose Fourier transform corresponds to a uniform rectangular box. If parameters are

selected such that the extent of the rectangular box corresponds with the FOV, then no deconvolution step would be required. However, such a scheme (an exact non-uniform discrete Fourier transform) is computationally impractical due to the size of the convolution kernel, and one is forced to use a band-limited kernel. The first, and still the most popular kernel used in gridding reconstruction is the Kaiser-Bessel window [34], which is given by

$$\Psi(\kappa) = \frac{1}{L} I_0 \left(\beta \sqrt{1 - (2\kappa/L)^2} \right), \tag{3.14}$$

where I_0 is the zeroth-order modified Bessel function, L is the length of the window, and β is an optimization parameter. Jackson et al. [34] have shown that values of $L = 4$ and $\beta = 12$ yield the least amount of root-mean-squared error. The Gaussian kernel was introduced later by mathematicians to provide a rigorous analysis because of its simplicity and computational advantages. Sarty et al. [35] showed that an optimal Gaussian kernel provides the same accuracy as the standard Kaiser-Bessel kernel for large images (256^2 pixels) and marginally better accuracy for small images (64^2 pixels). The algorithm used in this thesis is based on Ref. [31], where the NUFFT is accelerated by a factor of $5 - 10$ by exploiting the fact that the Gaussian kernel may be expressed as a tensor product

$$\Gamma(\kappa) = e^{-(\kappa_j - 2\pi m/K)^2/4\tau} = e^{-\kappa_j^2/4\tau} \left(e^{\kappa_j \pi/K\tau} \right)^m e^{-(\pi m/K)^2/\tau}. \tag{3.15}$$

Thus, the two exponentials $e^{-\kappa_j^2/4\tau}$ and $e^{\kappa_j \pi/K\tau}$ may be computed and stored for each j^{th} source point, while the third exponential $e^{-(\pi m/K)^2/\tau}$ is independent of κ_j. In MATLAB, operating on an Intel Core2 Duo CPU E8400 (3 GHz, 3.5 MB available RAM) reconstructing a 256×256 image with the desired three digits of accuracy only takes ~ 0.25 s, making the algorithm extremely fast compared to other competing methods (e.g., iterative reconstruction algorithm using the conjugate gradient method).

3.4.3 Density Compensation Function

In Eq. (3.7), the discrete κ-space samples F_j were assumed to be already pre-corrected by the density compensation function W_j which is proportional to the area surrounding each sample location in κ-space:

$$f(\mathbf{r}) = \int F(t) e^{-i\boldsymbol{\kappa}(t)\cdot\mathbf{r}} W(t) dt. \tag{3.16}$$

This amplitude correction term, accounts for the fact that samples must be weighted according to the local sampling density. Various methods of calculating $W(t)$ have been demonstrated in the literature, including analytical [24], iterative [36], and other numerical

techniques [37, 38]. Calculation of the density compensation function can often take longer than the actual gridding reconstruction itself, but fortunately, it depends entirely on the κ-space acquisition sampling trajectory and can be precomputed only once prior to the scan and stored in a matrix. In this thesis, I have used the method of Ref. [38] with Voronoi diagrams to compute the sampling density compensation function. A formal definition of the Voronoi diagram is provided by Aurenhammer [39], but for our purpose, it suffices to describe the Voronoi diagram as a 2D web (shown in Fig. 3.4(a)), where each point is assigned a cell of finite area centered at its location.

The Voronoi diagram is computed by the native MATLAB function via a Delaunay triangulation, and the area of the Voronoi polygon for the j^{th} κ-space sample is used as a measure of the corresponding density compensation weight W_j. We note that although the whole κ-space sample plane of an image is needed to compute the density compensation function (see Fig. 3.4(a)), the function is virtually identical for every interleaf, because the spiral interleaves are rotationally symmetric. The Voronoi diagram of a quadrant of κ-space is shown in Fig. 3.4, along with the corresponding sampling density compensation $W(t)$ for one interleaf. (Here, $W(t)$ is simply W_j expressed in terms of the sampling time scale instead of the sample index.) Thus the term F_j in Eq. (3.7) may be expressed in terms of W_j as

$$F_j = W_j S_j, \tag{3.17}$$

where S_j is the raw signal sample.

3.4.4 1D Non-Uniform Fast Fourier Transform of Type-2

The concept of gridding is referred to by Greengard et al. [31] as the "type-1" NUFFT or by Sarty et al. [35] as the Generalized fast Fourier transform (GFFT). Other non-uniform fast Fourier transforms (e.g., type-2 and type-3) have also been studied and used in other situations. A type-2 NUFFT algorithm performs the opposite; it evaluates the inverse Fourier transform of uniform data at non-uniform sample locations. Finally, the type-3 algorithm is a combination of the first two in that it takes non-uniform data, and evaluates the Fourier transform on another non-uniform grid [40]. In chapter 3, the type-2 NUFFT is used to simulate the acquired MRI spiral signal of a digital phantom.

In one dimension, for $\kappa_j \in [0, 2\pi]$, the type-2 NUFFT is defined by the calculation of

$$F(\kappa_j) = \sum_{x=-M/2}^{M/2-1} f(x) e^{i\kappa_j x}. \tag{3.18}$$

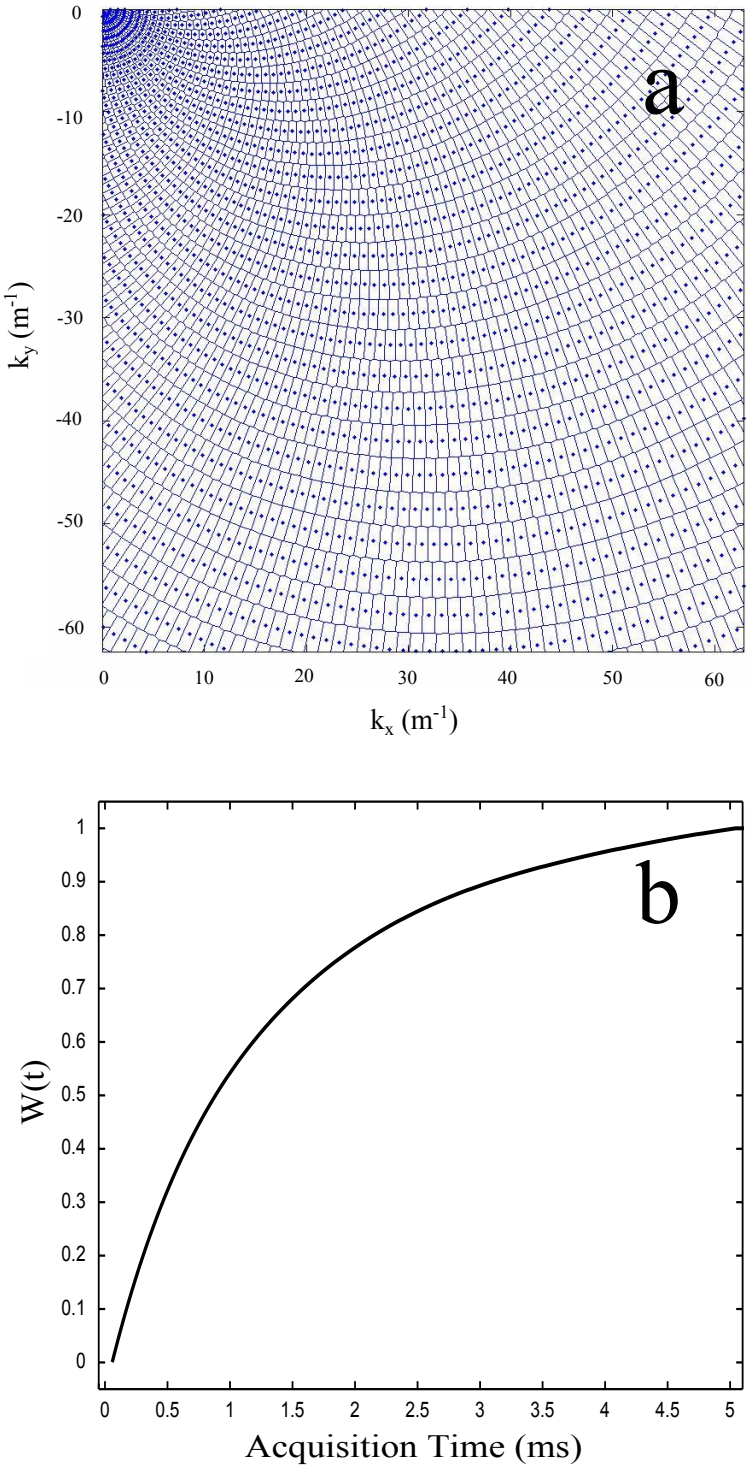

Figure 3.4: Voronoi diagram of the spiral sampling trajectory (a), and the corresponding density compensation function $W(t)$ for one interleaf (b). Note that the center of κ-space is highly oversampled. Parameters for the spiral sequence are: $T_{acq} = 5.1$ms, $N_I = 60$, $L_{acq} = 256$, and $FOV_d = 25$ cm.

First, we deconvolve the Fourier coefficients, defining $f_{-\tau}(x)$ by

$$f_{-\tau}(x) = \sqrt{\frac{\pi}{\tau}} e^{x^2 \tau} f(x), \tag{3.19}$$

and evaluate the corresponding function $F_{-\tau}(\kappa)$ on a uniform mesh with K points on $[0, 2\pi]$ using the FFT

$$F_{-\tau}(\kappa) = \sum_{x=0}^{K-1} f_{-\tau}(x) e^{i\kappa x}. \tag{3.20}$$

In the preceding, we then set $f_{-\tau}(x) = 0$ for $\frac{M}{2} \leq x < K - \frac{M}{2}$ and view $f_{-\tau}(x)$ as a K-periodic function $f_{-\tau}(x) = f_{-\tau}(x - K)$. Finally, we compute the desired values $F(\kappa_j)$ from

$$F(\kappa_j) = F_{-\tau} * G_\tau(\kappa_j) = \frac{1}{K} \sum_{m=0}^{K-1} F_{-\tau}(2\pi m/K) G_\tau(\kappa_j - 2\pi m/K). \tag{3.21}$$

Note that unlike the type-1 NUFFT, the type-2 does not require a sampling density compensation.

3.4.5 Image Reconstruction of a Spiral MRI Scan

A spiral image of a grid within the American College of Radiology Magnetic Resonance Accreditation phantom (ACR MRAP) was acquired on the Philips Achieva 3T scanner based on the sampling trajectory described in §3.2. The slice was shimmed with both first and second-order shims to minimize the effect of static magnetic field inhomogeneity. The raw data was processed off-line via a MATLAB routine that utilizes the type-1 NUFFT and Voronoi-based sampling density compensation. A small time delay of 6 μs was applied to the spiral waveforms in order to compensate for eddy-currents and/or gradient delays. The magnitude image reconstructed from the raw data is displayed in Fig. 3.5(a), along with the image that the built-in Philips reconstructor produces on-line (b). The two images are not exactly identical due to differences in filtering and reconstruction algorithms, but a careful inspection reveals that the two images are of equivalent quality.

3.5 Gradient Delay and Eddy-Currents Correction

According to Faraday's Law of induction, a changing magnetic field induces an electric field. If this electric field occurs within a conductor, an electrical current will be induced. These "eddy" currents tend to flow in conductors on the outside of the gradient coils, inducing a magnetic field that opposes the original magnetic field (i.e., Lenz's law). Eddy currents are problematic in MRI hardware because they distort the temporal waveforms and spatial

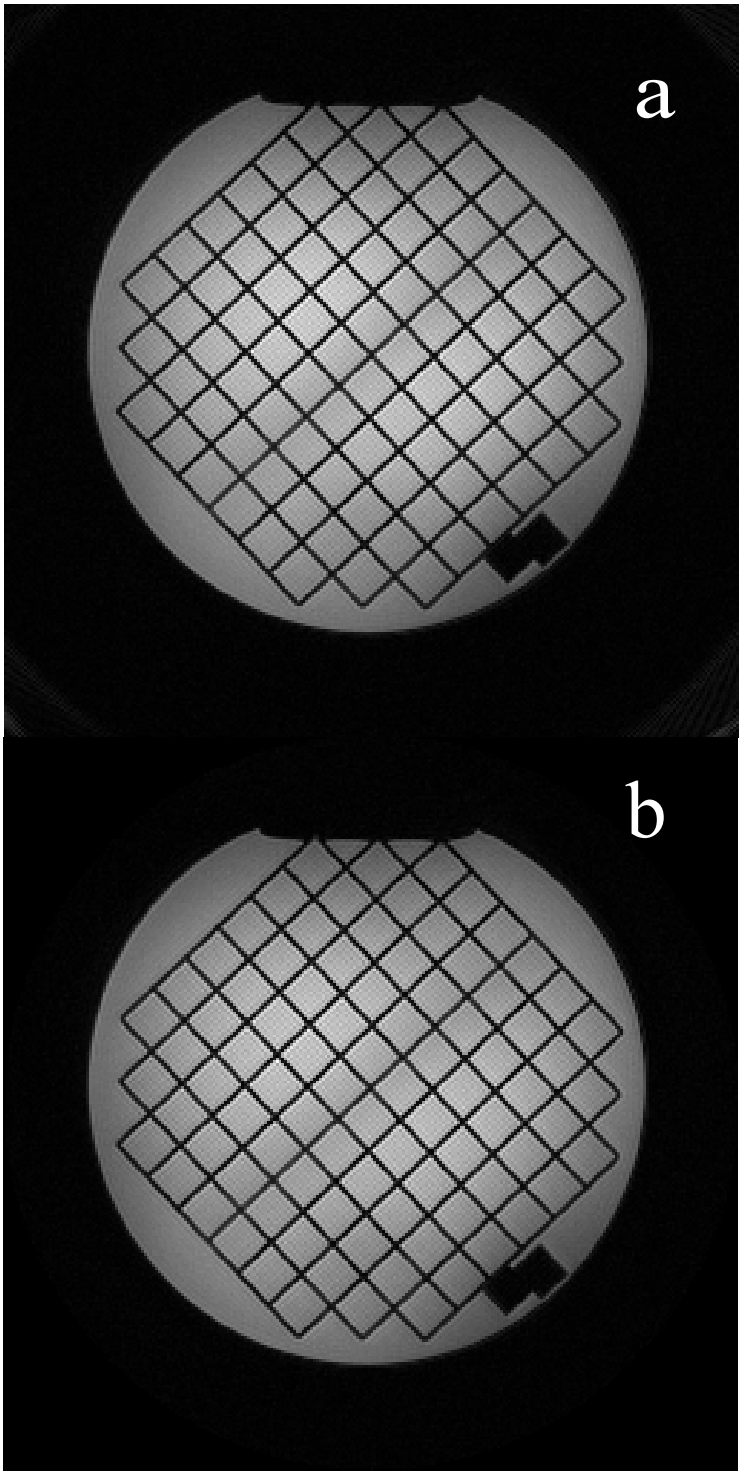

Figure 3.5: Spiral image of a grid phantom reconstructed using an off-line MATLAB subroutine (a), compared to the Philips on-line built-in reconstruction (b). Differences in the angle of the gibbs ringing of the two images are readily noticeable. Imaging parameters include: $L_{acq} = 256$, $N_I = 60$, $T_{acq} = 5.1$ ms, $FOV_d = 25$ cm, $T_R = 500$ ms, $T_E = 1.76$ ms, 50° flip angle, and 3 mm slice thickness.

distribution of the gradient fields that we are trying to create in the presence of the object within the system's imaging region.

One method of preventing eddy currents utilizes active shielding of the gradient coils. For a cylindrical-bore magnet, active shielding consists of connecting an outer coil in series with the main coil. The diameters, conductor wire design, and the currents of these concentric coils are selected so that their fields cancel outside the larger cylinder, leaving only a small net field. Hence they are reduced by minimizing the gradient fringe field [1].

Any residual eddy currents are compensated for by applying a pre-emphasis to the gradient waveforms [1] i.e., the effect of eddy currents on the output gradient waveforms is predicted and the waveforms programmed into the system are pre-distorted so as to achieve the desired net physical gradient waveforms within the imaging volume. As shown by Bernstein [1], the net output gradient waveform may be modeled as

$$G_{net}(t) = G_{applied}(t) + g(t) \tag{3.22}$$

where g(t) is the amplitude change due to eddy currents, given by

$$g(t) = -\frac{dG(t)}{dt} * e(t) \tag{3.23}$$

and $e(t)$ is the eddy current impulse response function. For the Philips 3T Achieva scanner, the impulse response is characterized by a gradient settling amplitude $\alpha_s = 0.3$, and a settling constant $\tau_s = 60\ \mu s$. Figure 3.6 shows the pre-emphasized G_x gradient waveform, along with the net waveform of Fig. 3.2. Although the difference between to two waveforms might appear negligible, serious artifacts will result in the image if the pre-emphasized waveform is used to grid the data instead of the net waveform. A final, small time delay must also be applied to the waveforms in order to remove the combined gradient delays. This time delay is equivalent to slightly adjusting the temporal location of the acquisition window within the imaging sequence. Although in general the correct delay depends on the gradient channels (x, y, and z), an average value of 6 μs was found to yield quality images on the Philips 3T Achieva scanner.

3.6 Off-Resonance Correction

The imaging equation Eq. (2.33) assumes that the Larmor frequency is constant over the whole imaging region. To include the effect of off-resonance conditions (e.g., B_0 shim,

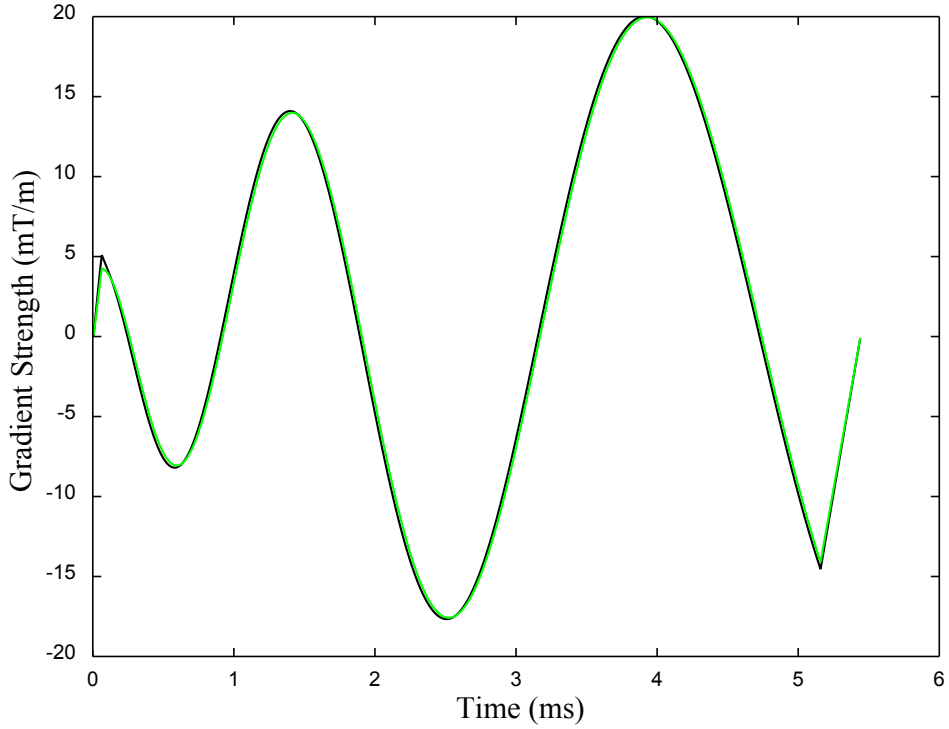

Figure 3.6: Gradient waveform $G_x(t)$ with pre-emphasis (black) compared with the ideal (net) output waveform (green). Note the small gradient delay that arises from the impulse response, and the positive ramp at the beginning of the waveform which reaches a higher peak in amplitude. The net waveform also reaches a maximum amplitude that is slightly lower than the pre-emphasized waveform.

chemical shift, etc.) it is modified to

$$S(t) = \int_V m(\boldsymbol{r}) e^{-i(\boldsymbol{k}(t)\cdot\boldsymbol{r} + \Delta\omega(\boldsymbol{r})\, t)} d^3r, \tag{3.24}$$

where $m(\boldsymbol{r})$ is the magnetization at location $\boldsymbol{r}$, and $\Delta\omega$ is the resonance offset from the demodulation frequency ω_0 arising from a combination of the main static magnet inhomogeneity ΔB_0, the magnetic susceptibility differences ΔB_χ, and the chemical shift ΔB_{CS} at location $\boldsymbol{r}$ [41]. The static magnet inhomogeneity ΔB_0, which is generally the most significant contributor to the resonance offset, can be removed by higher-order shimming. If the FOV is not too large, and we are only interested in shimming a single slice, first and second-order shimming can almost fully remove ΔB_0, leaving only the off-resonance due to susceptibility differences and chemical shift. When ΔB_{CS} arises from water and fat chemical shift difference (as is commonly the case), and we are not interested in signal arising from fat, it may be removed by using fat-suppression RF pulses at the start of the imaging sequence. Standard gridding reconstruction assumes $\Delta\omega$ to be zero, with resulting visible blurring artifacts that depend on the range of $\Delta\omega$ over the image, and the acquisition time T_{acq}. One way to minimize blurring while maintaining pixel resolution is to use a large number of interleaves, with a shorter acquisition time T_{acq}, or by using higher slew rates and gradient strengths, which also permit a shorter T_{acq}. However, using too many interleaves N_I defeats the purpose of spiral imaging, since the κ-space becomes less efficiently sampled as N_I increases, and the total scan time lengthens significantly for an equal T_R. An alternative approach consists of incorporating the off-resonance term $\Delta\omega$ in the reconstruction.

Blurring artifact can be corrected in spiral MRI, just as distortion corrections can be performed on Cartesian MRI images [41]. Methods of spiral image deblurring may be grouped into various categories, such as those that require a phase map [42, 43], versus those that use an objective function to quantify and minimize the blur [44]. Certain methods may be considered as exact [40, 45, 46], and work equally well on images with a steeply-varying resonance offset, while other methods are approximate [42, 47, 48], and are only effective when the resonance offset is slowly-varying.

Two recently-developed exact deblurring algorithms include that of Eggers et al. [45], who use a gridding-based conjugate gradient reconstruction, and that of Makhijani et al. [46], who employ a post-gridding convolution-based conjugate gradient algorithm to reconstruct spiral images with sharply-varying resonance offsets. Both methods achieve full deblurring where approximate methods fail, however, they are conceptually more complex and computationally intensive.

For the past two decades, the most common method of deblurring spiral images has

been the conjugate-phase reconstruction technique (CPR) [26], which consists of demodulating the signal (multiplying it by $e^{i\Delta\omega_n\, t}$) under a range of N frequency offsets $\Delta\omega_n$, and reconstructing a separate image for each offset. The final pixel value is assigned based on its frequency offset obtained from a field map. An exact implementation of this method is time-consuming because no interpolation scheme is employed. Conceptually, this method is equivalent to calculating the conjugate-phase image

$$I_{cp}(\boldsymbol{r}) = \int_0^{T_{acq}} S(t) e^{i(\boldsymbol{k}(t)\cdot\boldsymbol{r} + \Delta\omega(\boldsymbol{r})\, t)} W(t) dt, \tag{3.25}$$

based on the approximation

$$e^{i\Delta\omega(\boldsymbol{r})\, t} S(t) = e^{i\Delta\omega(\boldsymbol{r})\, t} \int_V m(\boldsymbol{r}) e^{-i(\boldsymbol{k}(t)\cdot\boldsymbol{r} + \Delta\omega(\boldsymbol{r})\, t)} d\boldsymbol{r} \approx \int_V m(\boldsymbol{r}) e^{-i(\boldsymbol{k}(t)\cdot\boldsymbol{r})} d^3r, \tag{3.26}$$

which in practice gives acceptable results when $\Delta\omega(\boldsymbol{r})$ is smoothly-varying, as is usually the case for ΔB_0. The assumption of Eq. (3.26) is violated when T_{acq} is too long, resulting in excessive dephasing, which CPR can no longer recover. On the Philips 3T Achieva Scanner, with only the first-order shimming routine turned on, this limit begins to be reached when images are acquired with $T_{acq} \geq 20$ ms, (15 interleaves or less, for a 256×256 image), where some residual blurring may be observed in the deblurred image. Given a frequency range of ≈ 200 Hz over the phantom region of 20 cm (see, Fig. 3.8(c)), and $T_{acq} = 20$ ms, this translates to ≈ 0.125 rad of dephasing between two adjacent pixels.

3.6.1 Frequency-Segmented Off-Resonance Correction

Because an exact CPR method is computationally inefficient, much research has been done in speeding up the basic calculation of Eq. (3.25). Here, I present the method of Frequency-Segmented Off-Resonance Correction (FSORC) which was proposed by Noll et al. [49], and from which slightly faster methods have been derived more recently, such as Block Regional Off-Resonance Correction BRORC [47], and Multi-Frequency Interpolation (MFI) [42]. These, however, do not provide further improvements in accuracy, since they all rely on the same basic assumption of Eq. (3.26).

In FSORC, the range of frequency offsets $\Delta\omega(\boldsymbol{r})$ over the field inhomogeneity map is divided into N different bins. The signal is gridded once, after applying the sampling density compensation, after which it is demodulated at N different frequency offsets and Fourier transformed to obtain N different images. Finally, the field inhomogeneity map is used to find the two nearest frequency bins that correspond to each pixel. Each pixel is thus interpolated linearly between two images, each one obtained from a nearby frequency bin. This process is illustrated in Fig. 3.7. The minimum number of frequency bins N required

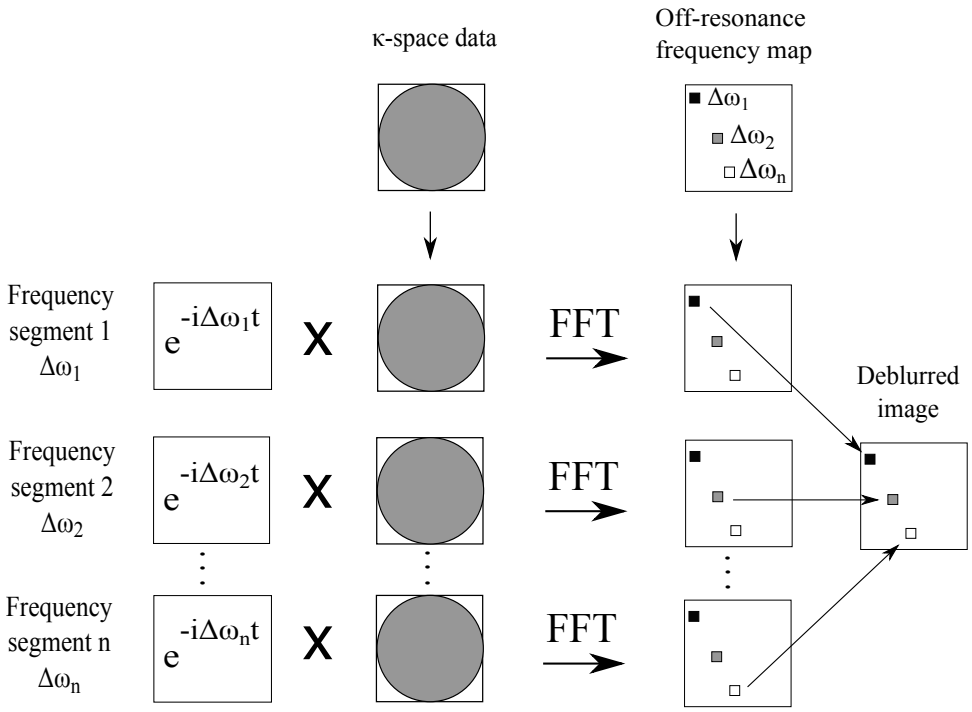

Figure 3.7: Method of Frequency-Segmented Off-Resonance Correction (FSORC). Adapted from [1, p.948].

to achieve full deblurring is given by the criterion derived by Noll et al. [43]

$$N \geq \frac{4(\Delta\omega_{max} - \Delta\omega_{min})T_{acq}}{\pi}, \tag{3.27}$$

where $\Delta\omega_{max}$ is the largest positive frequency offset, and $\Delta\omega_{min}$ is the minimum frequency offset of the field inhomogeneity map.

In terms of matrix algebra, the κ-space signal was first gridded onto a Cartesian grid resulting in matrix $\boldsymbol{S}$. The time points $t(\kappa)$ were also gridded onto a Cartesian time map $\boldsymbol{T}$, which is the acquisition time at each κ-space location. These operations enable the fast reconstruction of multiple images $\boldsymbol{I}_{\Delta\omega_n}$ using standard FFT from which the linear interpolation can be performed for each pixel

$$\boldsymbol{I}_{\Delta\omega_n} = \mathrm{FFT}\{\boldsymbol{S}\exp(-i\Delta\omega_n\boldsymbol{T})\}. \tag{3.28}$$

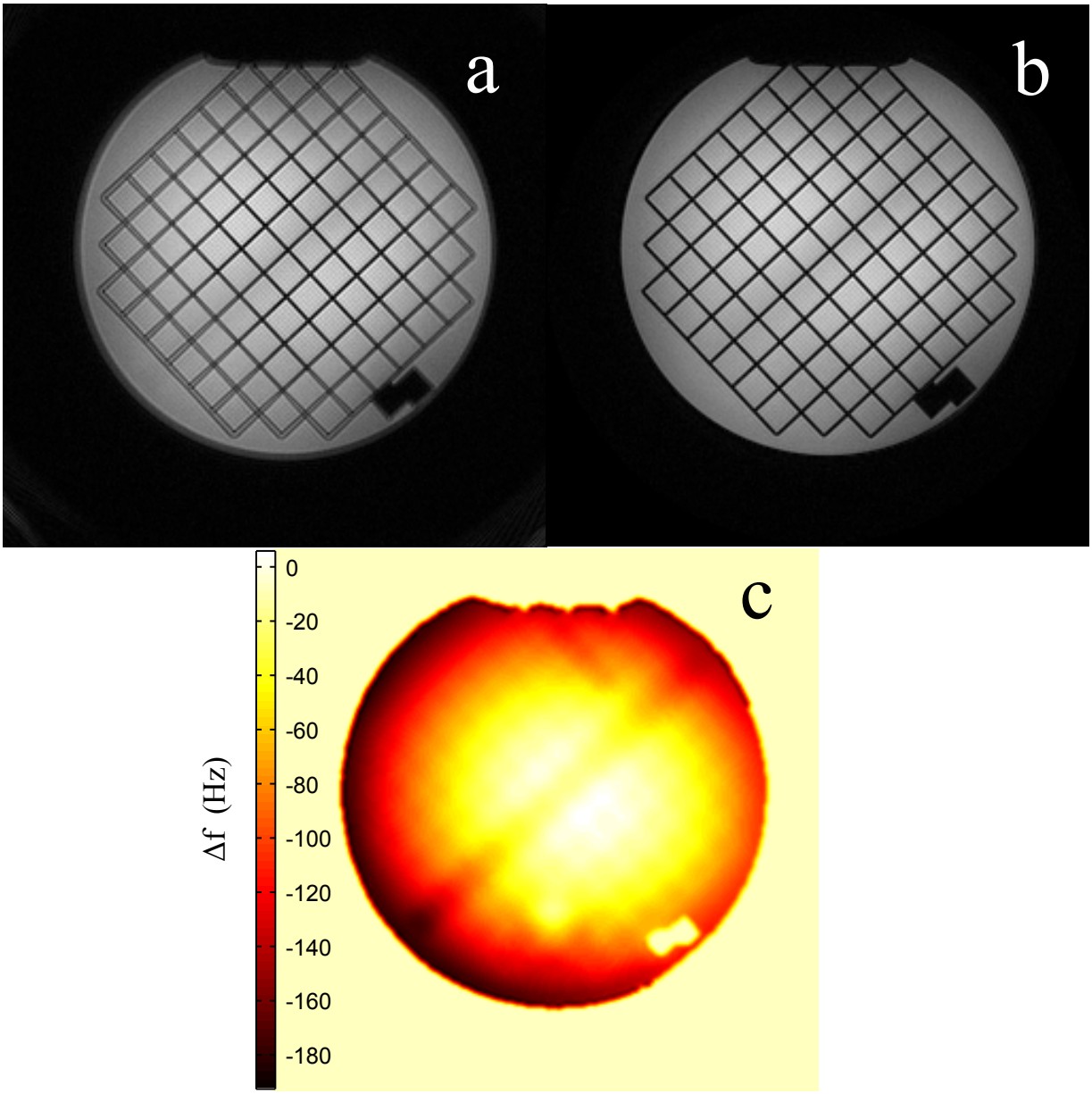

Figure 3.8: (a) Spiral image of the grid phantom acquired with second-order shims turned off. (L_{acq} = 256, N_I = 60, T_{acq} = 5.1 ms, FOV_d = 25 cm, T_R = 500 ms, T_E = 1.76 ms, 50° flip angle, and 3 mm slice thickness). Four segments were required, based on Eq. (3.27). (b) Deblurred image using FSORC. (c) The frequency-offset map using the scan parameters in (a) and $\Delta T_E = 4$ ms.

3.6.2 Obtaining the Frequency-Offset map

The most accurate methods of spiral image deblurring use a field inhomogeneity map (a.k.a. frequency-offset map), which can also typically be obtained by means of a gradient-echo spiral sampling scheme. Schneider et al. [50] show that a frequency-offset map is easily obtained by measuring the phase difference between the complex signal of two MR images, each acquired at a different echo time T_E. Mathematically, the frequency offset is calculated as

$$\Delta\omega = \frac{\angle(m_1^\star m_2)}{(T_{E2} - T_{E1})} \tag{3.29}$$

at each pixel, where m is the complex pixel value, and image 1 has the shorter echo time T_{E1}. As may be observed from Fig. 3.8(c), the phase map is blurry, partly because it is derived from two blurred spiral images, but mostly because it is also filtered by applying a 2D moving-average pillbox ($1 - 2$ pixels in radius) to decrease noise levels. If the blurring due to the off-resonance is not too excessive, it will not significantly alter the phase because it is assumed to be slowly-varying. Hence, a "rough" phase map may be obtained by means of two fast and/or low-resolution spiral scans [51], otherwise, an identical spiral scan (except for a longer T_E) may be used to correct the image with the shorter echo time as was done in Figs. 3.8(c), 3.9(b). Figure 3.9(a) shows the same grid phantom image as in Fig. 3.8(b), but this time, the FSORC was based on an off-resonance map obtained from only 4 interleaves, and $T_{acq} = 77$ ms, shown in Fig. 3.9 (d). We note that the absolute difference error in (c) between the two deblurred images is generally less than 10%, with a maximum pixel error of 20%, which is surprisingly low, considering a total scan-time reduction by 43% (2×30 s versus 30 s + 2×2 s). Excessive blurring also causes the field inhomogeneity map to spread outside the phantom as shown by the white region in Fig. 3.9(d), but this leads to errors of less than ± 40 Hz within the phantom region.

Phase unwrapping of the phase map $\angle(m_1^\star m_2)$ is necessary if the echo time is sufficiently long for the phase to wrap beyond the range of $[-\pi, \pi]$. Phase wrapping can be avoided by using a smaller echo time difference, but this results in a map with lower SNR. The implementation of a fast phase-unwrapping algorithm is often more time-consuming than the implementation of the FSORC technique itself, depending on the resolution of the spiral images. For example, Baldwin et al. [41] state that phase unwrapping in 3 dimensions took approximately one hour, given the dataset of $256 \times 160 \times 24$ voxels. The 2D Goldstein branch-cut phase unwrapping algorithm [52, 53] used in this thesis effectively unwraps a 256×256 image in 6 seconds, or a 128×128 image in 1.8 seconds. Considerable processing time may be saved by first down-sampling the phase map before unwrapping it, or acquiring a lower-resolution map, which does not result in an observable loss of accuracy given a slowly-varying phase (i.e., one where the maximum phase difference between two adjacent

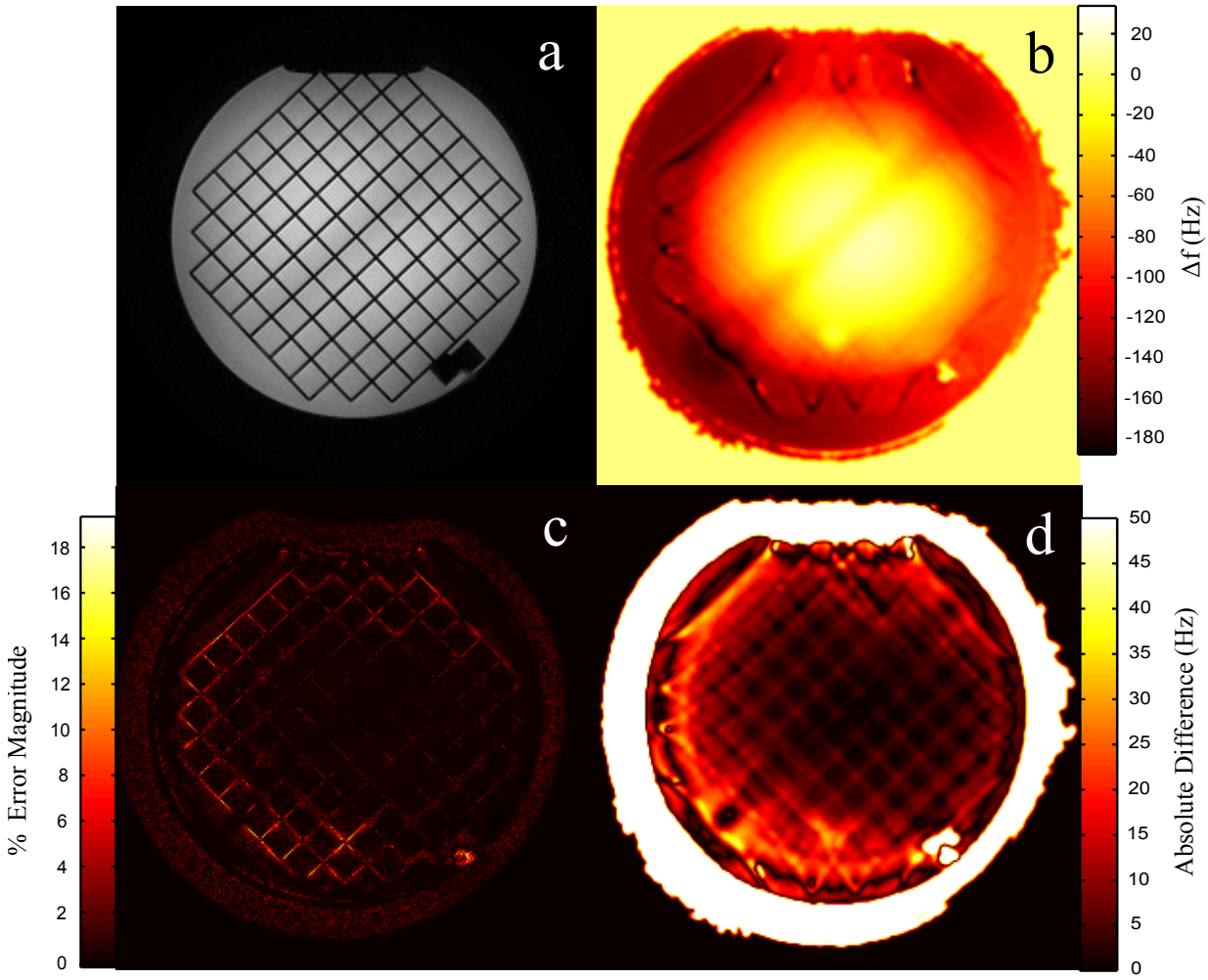

Figure 3.9: (a) Same image as in Fig. 3.8(b), but deblurred using the field inhomogeneity map in (b), obtained from a faster spiral scan with parameters: $N_I = 4$, $T_{acq} = 77$ ms, $L_{acq} = 256$, and $FOV_d = 25$ cm, $T_R = 500$ ms, and ΔTE = 4ms. (c) Percent error magnitude between the deblurred image in (a) and Fig. 3.8(b). (d) Absolute difference between the field inhomogeneity map in (b) and in Fig. 3.8(c).

pixels is less than ~ 0.125 rad). For a 256×256 image, FSORC took about 2.9 seconds for 4 segments, or 3 seconds for 29 segments (~ 2.5 s for gridding the time map $\boldsymbol{T}$ in Eq. (3.28), and ~ 0.4 s for the interpolation). Because the time map is the same for any slice, (provided that the trajectory is unchanged), an entire multi-slice dataset may be deblurred at a speed of ~ 2.5 s per slice.

3.7 The Effect of Concomitant Gradient Fields

According to Maxwell's equations, the net magnetic field $\boldsymbol{B}$ within an MRI bore must satisfy:

$$\frac{1}{\mu_0}\boldsymbol{\nabla} \times \boldsymbol{B} = \varepsilon_0 \frac{\partial \boldsymbol{E}}{\partial t} + \boldsymbol{J} \tag{3.30}$$

$$\boldsymbol{\nabla} \cdot \boldsymbol{B} = 0. \tag{3.31}$$

Since the displacement $\frac{\partial \boldsymbol{E}}{\partial t}$ and conduction current $\boldsymbol{J}$ are negligible for gradient fields in biological samples, Eq. (3.30) reduces to $\boldsymbol{\nabla} \times \boldsymbol{B} = 0$. These two vector equations may be expanded into the following four scalar equations [1]:

$$\frac{\partial B_x}{\partial x} + \frac{\partial B_y}{\partial y} + \frac{\partial B_z}{\partial z} = 0, \tag{3.32}$$

$$\frac{\partial B_x}{\partial y} = \frac{\partial B_y}{\partial x}, \tag{3.33}$$

$$\frac{\partial B_y}{\partial z} = \frac{\partial B_z}{\partial y}, \tag{3.34}$$

$$\frac{\partial B_z}{\partial x} = \frac{\partial B_x}{\partial z}, \tag{3.35}$$

which contain five independent partial derivatives, three of which are defined by the physical gradients: $\frac{\partial B_z}{\partial x} \equiv G_x$, $\frac{\partial B_z}{\partial y} \equiv G_y$, and $\frac{\partial B_z}{\partial z} \equiv G_z$. If we define a dimensionless parameter $\alpha \equiv -\frac{1}{G_z}\left(\frac{\partial B_x}{\partial x}\right)$, we then have $1 - \alpha = -\frac{1}{G_z}\left(\frac{\partial B_y}{\partial y}\right)$. A transverse term may also be defined as $G_\perp \equiv \frac{\partial B_x}{\partial y} = \frac{\partial B_y}{\partial x}$. For an MRI scanner equipped with cylindrical gradient coils, where x, y, z are the physical gradient coordinates, $\alpha \approx 0.5$ and $G_\perp \approx 0$ [1]. If we perform a second-order Taylor series expansion of the overall field

$$B(x, y, z) = \sqrt{B_x^2 + B_y^2 + B_z^2}, \tag{3.36}$$

we obtain the following approximation [1]

$$\begin{aligned} B &= B_0 + G_x x + G_y y + G_z z \\ &\quad + \frac{1}{2B_0}\left[\frac{G_z^2}{4}\left(x^2+y^2\right) + \left(G_x^2+G_y^2\right)z^2 - G_x G_z xz - G_y G_z yz\right], \\ &= B_0 + \boldsymbol{G}\cdot\boldsymbol{r} + B_c, \end{aligned} \tag{3.37}$$

where B_c is known as the *concomitant* field term. The concomitant term is always a positive quantity in MRI, and may result in various image artifacts, depending on the pulse sequence, and the slice position and/or orientation used. In spiral MRI, the concomitant term results in an additional phase accumulation of the signal, given by [1]

$$\phi_c = \gamma \int_0^{T_{acq}} B_c(G_x, G_y, G_z, x, y, z)dt. \tag{3.38}$$

Because the concomitant field strength B_c is inversely proportional to the static field strength B_0, and proportional to the square of the gradient strengths G_x, G_y and G_z, the effects on the Philips 3T scanner (with gradient strengths limited by the software to 21 mT/m) are barely noticeable, compared to those at 1.5 T. In fact, concomitant field corrections are typically noticed at fields of 1.5 T or less [29, 30, 48], or with much larger gradient strengths. Spiral scans with acquisition times in the order of 12 ms were taken in the axial, coronal and sagittal plane and reconstructed with FSORC to check for observable blurring due to concomitant fields. Only an axial image with a large slice offset of $z_c = -11.7$ cm showed some blurring due to concomitant fields (see Fig. 3.10(a)).

Fortunately, blurring in the axial plane is readily corrected. Since G_z is inactive during the readout, the concomitant phase is

$$\phi_c(t,z) = \frac{\gamma z^2}{2B_0}\int_0^t \left[G_x^2(t') + G_y^2(t')\right]dt', \tag{3.39}$$

and the signal acquired in Eq. (2.33) becomes

$$S(t) = \int_V m(\boldsymbol{r}) e^{-i(\boldsymbol{k}(t)\cdot\boldsymbol{r} + \phi_c(t,z))} d^3r. \tag{3.40}$$

For 2D imaging, the phase dispersion across the slice will result in a signal loss that is not explicitly shown in Eq. (3.40). However, according to King et al. [30] it is not observable for slice thicknesses of less than 1 cm, slice offsets of less than 10 cm and gradient strengths of less than 22 mT/m. Thus, the time dependence may be factored out of the integral, and Eq. (3.40) reduces to

$$S(t) = e^{-i\phi_c(t,z_c)} \int_V m(\boldsymbol{r}) e^{-i(\boldsymbol{k}(t)\cdot\boldsymbol{r})} d^3r. \tag{3.41}$$

Figure 3.10(a) shows blurring arising from concomitant fields in the axial plane, after FSORC was applied in order to remove all the blurring due to B_0 field inhomogeneity. Blurring is fully removed in (b), after applying both FSORC and demodulation of the signal with the conjugate concomitant phase $\phi_c(t, z_c)$.

3.8 3D Imaging

Three-dimensional MR acquisitions may be advantageous over 2D MRI, in that high-SNR T_1-weighted images with sub-millimeter isotropic resolution may be achieved in one experiment. Recently, 3D MRI scan protocols have been used for radiation therapy treatment planning [54]. Efficient 3D MRI may be performed by sampling κ-space using a stack of 2D spirals in the xy-plane, with phase-encoding along the z direction. Image deblurring by means of FSORC proceeds the same way as in the 2D case, after the 3D dataset has been reconstructed into a stack of axial slices, along with their unwrapped 2D field inhomogeneity maps. A true 3D spiral acquisition was not considered in this thesis, because although the overall acquisition time would be reduced, the image reconstruction and post-processing time would increase significantly, as both gridding and deblurring would have to be performed in 3D.

3.8.1 Phantom Study

In order to assess the image quality of 2D spiral with 1D phase-encoding MRI and compare it to an equivalent 3D Cartesian MRI, four 3D image datasets were taken on the ACR phantom using the same FOV of $240 \times 240 \times 125$ mm^3, and an 8-channel head array coil operated in quadrature mode. The first dataset consisted of a high-resolution ($0.98 \times 0.98 \times 1$ mm^3) spiral scan (N_I = 64, T_{acq}= 4.7 ms, T_R = 16 ms, T_E = 1.4 ms, α = 13°, NEX = 3, scan time = 8:09). The second and third datasets were low-resolution ($2 \times 2 \times 1$ mm^3) spiral scans acquired at two different echo times for the purpose of creating a stack of 2D field inhomogeneity maps (N_I = 8, T_{acq} = 10 ms, T_R = 16 ms, T_{E1} = 1.4 ms, T_{E2} = 4.4 ms, α = 13°, NEX = 2, T_{scan} = 1:30). The fourth dataset was a high-resolution ($0.94 \times 0.94 \times 1$ mm^3) magnetization-prepared gradient echo (TFE in Philips nomenclature) Cartesian scan, with a minimum acquisition bandwidth (TFE factor = 64, T_R = 16 ms, T_E = 4 ms, α = 13°, NEX = 1, scan time = 8:59). The 3D datasets were reconstructed on-line into 125 contiguous axial slices of 1 mm thickness, and the high-resolution spiral dataset was deblurred off-line using the same FSORC algorithm programmed in MATLAB, following phase unwrapping of the 125 low-resolution field-inhomogeneity maps of 128×128 pixels. The total post-processing time was 5:20 minutes. The deblurred spiral images (a,

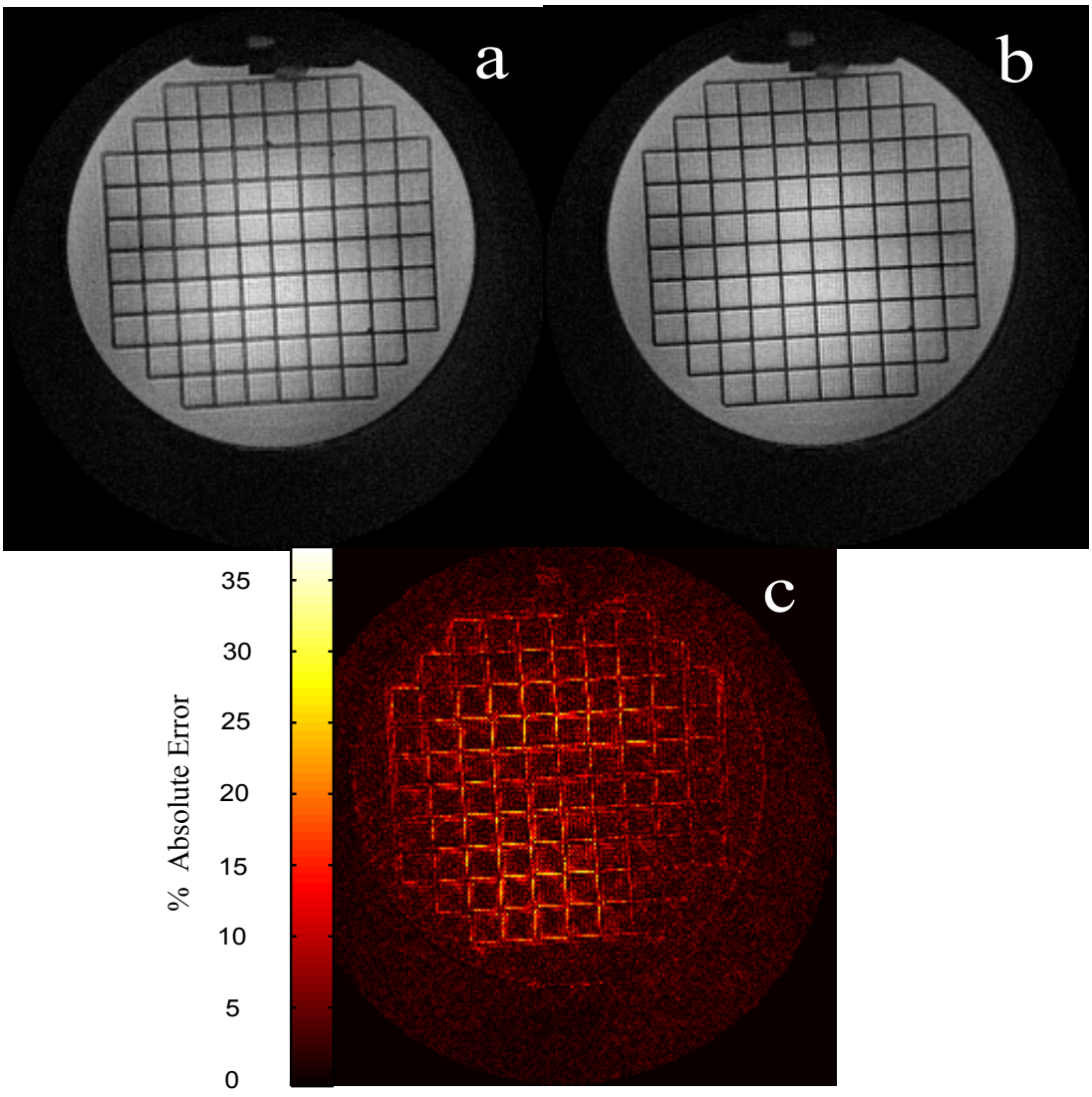

Figure 3.10: (a) Axial image (slice offset of $z_c = -11.7$ cm) with FSORC applied, showing the remaining blurring due to concomitant gradient fields. (b) Same image reconstructed with both FSORC and concomitant phase correction. (c) Absolute percent error between the image in (a) and (b).

c, e), along with the Cartesian images (b, d, f) are displayed in Fig. 3.11 for slice #10, 61 and 110. The SNR was measured at the center of slice #78, at which point the combined coil-sensitivity profile and B_1^+ field is approximately uniform. Measurement of the mean signal and noise standard deviation within a square (region-of-interest) ROI of ~ 1000 pixels at the centre of the image, yielded SNRs of ~ 100 and ~ 90 for the spiral and Cartesian image, respectively.

A close examination of images (a-f) reveal that the spiral images contain less Gibbs ringing, and no distortion compared the their Cartesian counterparts. The circles within the spiral image of slice #110 have less T_2^* contrast, compared to those of the Cartesian image because of the shorter T_E used in the spiral sequence. This problem may be overcome by using a longer T_E of 4 ms for the spiral acquisition. One may also notice a slightly poorer definition because the field inhomogeneity map is filtered and too low in resolution to resolve the slight field inhomogeneity differences arising from the water-plastic interfaces. A higher-resolution off-resonance map could be performed as a remedy, but at the cost of a longer post-processing time. The spiral image of slice #110 also contains an half-moon shaped artifact close to the center of the image, which is probably caused by higher-order stimulated echoes due to imperfect signal spoiling. The difference between the magnitude spiral image and Cartesian image of slice #61 is shown in Fig. 3.12(a) (spiral minus Cartesian image). The maximum geometrical distortion of the Cartesian image is in the order of $\sim$ 1mm (one pixel). Figure 3.12(b) shows the mirrored Cartesian image quarter section next to the spiral image quarter section in (c) in order to facilitate the visualization/comparison. Because the distortions occur along both the phase-encode and frequency direction, the image appears translated along the diagonal by about 1 mm. Since the distortions of the 3D Cartesian image dataset are not readily observed, an example is also provided in Fig. 3.16 for a single-slice 2D acquisition, where the deblurred spiral image contains no visible distortions compared to the equivalent Cartesian echo-planar image (EPI) acquired with similar scan parameters. The EPI image could also be corrected using a field-inhomogeneity map, but the map would have to be derived from a different pulse sequence, which can potentially result in two geometrically inconsistent datasets.

3.8.2 Invivo Exam

In order to demonstrate the ability of spiral MRI to provide geometrically-accurate high-resolution brain images, I performed a 3D *in vivo* brain exam on a healthy volunteer with a spiral protocol very similar to the previous phantom study (exceptions: $T_E = 4$ ms, $\alpha = 15°$, NEX = 4, $T_{scan} = 10{:}47$). Phase unwrapping and image deblurring by FSORC was performed slice by slice on the first 105 slices of the spiral dataset. The last 20 slices were not included because they fell outside the brain region. Figure 3.14 displays the field

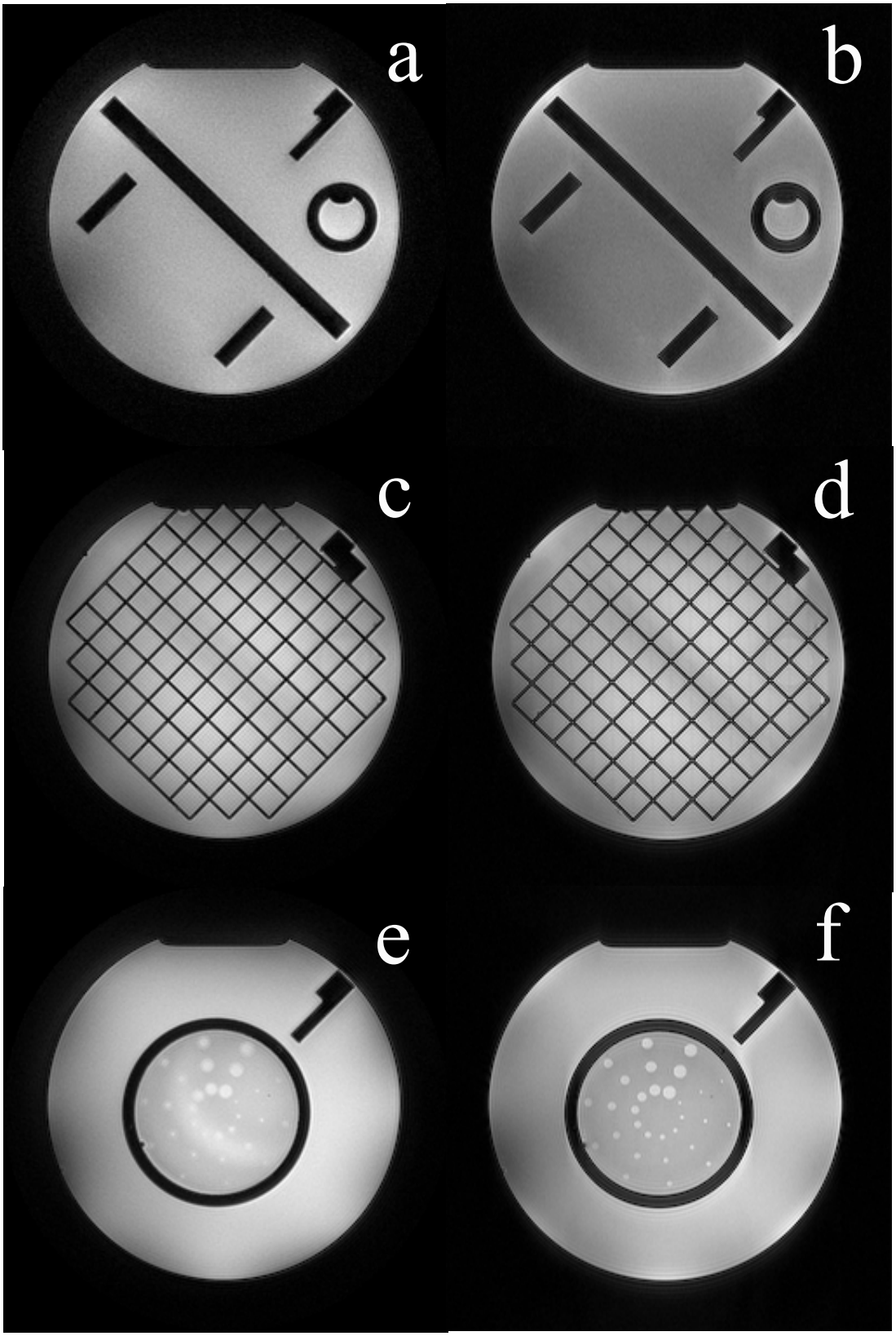

Figure 3.11: Deblurred spiral images (a, c, e), compared to the corresponding Cartesian images (b, d, f) for slice # 10, 61 and 110 (3D acquisition).

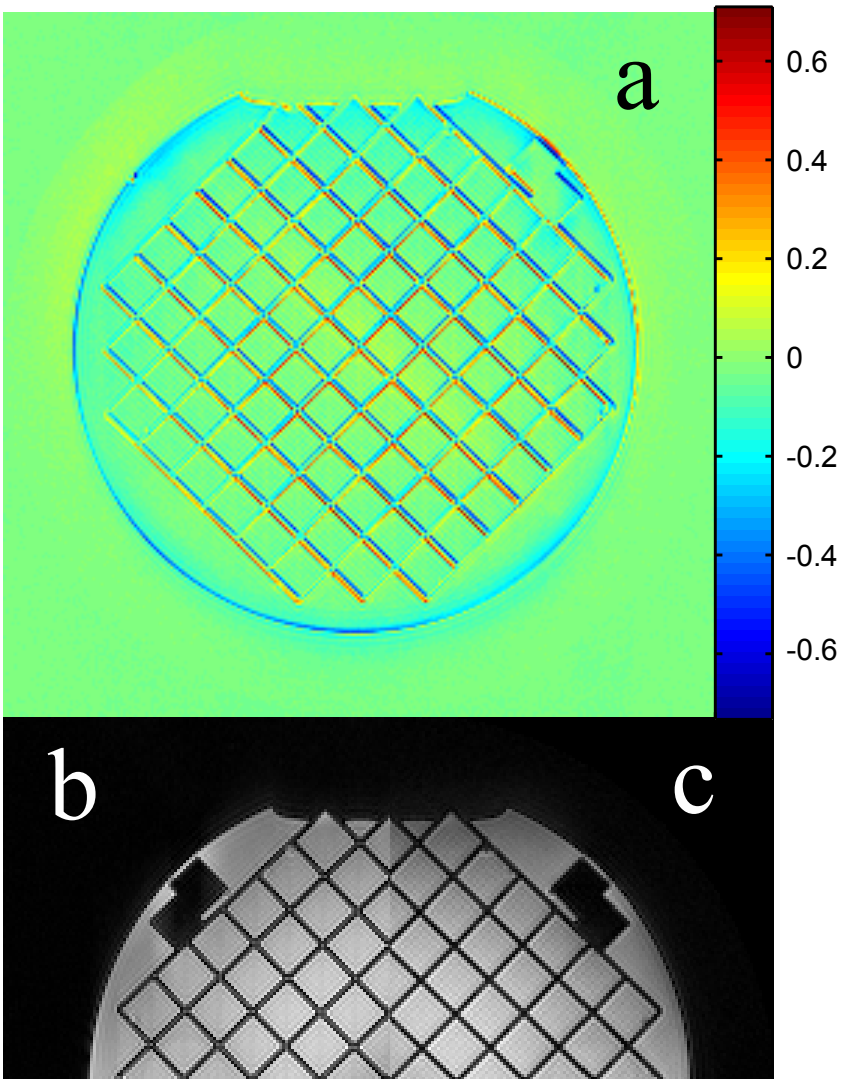

Figure 3.12: (a) Pixel intensity difference: normalized spiral minus normalized Cartesian image of slice #61. (b) Mirrored Cartesian quarter section. (c) Spiral quarter section.

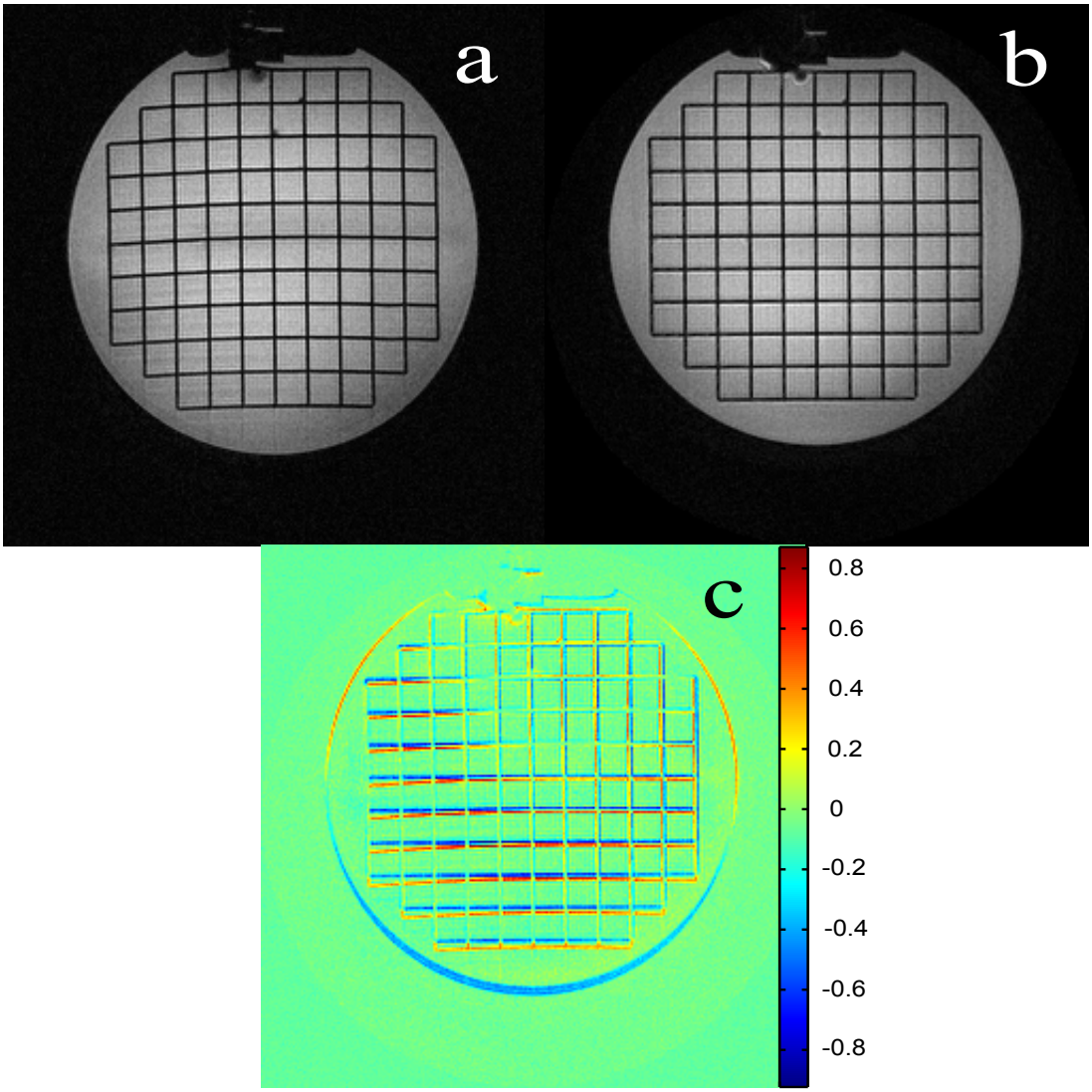

Figure 3.13: (a) EPI image acquired with 20 interleaves, ($\alpha = 25°$, $T_R = 24$ ms, $T_E = 11$ ms, $FOV = 25 \times 25$ cm^2, 256×256 pixels). (b) Deblurred spiral image acquired with 20 interleaves, ($\alpha = 25°$, $T_R = 25$ ms, $T_E = 1.54$ ms, $T_{acq} = 15$ ms, $L_{acq} = 256$, $FOV_d = 25$ cm, $\Delta T_E = 6$ ms. (c) Normalized spiral image minus the normalized EPI image, showing the pixel intensity difference. The severe distortions are clearly visible in the EPI image, and virtually absent in the spiral image.

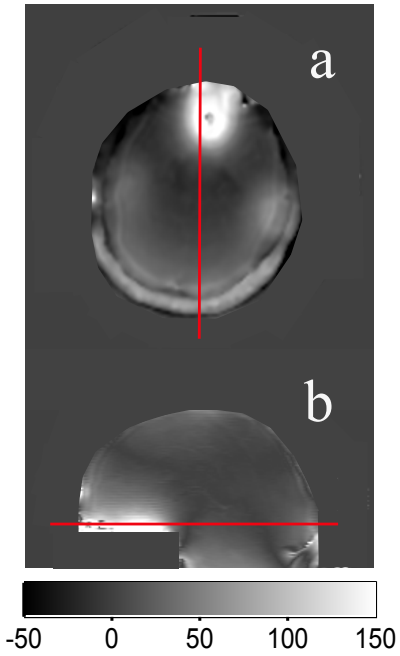

Figure 3.14: Field inhomogeneity map (in Hz), shown in both the axial (a) and sagittal (b) orientation. The red lines indicate the approximate relative locations of the two slices.

inhomogeneity map in both the axial (a) and sagittal (b) plane. The smoothly-varying field inhomogeneity in the sagittal plane demonstrates that the phase unwrapping of a 3D dataset may be effectively performed in 2D, with a significant reduction in post-processing time, provided that the SNR of the two low-resolution spiral datasets is sufficiently high to produce an accurate phase map. One may observe how the strong field-inhomogeneity difference of over 150 Hz close to the nasal cavity in the frontal lobe (Fig. 3.14), results in a blurred artery (Fig. 3.15(a)). Figure 3.15 compares the raw spiral image with the deblurred image for the same axial slice #30 shown in Fig. 3.14(a).

A 3D Cartesian scan protocol with similar scan parameters was also performed on the same volunteer with the same FOV and pixel resolution for comparison (T_E = 4 ms, T_R = 10 ms, $\alpha = 12°$, NEX = 1, T_{scan} = 11:13). The α, T_R, and NEX were selected to yield a SNR, contrast and T_{scan} comparable to the *in vivo* spiral protocol described above. Figure 3.16 displays a maximum intensity projection (MIP) of the deblurred spiral dataset in (a) for comparison with the Cartesian dataset in (b). The MIP derived from the spiral dataset generally resolves the arteries better than its Cartesian counterpart.

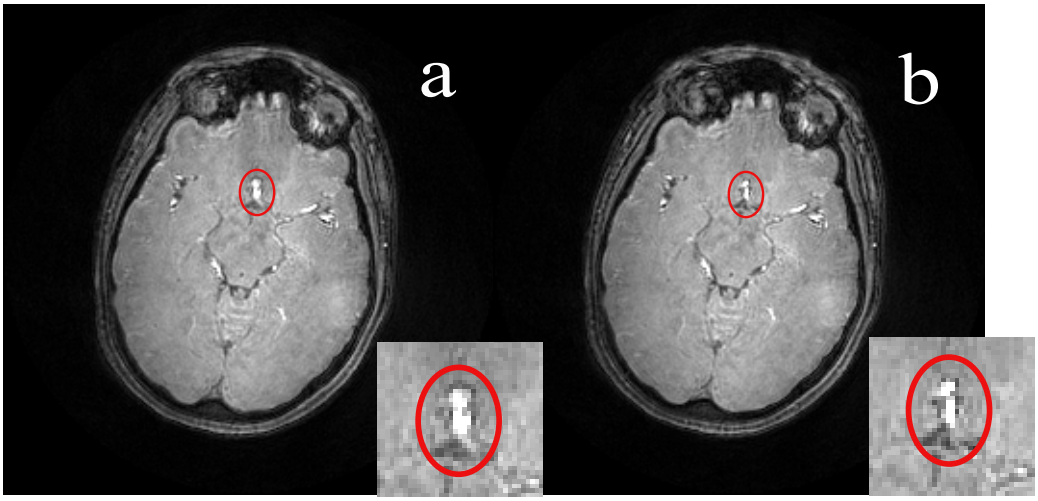

Figure 3.15: Uncorrected *in vivo* spiral image (a) and deblurred spiral image (b) of slice # 30. The resolution in this region is successfully recovered in the deblurred image (red circle).

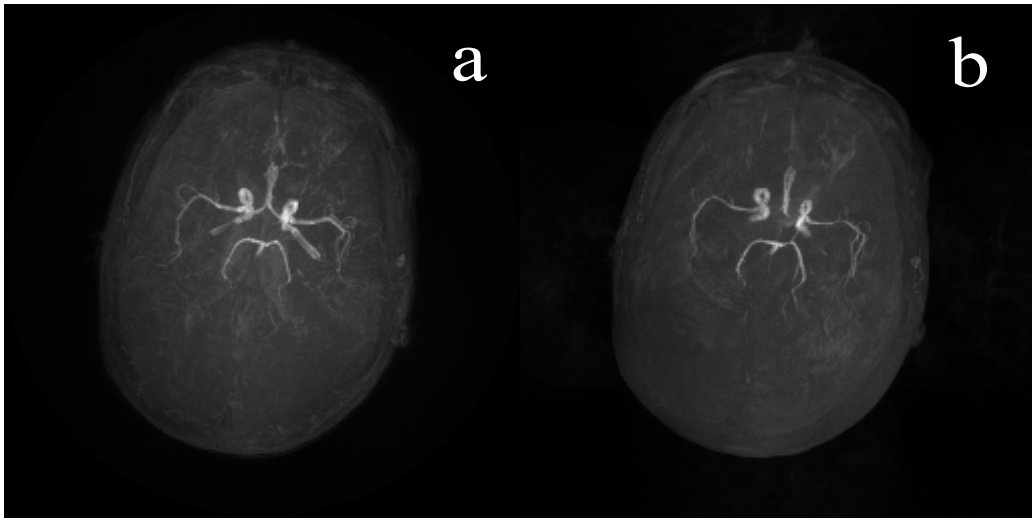

Figure 3.16: MIP of the spiral dataset in (a) compared with the Cartesian dataset in (b), derived from the same volunteer/dataset as in Fig. 3.15.

3.9 Conclusion

This chapter has concisely outlined the theory of spiral MR image acquisition, reconstruction and post-processing, and serves as general background for chapter 4. I demonstrated that spiral MRI can provide accurate phantom and *in vivo* images, provided that certain technical considerations are met. We first saw that the κ-space sampling trajectory must be accurately modeled. A time delay must also be tuned and taken into account as part of the image reconstruction in order to correct for gradient delays and eddy-current effects. An accurate and fast image reconstruction algorithm must be employed, such as the NUFFT. Finally, scan parameters including T_{acq}, N_I, L_{acq} and FOV_d must be chosen, along with an accurate high-order shim in order to avoid image blurring. Alternatively, the blurring may be removed through post-processing using a field-inhomogeneity map.

CHAPTER 4

Efficient Multichannel Coil Data Compression: A Prospective Study for Distributed Detection in Wireless High-density Arrays[1]

4.1 Introduction

The use of high-density receive array coils (i.e., those where the number of elements contained within the field-of-view (FOV) is large) is becoming more common in magnetic resonance imaging (MRI) to take advantage of improved signal-to-noise ratio (SNR) over a large imaging volume [23], as well as to perform accelerated imaging through parallel techniques [56–58]. Large coil arrays of up to 128 channels have been demonstrated [10–12] and can lead to situations whereby MR data storage limits are reached along with the increased computational burden and image reconstruction time posed by a large number of channels [see, e.g., Refs. 12, 59]. Some reduction in data is achievable by appropriate combinations of individual channels [60, 61]. Nevertheless, as the number of channels increases, electromagnetic coupling between coils and the coaxial cables that carry MR signals becomes increasingly challenging to manage [59, 62], with consequent safety issues and cross-talk among channels.

Various approaches have been considered to replace coaxial cables with wireless links [59, 63] or optical fibers [64, 65]. Both transmission methods can support analog or digital information. Analog transmission of MR signals with performance similar to that of coaxial cables requires meeting very stringent dynamic range and noise figure performance specifica-

[1] A version of this chapter has been published in Concepts in Magnetic Resonance Part B 39B (2):64-77. (2011) [55]

tions [59, 66, 67] that test the limits of current technology. Conversely, digital transmission methods are sufficiently advanced that MR data could readily be transmitted if digitization were performed at the coil. Fiber connections are fastest but may be impractical due to the high cost of reliable high-density optical connectors, as well as the fact that being tethered limits optical fibers use in highly ergonomic wearable designs such as those of Ref. [68]. For the truly wireless solution [59] numerous digital transmission standards exist but all have data rates that can be exceeded (e.g., 54 Mbps based on IEEE 802.11a) if a large number of channels is used, especially if fast dynamic scanning is required which limits the possibility of buffering the data. Hence, if wireless high-density arrays are to become practical, the data to be transmitted to the reconstruction unit should be compressed.

In recent years, advances in the performance of analog-to-digital converters (ADCs) have allowed direct sampling of radio frequency (RF) signals [67, 69, 70], thus eliminating the traditional analog detection front-end and its sensitive circuitry. This simplified architecture naturally leads to considering a digital acquisition system (spectrometer) design whereby digitization occurs in separate modules at each of the coils, rather than in a cabinet in the equipment room. This "distributed" spectrometer would require not only an ADC at each coil but also digital signal processing devices to perform filtering, demodulation, and decimation (i.e., signal detection) that result in the familiar rotating-frame MR signal. These signal processing devices could also support additional operations aimed at compressing the MR data prior to transmission over the wireless link therefore allowing the full benefits of high-density arrays to be exploited while avoiding limitations in wireless data transmission rates.

In this work, we show through both simulations and phantom experiments how the bulk of the data can be reduced to one-third or less of the original amount while preserving equivalent image quality. We achieve this in spiral MRI by spectral compression using coil-wise dynamic demodulation [71], and by bit-depth reduction following dynamic range compression. These reductions are independent and fully compatible with those achieved by parallel imaging techniques [56–58, 72]. They are also compatible with channel combination [60, 61], with the advantage that in a distributed spectrometer architecture, our methods reduce the data at each individual coil module while channel combination cannot, since it must be performed in a location where all coil signals are present. Finally, even without restrictions on data transmission rates, the data compression methods may also be used to reduce the total archival memory storage requirements in scans that use a large number of channels.

4.2 Theory

4.2.1 Imaging with Limited Coil FOV

High-density coil arrays offer the opportunity to reduce the amount of signal data for each acquisition interleaf based on the fact that each coil sees an effective FOV that may be substantially smaller than that of the full acquisition. Gradients present during acquisition will correspondingly spread the MR signal over a band of frequencies that is proportional to the coil's FOV and thus smaller than that required for the full FOV. Therefore, a reduction of signal data that depends on the size of the sensitivity profile of the coil relative to that of the object is possible. If coil sensitivity does not fall to zero beyond the chosen bandwidth limits, redundancy due to overlap of coil sensitivities in the array ensures that image quality is preserved even if some low-level signal is lost or distorted.

In a standard system, the signal picked up by each individual coil is demodulated at a frequency corresponding to that at the centre of the common FOV (Fig. 4.1(a)). Consequently, for coils at the edge of the FOV, the signal spectrum will be shifted from this center frequency and will require a large acquisition bandwidth despite the fact that a small, localized sensitivity profile leads to a smaller signal bandwidth. Similarly, coils near the centre of the FOV will be assigned unnecessarily large bandwidths due to their inability to see the entire imaging FOV. Signal acquisition can therefore be made more efficient, with a reduction in the amount of data required for image reconstruction, by demodulating the signal using the frequency at the centre of each coils individual sensitivity profile and low-pass filtering, thus assigning a separate FOV to each coil.

4.2.2 Dynamic Demodulation

In an arbitrary κ-space sampling trajectory, the centre frequency of each coil varies at each sampling instant in proportion to the applied gradients. In the standard direct-sampling receiver architecture (Fig. 4.1(a)), the RF signal is sampled typically below the Nyquist rate of the Larmor frequency and digitally processed to extract the desired complex MR signal from one of the resulting aliases [67, 69, 70]. All channels are demodulated at the same fixed frequency ω_0 corresponding to the same image center and filtered with a bandwidth corresponding to the full FOV. In the more flexible receiver chain of Fig. 4.2, the signal from each coil can be demodulated and filtered based on the individual FOV corresponding to the position and sensitivity pattern of each coil. The dynamic demodulation technique was introduced by Lee et al. [71] and applied to avoid aliasing artifacts in the spiral version of the parallel imaging with localized sensitivities (PILS) technique [72]. In this work, we

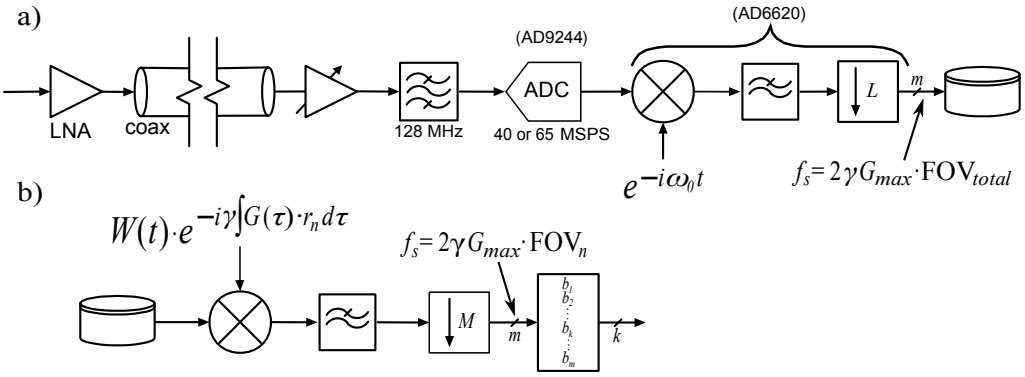

Figure 4.1: In a modern MRI receiver chain (a), the signal from each coil is amplified through a low-noise amplifier (LNA), transmitted via a coaxial cable, and band-pass filtered prior to being digitized (at several tens of megasamples/s, MSPS) in an analog-to-digital converter (ADC) and demodulated by direct digital conversion. The signal from each coil is demodulated using the same common demodulation frequency ω_0 corresponding to that at the centre of the image FOV. Final antialias low-pass filtering and decimation by a factor L are applied to produce the desired MR signal. Devices AD9244 and AD6620 are examples of integrated circuits by Analog Devices (Norwood, MA) that perform the corresponding functions. In our implementation the raw signal stored in the system memory is processed off-line (including storing data as integers) using MATLAB (The MathWorks, Natick, MA) as shown schematically in (b) to emulate the distributed spectrometer architecture of Fig. 4.2.

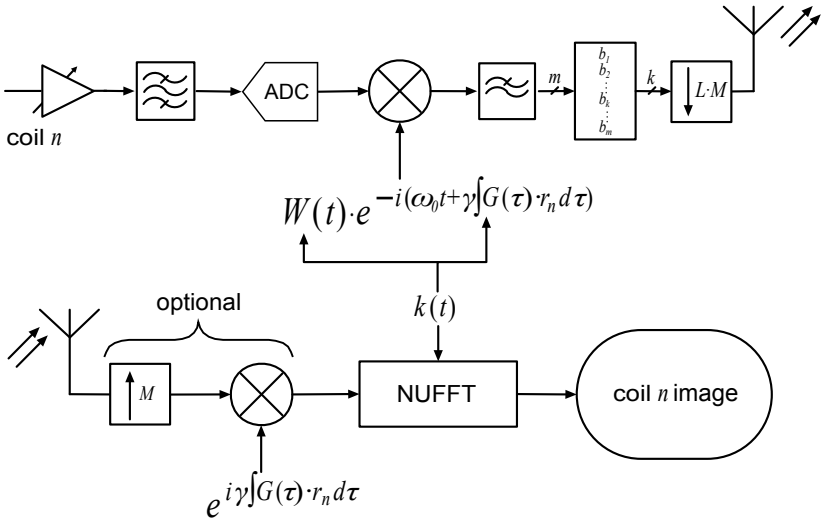

Figure 4.2: In the proposed MRI receiver chain, the signal from each coil is demodulated by a separate demodulation frequency waveform, corresponding to an FOV centered on each coil's sensitivity profile. To reduce the amount of data, the sampling density compensation $W(t)$ is applied to the digital signal prior to transmission, thus compressing the dynamic range such that the m-k least significant bits can be ignored following the low-pass filter. Similar to the standard receiver, decimation by a factor L is required to bring the sampling frequency down to the kHz range, with additional downsampling by the compression factor M. The resulting data are transmitted over a wireless or fiber-optic digital transmission link. After reception (below), the signal can be upsampled by the factor M to preserve κ-space sampling density and finally remodulated prior to gridding and reconstruction.

use dynamic demodulation to compress the spectrum and reduce the amount of data in each interleaf for the purpose of more efficient transmission via a wireless link by low-pass filtering and downsampling the signal by a factor M relative to the full acquisition (Fig. 4.2). Any parallel imaging acceleration would be in addition to what we describe here. In the most general case, the coil-wise demodulation frequency $\omega_n(t)$ is given by

$$\omega_n(t) = -\gamma \mathbf{G}(t) \cdot \mathbf{r}_n - \omega_0 \tag{4.1}$$

where γ is the gyromagnetic ratio for protons, $\mathbf{G}$(t) is the gradient strength vector, $\mathbf{r}_n$ is the position of the centre of the n^{th} channel's FOV after dynamic demodulation, and ω_0 is the demodulation frequency at the origin.

The demodulated signal $s_n^d(t)$ for coil n is then given by

$$s_n^d(t) = s_n(t) e^{i \int \omega_n(t) dt}. \tag{4.2}$$

Alternatively, the demodulated signal may be expressed in terms of the κ-space position vector $\kappa(t)$ by integrating the gradient waveforms

$$\kappa(t) = \gamma \int_0^t \boldsymbol{G}(\tau) d\tau, \tag{4.3}$$

resulting in

$$s_n^d(t) = s_n(t) e^{i(\boldsymbol{\kappa}(t)\cdot \mathbf{r}_n - \omega_0 t)}. \tag{4.4}$$

This expression may be interpreted as the Fourier shift theorem generalized to an arbitrary κ-space trajectory, and the subsequent low-pass filtering has the effect of reducing the diameter of the unaliased FOV by a factor M [71]. The centre offsets $\mathbf{r}_n$ must therefore be chosen so that the superposition of all the individual FOVs after spectral compression will cover the imaging object sufficiently (refer to Fig. 4.4(b)). The offsets can be chosen by methods that are based on coil geometry alone (in our examples, at equal angular intervals around a suitable radius), or based additionally on the imaging object's shape and its effect on coil sensitivity. In the following, the offsets are chosen equal to the centroid (center of mass) of the corresponding coil's sensitivity pattern in the presence of the phantom. Finally, we note that spectral compression works with any slice orientation as long as there are enough coils with sufficient sensitivity in that slice so that reduced FOVs and offsets can be found to cover the imaging object.

Figure 4.3(a) displays the effect of demodulating the signal on its spectrum, which is to "squeeze" the signal information from all 16 coils to the centre of the bandwidth (green), compared to the much wider bandwidth occupied by the original signal (black).

As shown schematically in Fig. 4.2, this dynamic demodulation can be performed digitally at each separate coil element by using an appropriate fast processing device such as a field-programmable gate array or application-specific integrated circuit. The waveform of Eq. (4.2) would then be uploaded to the corresponding module before the scan along with the corresponding centroid and frequency of Eqs. (4.1) and (4.4). The centroids of the coil profiles are readily calculated from the sensitivities measured during a prescan similar to that used for SENSE reconstruction [57]. Alternatively, dynamic demodulation can be implemented as an additional processing step (Fig. 4.1(b)) on the more traditional filtered and downsampled data at the output of Fig. 4.1(a), which we perform in this work for the purpose of emulating the effect of the proposed receiver architecture presented in Fig. 4.2.

4.2.3 Dynamic Range Compression

Efficient digital transmission of analog signals necessarily imposes limits on the dynamic range that is supported due to the need to represent each sample using a limited number of

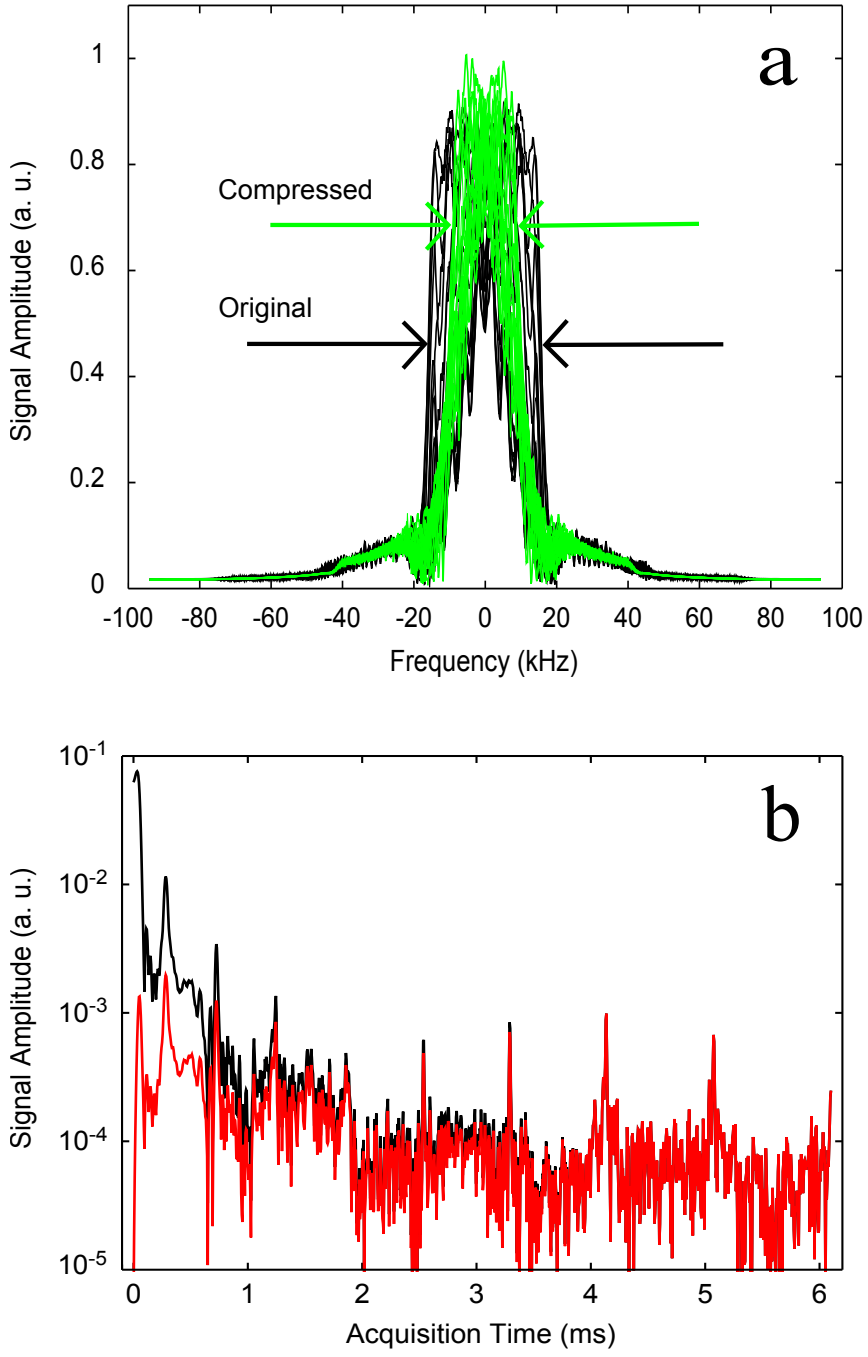

Figure 4.3: Data from a simulated spiral acquisition using 16 coils and 60 interleaves: (a) overlaid spectra of the original raw signals (black) and dynamically demodulated signals (green) of one interleaf from all coils. The density compensation is not included. Dynamic demodulation has the effect of squeezing the signal to the centre of the sampling bandwidth thus preserving information that would otherwise be lost or result in aliasing if the raw signal were directly low-pass filtered and downsampled. (b) Signal (from a single channel) with sampling density compensation (red) has a dynamic range of 27.5 dB or approximately five bits lower than that of the raw signal (black).

bits. In MR, the dynamic range of the signal (in dB) is given by [66]

$$DR_{signal} = 20 \log \left(\frac{2S_0}{\sigma} \right), \tag{4.5}$$

where S_0 is the peak of the signal amplitude (which typically occurs at the centre of κ-space) and σ is the noise standard deviation of the signal. The factor of two accounts for the fact that the signal may be either positive or negative. Dynamic range supported by the ADC (also in dB) may be expressed in terms of the number of bits, m [66]:

$$DR_{ADC} = 20 \log \left(2^m\right) \cong 6.02m. \tag{4.6}$$

MR signals during a given scan are well-known to cover dynamic ranges of 90 dB or more for 3D scans. However, in a system where amplification is fixed before transmission out of the magnet bore (e.g., that of Fig. 4.1), the dynamic range calculation must refer to the extremes of maximum signal resulting from uniform excitation of all spins in the coil's FOV, relative to that of the smallest noise magnitudes Eq. (4.5) expected during a low-bandwidth spectroscopic acquisition. With this unrealistic definition the dynamic range requirements on the transmission system readily exceed astronomical values of 150 dB or more [66], which can be supported only by passive cabling (i.e., coax) rather than active transmission devices. Clearly, then, the solution is to place the system's scan-specific gain adjustment before the signal transmission stage as done in Fig. 4.2 and bring dynamic range down to values that are compatible with the 16 bits of current RF ADCs.

The reduction in dynamic range of MRI data has prompted numerous, but uncommon, approaches over the years, including sequence modifications [73], using two separate ADCs per channel [74] and hardware compression [75]. For Cartesian MRI, it is common in some systems to use profile-dependent amplification [66], whereby read-out lines near the centre of κ-space are acquired with lower gain settings. This method typically allows an increase of roughly three bits in the effective dynamic range supported by the system [66]. The idea can be extended by adding more steps to the gain setting, thus achieving a gain adjustment that is optimized for each interleaf [76]. However, profile-dependent amplification is not used in non-Cartesian sampling trajectories or echo-planar imaging due to the limited speed with which variable attenuators can switch reliably.

In this work, we reduce the dynamic range of the data from non-Cartesian sampling trajectories by applying the κ-space sampling density compensation [38] to the signal prior to its transmission to the reconstruction unit. The sampling density compensation function, denoted by *W(t)* in Figs. 4.1(b) and 4.2, depends entirely on the κ-space trajectory, which can be calculated prior to the start of the sequence and uploaded to the individual

coil modules together with the demodulation waveform of Eq. (4.3) and $\mathbf{r}_n$. Multiplication of the signal by *W(t)* can be performed in the same digital processing device as the dynamic demodulation and followed by bit-depth reduction (and consequent data compression) through removal of the $m-k$ least significant bits of each data sample (Fig. 4.2). The total amount of data reduction including spectral compression and bit-depth reduction may be summarized as $1-k/m \cdot M$, where $k/m \cdot M$ is the ratio of final to initial amount of data. Figure 4.3(b) illustrates the signal from one coil plotted for one interleaf on a logarithmic scale with and without the sampling density compensation, showing a 27.5 dB decrease in dynamic range (see §4.4). Data can therefore be represented with approximately five fewer bits Eq. (4.6) than would be needed for the uncompressed signal.

For Cartesian, as well as non-Cartesian trajectories, *W(t)* could also be a nonlinear compression characteristic implemented in software rather than in hardware as done in Ref. [75] or a generalization of profile-dependent amplification [66]. A method to optimize gain for each phase-encode line is described in Ref. [76], which can be implemented in software and generalized to each κ-space sample if a heuristically determined weighting function is used to predict signal amplitude variations across κ-space. In these cases the compression would need to be reversed by applying the inverse weighting before reconstruction (not shown).

4.2.4 Image Reconstruction

At the other end of the wireless link (lower part of Fig. 4.2), the signal can be optionally upsampled by the same factor M to recover the original sampling rate. While resampling comes at the cost of a longer gridding reconstruction time, our experience is that it yields images less prone to gridding artifacts than by directly gridding the downsampled signal onto the original size of the data matrix. As a final step, the signal from each coil may be either remodulated to shift the image to its original location and then reconstructed, or reconstructed without remodulation and shifted in the image domain. The latter option is possible only if the image shift due to modulation coincides with an integral number of pixels in the final combined image and may lead to image truncation errors. Combination of the images from individual coils can be performed by root-sum-of-squares (RSS) or other methods [72].

Spectral compression is equally applicable to all types of non-Cartesian sampling patterns, such as radial [77] or spiral. Spiral images in the following examples were acquired using the trajectory described by Boernert et al. [29], which accounts for hardware limitations in slew rate and gradient strength by varying the spiral's κ-space velocity. Image reconstruction was implemented using the Non-Uniform Fast Fourier Transform (NUFFT)

of type 1 described in Refs. [78] and [31]. The sampling density compensation was applied to the signal prior to gridding by multiplying it by Voronoi weights (MATLAB function *voronoi*) as done in Ref. [38].

Images from individual coils reconstructed following spectral compression can present some aliasing artifacts in regions of low signal intensity as described in Ref. [71] (Fig. 4.4), but are greatly reduced in the final combined image which is visually indistinguishable from that obtained using the full signal dataset. Some ghosting can also be present in images where the bit depth has been reduced excessively. Therefore, image quality comparisons between original and compressed images were carried out by calculating the artifact power (AP) according to the definition of Park et al. [79]

$$AP = \frac{\sum_j \left| \left| I_j^{ref} \right| - \left| I_j^{test} \right| \right|^2}{\sum_j \left| I_j^{ref} \right|^2}, \tag{4.7}$$

where j is the pixel index, I_{ref} is the reference image (the original uncompressed image), and I_{test} is the compressed image.

The amount of memory (in bytes) occupied by the compressed dataset used to reconstruct each image was calculated in the same manner as Wei et al. [59],

$$\text{Memory} = (\#\text{bits/samples}) \times (\#\text{samples/interleaf}) \times (\#\text{interleaves}) \times (\#\text{coils}) \times 2/8(\text{bits/byte}), \tag{4.8}$$

where the factor two takes both the real and imaginary components into account.

4.3 Simulation

To evaluate the effect of demodulation and downsampling under various conditions, a numerical grid phantom similar to that used in the experiments was designed in MATLAB. Coil sensitivity profiles were generated using the empirical expression

$$C(x, y) = K e^{\alpha \sqrt{(x-x_0)^2 + (y-y_0)^2}}, \tag{4.9}$$

where (x_0, y_0) is the location of each coil (arranged circularly around the phantom), K is a normalization constant, and the parameter α was chosen to yield a profile with a reduction in image intensity at the other end of the FOV similar to that of the six-channel head array coil used in the experiment (Fig. 4.5). The centre of each coil's sensitive region was found by calculating the weighted centroid of each profile. Figure 4.5(a) shows a profile

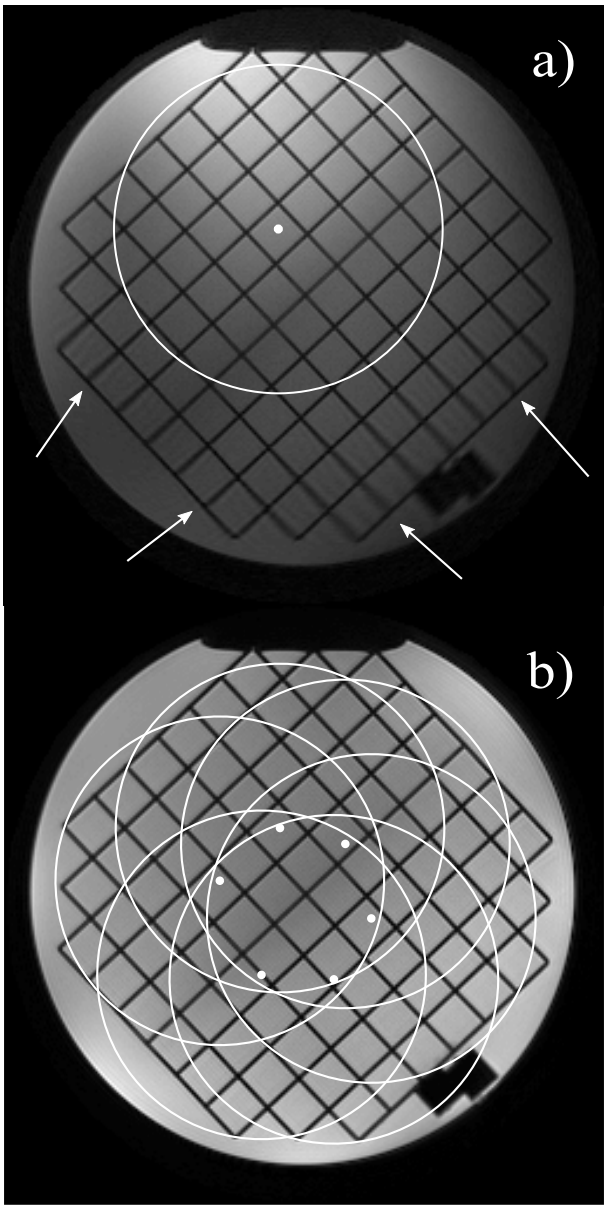

Figure 4.4: (a) Phantom image from a single coil reconstructed after dynamic demodulation (center off-set indicated by small circle), antialias filtering and downsampling with $M = 0.55$. Aliasing artifacts (arrows) are visible only in the region outside the reduced FOV (circled) where the coils sensitivity is small. When all coil images are combined using RSS (b), overlap in individual reduced FOVs ensures that no deterioration in image quality can be observed.

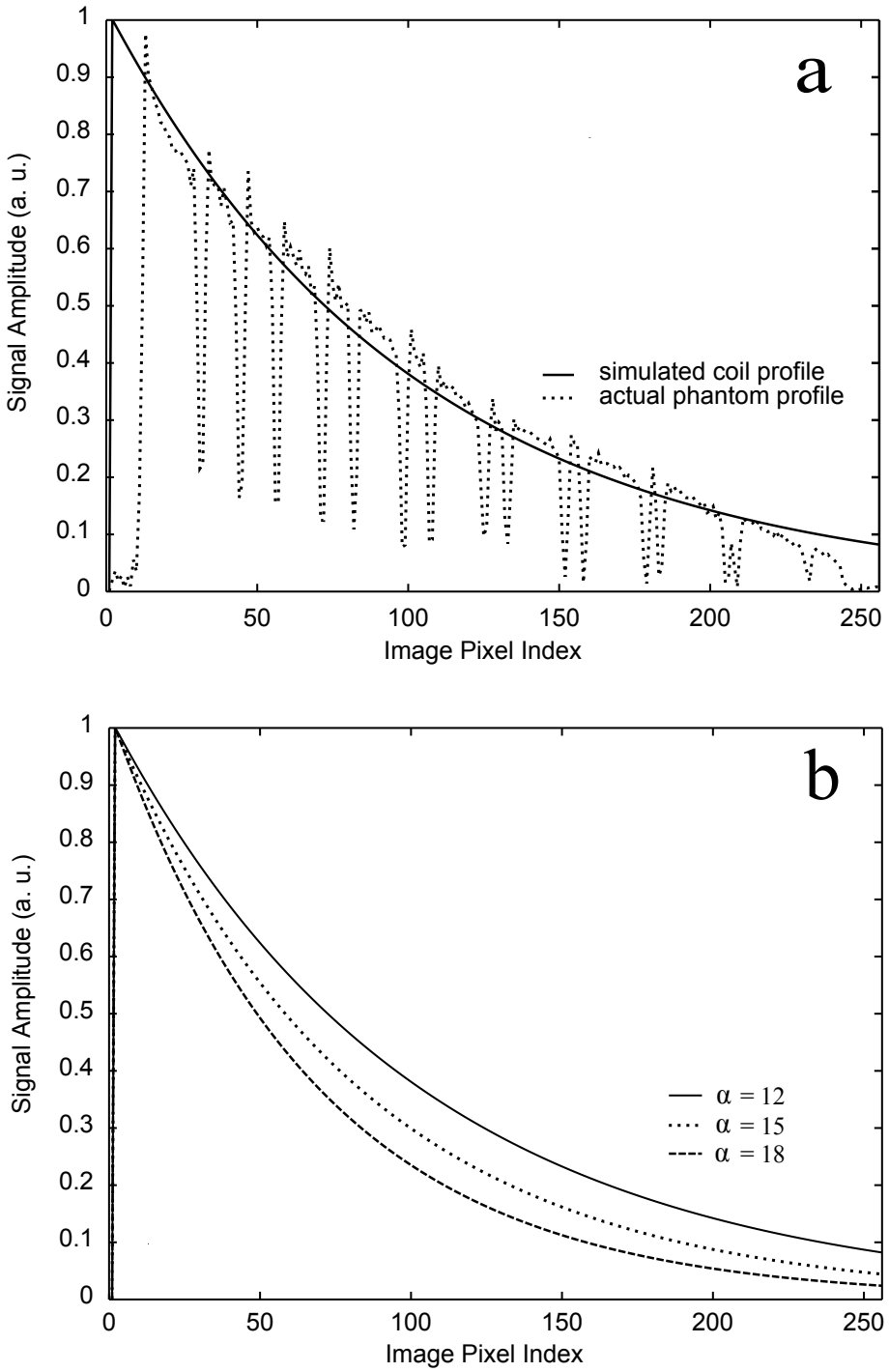

Figure 4.5: (a) Simulated image profile along the coil axis from Eq. (4.9) ($\alpha = 12$) superposed on an actual phantom image profile from one coil. (b) Image profiles and corresponding values for α used to simulate arrays of 8, 12, and 16 coils, respectively.

through an actual single-coil image of a test phantom, superposed with the corresponding simulated image used in the simulations, for an eight-coil array and $\alpha = 12$. Spiral sampling parameters were the same as those used in the actual scans (see §4.4). Nonuniform sampling of the numerical phantom in the frequency domain was performed using the NUFFT type-2 algorithm which converts a discrete Cartesian object to its κ-space representation along an arbitrary trajectory [31, 78]. White Gaussian noise with an intensity equal to 2% of the mean signal amplitude was added, yielding a central image SNR ≈ 50 following reconstruction which is comparable to the experimental images described below.

The effect of the number of coils and their sensitivity profiles on compressed image quality was assessed using two additional sensitivity profiles with $\alpha = 15$ and $\alpha = 18$ (Fig. 4.5(b)) for arrays of 12 and 16 coils, respectively. We note that these simulated profiles tend to overestimate the image intensity at the end of the FOV opposite the coil compared to experimental data from high-density arrays [e.g., see Fig. 6(b) of Ref. 12]. Hence the achievable amount of spectral compression in large coil arrays may be greater than that predicted by this simulation. While our simulation is performed with only 12 and 16 coils arranged around the object, these numbers are comparable to the number of coils (~ 20) of a high-density head array (as in Ref. [12]) that would have significant sensitivity in a given slice.

To assess the performance of spectral compression, images were processed in three different ways and combined from the individual channels using RSS. The reference images were reconstructed using the complete dataset without filtering or demodulation. Images with spectral compression were produced according to Fig. 4.1(b) by demodulating the signals from all coils and interleaves according to Eq. (4.4), filtering and downsampling by a ratio M, upsampling, and finally remodulating and reconstructing using NUFFT. The third set of images was obtained with filtering and resampling but without demodulating the signal.

The maximum achievable amount of spectral compression was investigated by calculating AP as a function of $1 - M$ for all three simulated coil profiles ($\alpha = 12$, 15, and 18). Different realizations of noise were used for the reference and compressed images to illustrate the threshold below which compression artifacts cannot be distinguished from the random noise that dominates the AP in this region. This threshold depends on noise level, geometry and contrast in the phantom, number of coils, and the sensitivity profiles. The lowest AP at which artifacts become visible is necessarily above this threshold and also depends on the type of artifact present (whether aliasing, ghosting, etc.). In the case of aliasing artifacts due to spectral compression, in our data an AP of 3.5×10^{-4} (dashed line in Fig. 4.6)

The resulting RSS images obtained for the simulated 16-coil array with $\alpha = 18$ are displayed in Fig. 4.7. Image (b) ($M = 0.45$, i.e., compressed to 45% of the original sampling

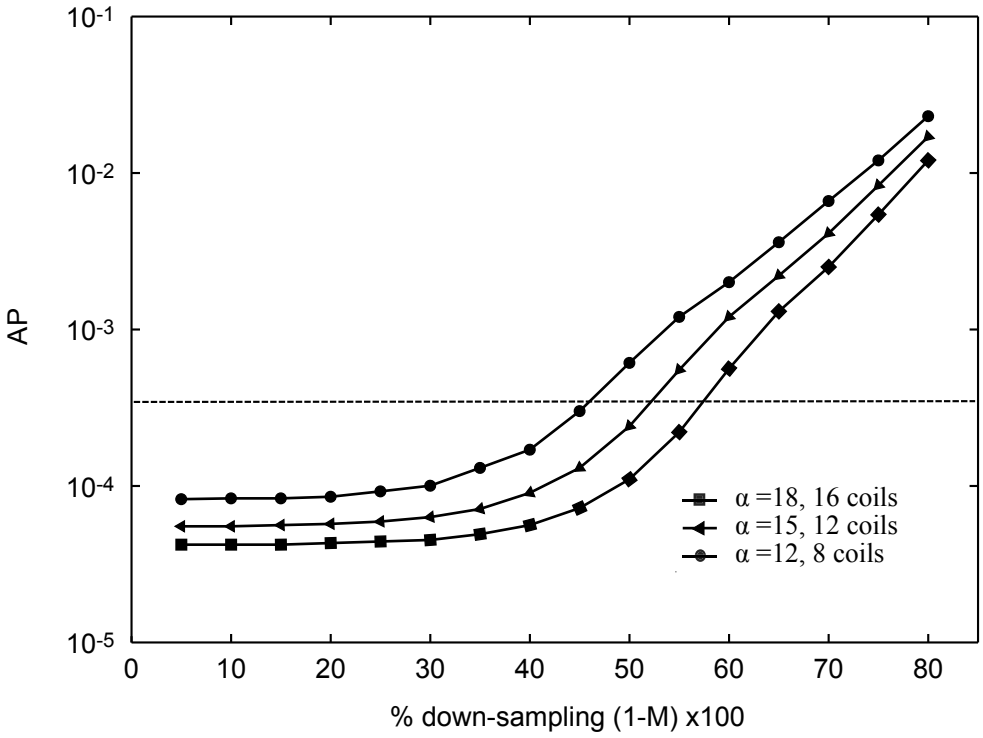

Figure 4.6: Plot of artifact power (AP) versus percent downsampling for the three image profiles of Fig. 4.5(b) with corresponding number of coils evenly distributed in a circular arrangement around the FOV (RSS reconstruction). The effect of noise is included and results in a plateau at low downsampling rates, which forms a lower bound below which compression artifacts cannot be distinguished from the random noise that dominates the AP resulting in no visible artifacts. The largest downsampling factors that did not result in visible aliasing artifacts were $M = 0.55$ for $\alpha = 12$, $M = 0.5$ for $\alpha = 15$, and $M = 0.45$ for $\alpha = 18$, confirming that the more confined sensitivity profiles of higher-density arrays allow for a larger spectral compression while maintaining equivalent image quality.

rate) contains negligible aliasing ($AP = 2.2 \times 10^{-4}$) even though the memory occupied by the data is reduced from 4,404 to 1,982 kB while image (c) is compressed without dynamic demodulation and reveals significant aliasing artifacts ($AP = 6.3 \times 10^{-3}$) even though it is compressed by the same amount.

These results confirm the effectiveness of dynamic demodulation as a spectral compression technique that does not impact image quality, even though some information is lost. This strength lies in the ability to tolerate some distortion beyond each coils reduced FOV where the corresponding sensitivity is negligible. On RSS combination, this distorted signal will be insignificant in comparison to the undistorted signal from other coils that have higher sensitivity in that region. A numerical example from the simulated eight-coil array shows that the sensitivity of some coils is still as high as 20% of the maximum sensitivity at pixels near the edge of the phantom. However, once the images are spectrally compressed and combined by RSS, the images with aliasing at these locations contribute only about 5% of the combined signal and the distortion in the combined image is therefore masked by the stronger contributions of coils that do not have aliasing at these locations.

The noise distribution of the RSS images obtained from spectrally compressed data contains nonuniformities compared to that obtained from the full dataset, with correlation among neighboring pixels (especially at the edges of the FOV) that results from low-pass filtering. In those locations, we also observe an unintuitive increase in SNR as shown in Fig. 4.8 for eight coils and a uniform simulated phantom without a grid. Standard deviation maps were calculated by a Monte-Carlo approach whereby separate realizations of white Gaussian noise are added to the spiral signal in 400 simulations to obtain 400 noisy RSS images. The noise standard deviation of each pixel was then calculated across all 400 images to obtain a map of standard deviations for both the compressed and uncompressed images. A circular averaging filter (pillbox) with a radius of eight pixels was applied to smoothen the random fluctuations in the noise standard standard deviation due to the finite number of simulations used. Figure 4.8(a) shows the inhomogeneous distribution in SNR gains obtained with $M = 0.55$. Figure 4.8(b) shows a cross-section through the center of the phantom of the percent SNR gain for three downsampling factors, where it is evident that greater spectral compression results in greater SNR gains at the periphery of the FOV. This SNR gain comes with a smoothing of the point-spread function, and, hence, a slight loss of image resolution that is measured by the AP above.

4.4 Experiment

A grid phantom was imaged in the transverse plane using a spiral readout on a Philips Achieva 3T scanner (Best, The Netherlands), using a maximum gradient strength of 21

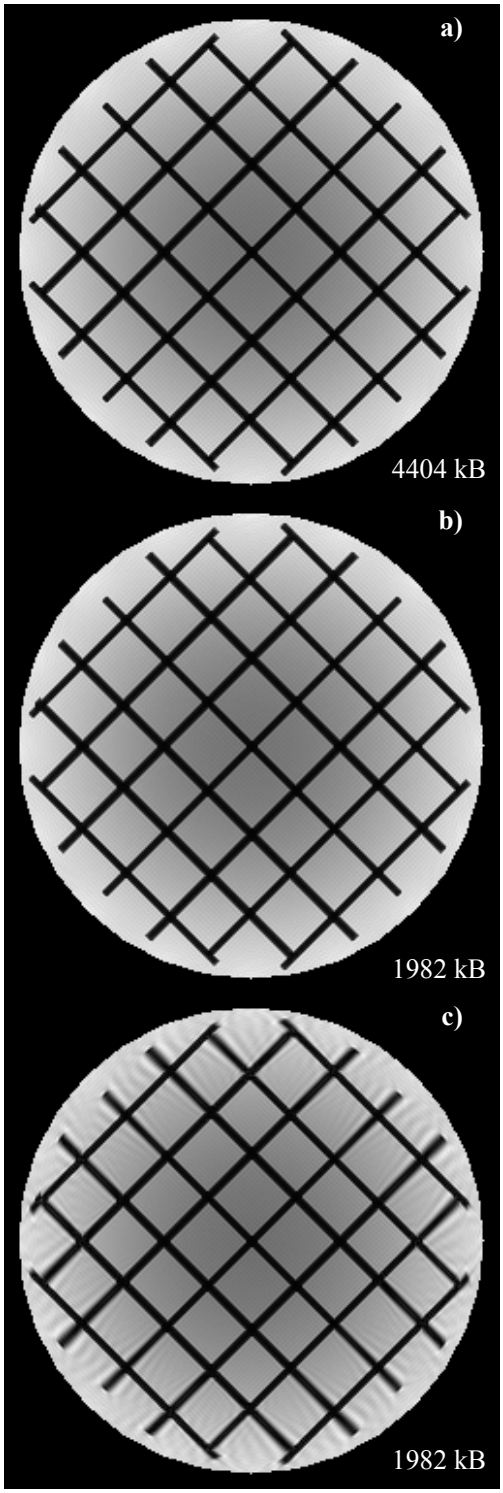

Figure 4.7: Simulated phantom imaged with 16 coils (RSS reconstruction) without spectral compression (a); compressed with a downsampling factor of $M = 0.45$ applied after dynamic demodulation resulting in a negligible $AP = 2.2 \times 10^{-4}$ (b); and without dynamically demodulating the signal prior to downsampling results in readily observed artifacts ($AP = 6.3 \times 10^{-3}$) (c). Amounts of data that must be transmitted are indicated for each image and demonstrate that dynamic demodulation allows substantial levels of artifact-free spectral compression.

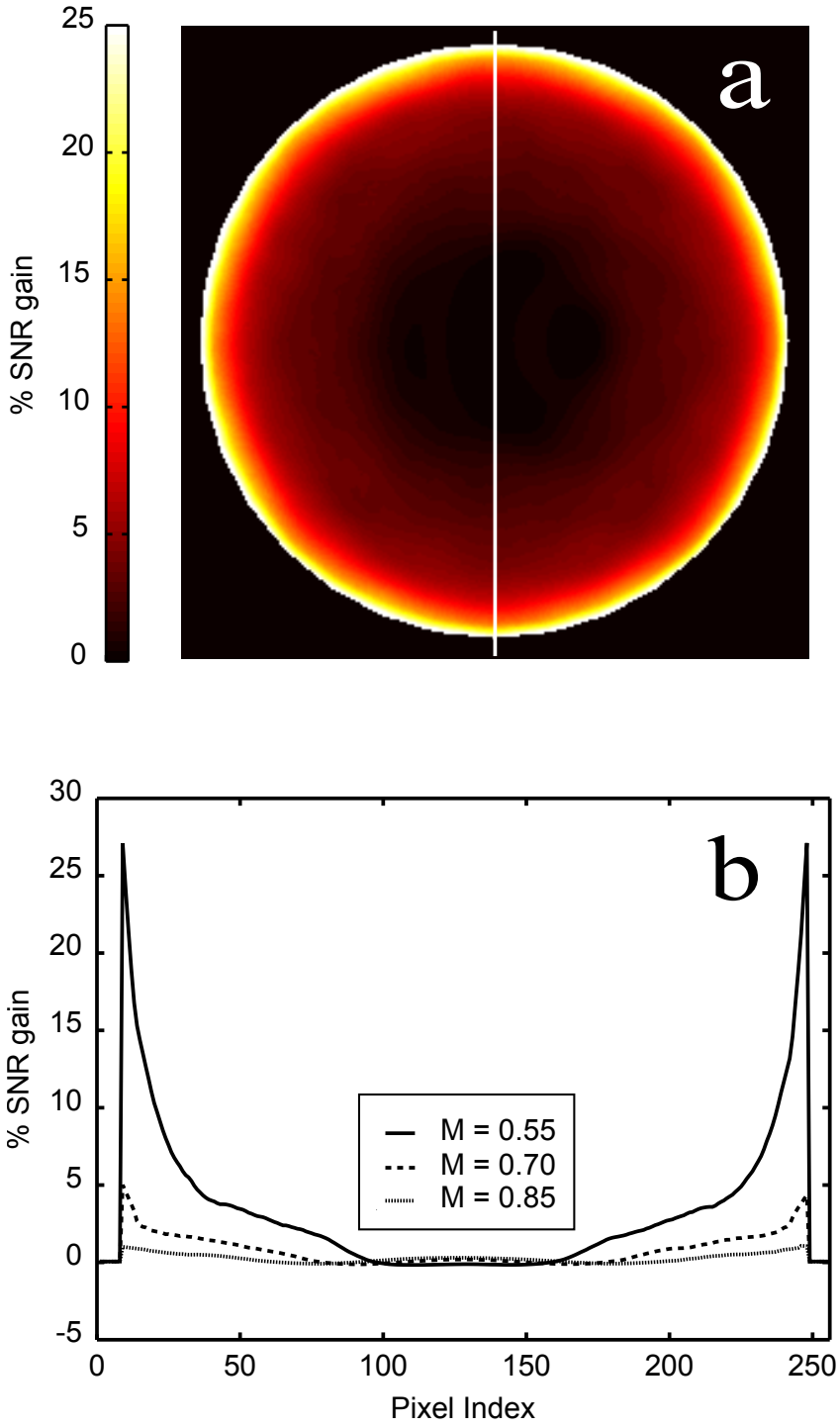

Figure 4.8: Relative SNR gains due to spectral compression in a simulated uniform phantom showing improvements at the periphery of the FOV. (a) Distribution map with downsampling factor $M = 0.55$. (b) Cross-sections of the map along 128th column (vertical line in a) show that SNR gains increase as the amount of undersampling $(1 - M)$ increases. Note that the SNR is essentially unchanged at the centre of the image.

mT/m, slew rate of 100 T/(m s) and a six-channel eight-coil head array (two lateral pairs of elements are combined internally to reduce the number of channels). This low number of channels is expected to yield conservative estimates of spectral compression that will readily be exceeded in truly high-density arrays. The acquisition FOV was 210×210 mm^2, $T_R = 500$ ms, $T_E = 1.39$ ms, with an acquisition matrix of 60 interleaves, each consisting of 1,146 samples (sampling frequency $f_s = 186.17$ kHz). The readout time was kept short (6.156 ms) to minimize blurring due to off-resonance effects; hence no image deblurring was necessary, although image compression does not prevent its application if needed. The raw κ-space data (which already include the demodulation by ω_0 of Fig. 4.1(a)) were processed off-line (Fig. 4.1(b)) using MATLAB to simulate the operations required for data compression.

Results of the compressed images with and without dynamic demodulation, along with the reference image are displayed in Fig. 4.9. Strong aliasing is visible in image (c) where compression was performed without dynamic demodulation. With dynamic demodulation (b), the image is indistinguishable from the reference image (a) even though it was reconstructed using only 55% of the original amount of data. A plot of AP as a function of $1 - M$ for compressed images with and without dynamic demodulation is shown in Fig. 4.10. A threshold level of $AP = 3.5 \times 10^{-4}$ (dashed line) was chosen, allowing a maximum downsampling factor $M = 0.55$, with corresponding $AP = 3.15 \times 10^{-4}$. We note that slightly lower AP values may be obtained by reconstructing the images using an optimal SNR combination [23] (not shown) instead of the more practical RSS combination.

Dynamic range measurements were performed on both the spiral image signal of Fig. 4.9(a), and on Cartesian gradient-echo image data corresponding to the same slice (not shown) with the scanners standard profile-dependent amplification disabled. The dynamic range of the uncompressed spiral dataset varied from 81.9 to 83.7 dB among the six channels, while that of the Cartesian image varied from 74.4 to 77.6 dB. The latter agrees with that of Ref. [66], where Cartesian 2D imaging using various types of coils and imaging protocols resulted in a dynamic range below 82 dB for a similar 3 T scanner. Following sampling density compensation by multiplication with *W(t)*, the dynamic range of the spiral dataset was reduced to values between 54.4 and 56.3 dB (Fig. 4.3(b)).

Bit-depth reduction was applied to both the dynamic-range compressed and the uncompressed spiral datasets by converting the signal samples from MATLAB's standard double-precision data type to signed 16-bit integers and zeroing the $m - k$ least significant bits. The effect of this bit-depth reduction on the phantom images is shown in Figs. 4.11(a,b), where the six least significant bits (one more than that predicted by the reduction in dynamic range) of each signal sample were zeroed prior to image reconstruction. The dynamic range compression in image (a) preserves the image quality following a six-bit reduction, while image (b) suffers from serious ghosting artifacts and blurring. The AP

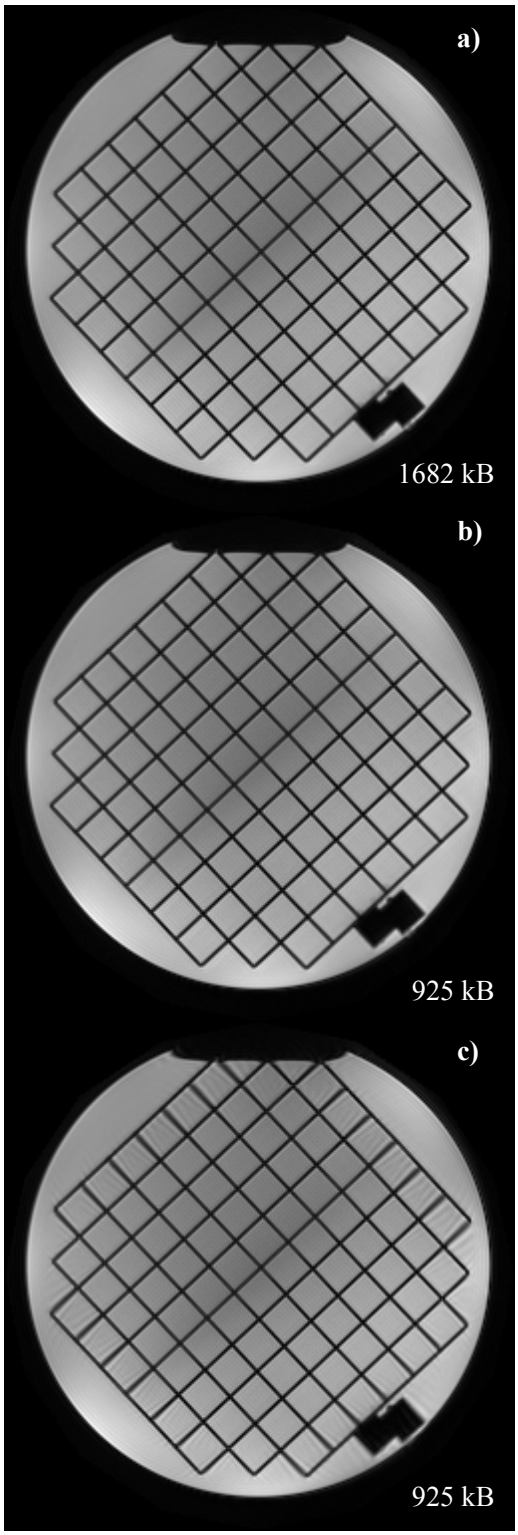

Figure 4.9: Grid phantom imaged with a six-channel array (RSS reconstruction) without spectral compression (a); with a downsampling factor of $M = 0.55$ applied after dynamic demodulation (negligible $AP = 3.15 \times 10^{-4}$) (b); and one without demodulating the signal prior to downsampling (observable $AP = 1.8 \times 10^{-3}$) (c).

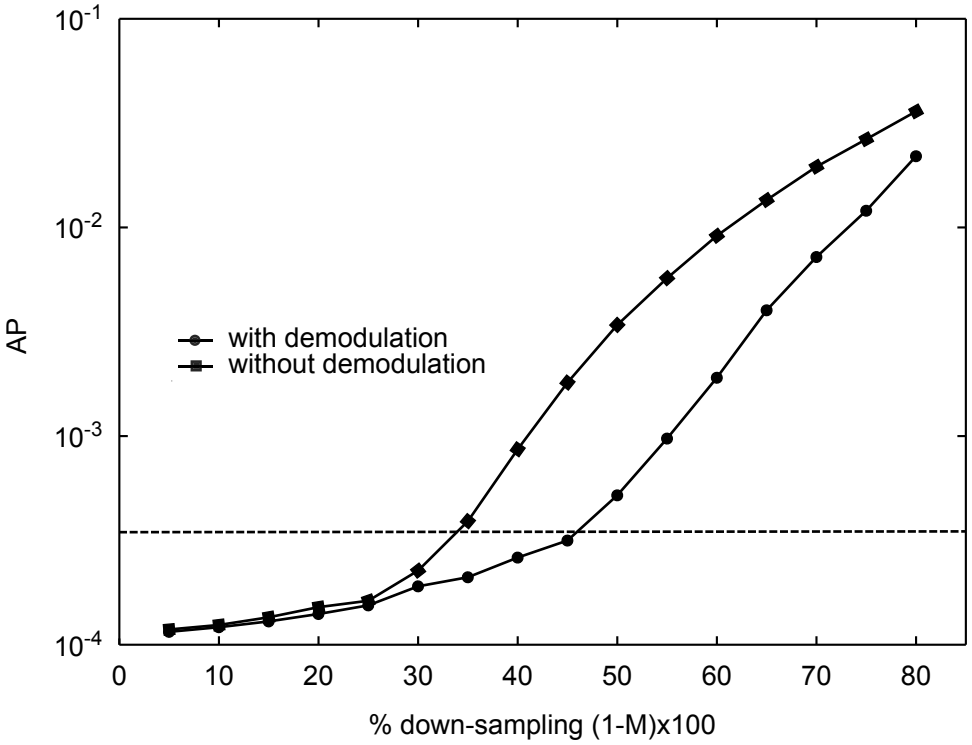

Figure 4.10: Plot of AP versus percent downsampling for spectral compression using dynamic demodulation (circles) and without (squares). The two curves separate where the reduced sampling rate no longer satisfies the Nyquist criterion. Dynamic demodulation is able to support greater compression without loss of image quality.

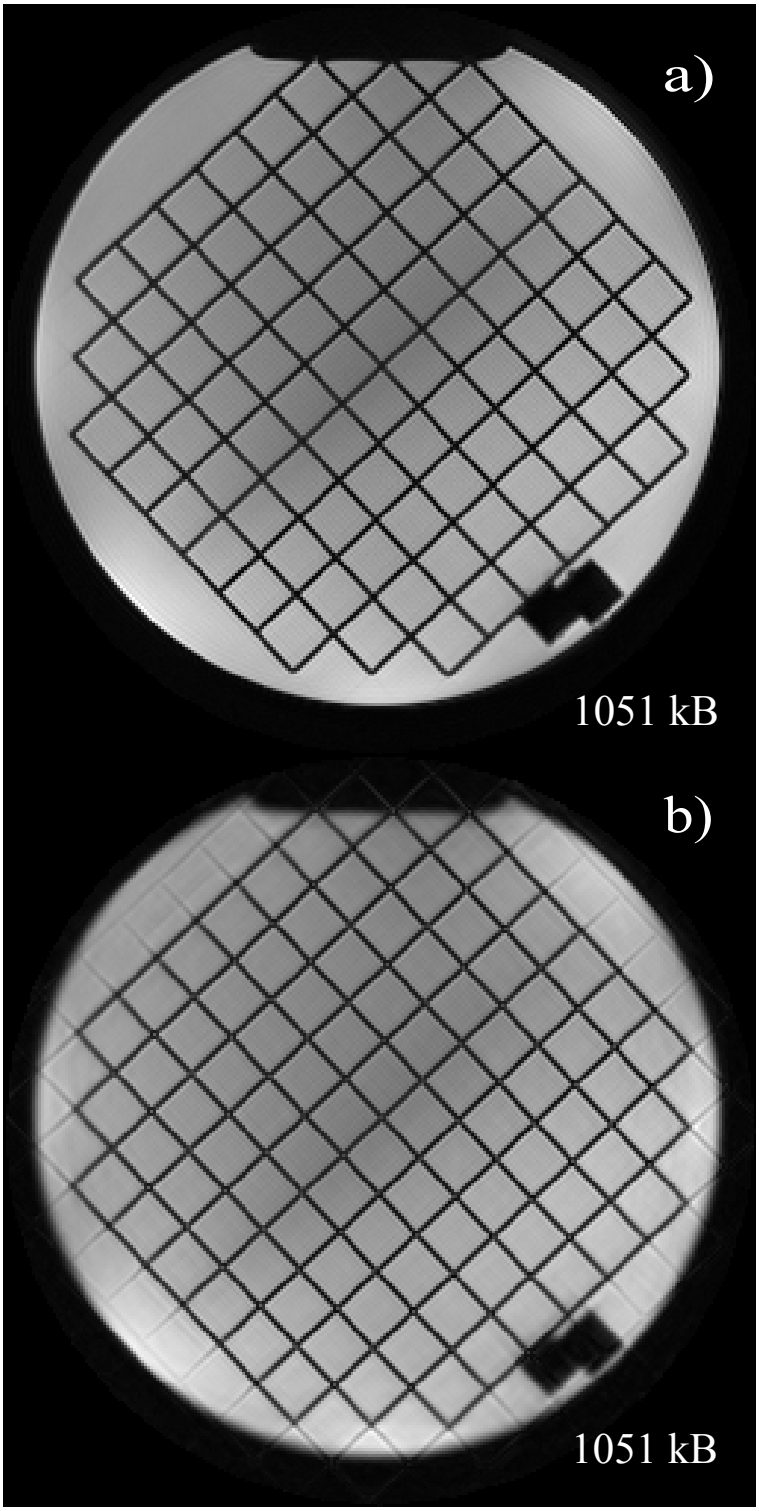

Figure 4.11: Effect of bit-depth reduction (zeroing the six least significant bits of the signal) on an RSS image including dynamic range compression ($AP = 1.69 \times 10^{-4}$) (a) and without dynamic range compression ($AP = 8.0 \times 10^{-3}$) (b), showing considerable ghosting and blurring.

resulting from bit-depth reduction was calculated between a reference image reconstructed from the full dataset (Fig. 4.9(a)), and both compressed and uncompressed images reconstructed following various degrees of bit-depth reduction. The results in Fig. 4.12 indicate that with a threshold $AP = 2 \times 10^{-4}$, a six-bit reduction can be achieved without appreciable loss of image quality, corresponding to a further $6/16 = 37.5\%$ reduction in data in addition to that achieved by spectral compression.

The effect of bit-depth reduction on SNR is shown in Fig. 4.12(b), where we note a small but uniform improvement in SNR ($\sim 4-7.5\%$) if the number of zeroed bits is limited to six or less in this case. While a detailed analysis of this counter-intuitive behavior is beyond the scope of this work, it can be qualitatively explained by noting that zeroing the least significant bits is equivalent to rounding downward, which has a greater relative effect on the amplitude of the noise than on that of the signal. In fact, signal has a shorter temporal duration but larger amplitude than the noise whose standard deviation is constant but small and requires all the least significant bits to be sampled accurately. If the number of zeroed bits increases beyond six, the additional quantization noise is no longer negligible relative to the data's thermal noise and a rapid degradation in SNR occurs. This coincides with the increase in AP since concurrent noise and artifacts cannot be mathematically separated in difference images.

The final image reconstructed following both types of data compression is displayed in Fig. 4.13. The combined AP (3.51×10^{-4}) does not increase significantly above the larger individual AP value when both types of compression are applied to the image while memory requirements decrease by a total of 66% (from 1,682 to 578 kB) to generate an image of equivalent quality.

4.5 Conclusion

Wireless MRI coils will bring benefits including improved patient comfort by allowing more ergonomic "wearable" designs as well as improved safety and cross-talk with the elimination of coaxial cables. Wireless transmission will, however, require efficient data encoding to overcome limitations in data rates, especially in high-density array designs.

In this work, we have analyzed two independent methods of MR data compression that rely on dynamic demodulation to perform spectral compression and sampling density compensation for dynamic range compression. Both are compatible with techniques such as parallel imaging and channel combinations and can also be used to reduce archival data storage requirements in standard MRI systems. Spectral compression takes advantage of the much smaller single-coil FOV compared to the full image FOV and is based on dynamic

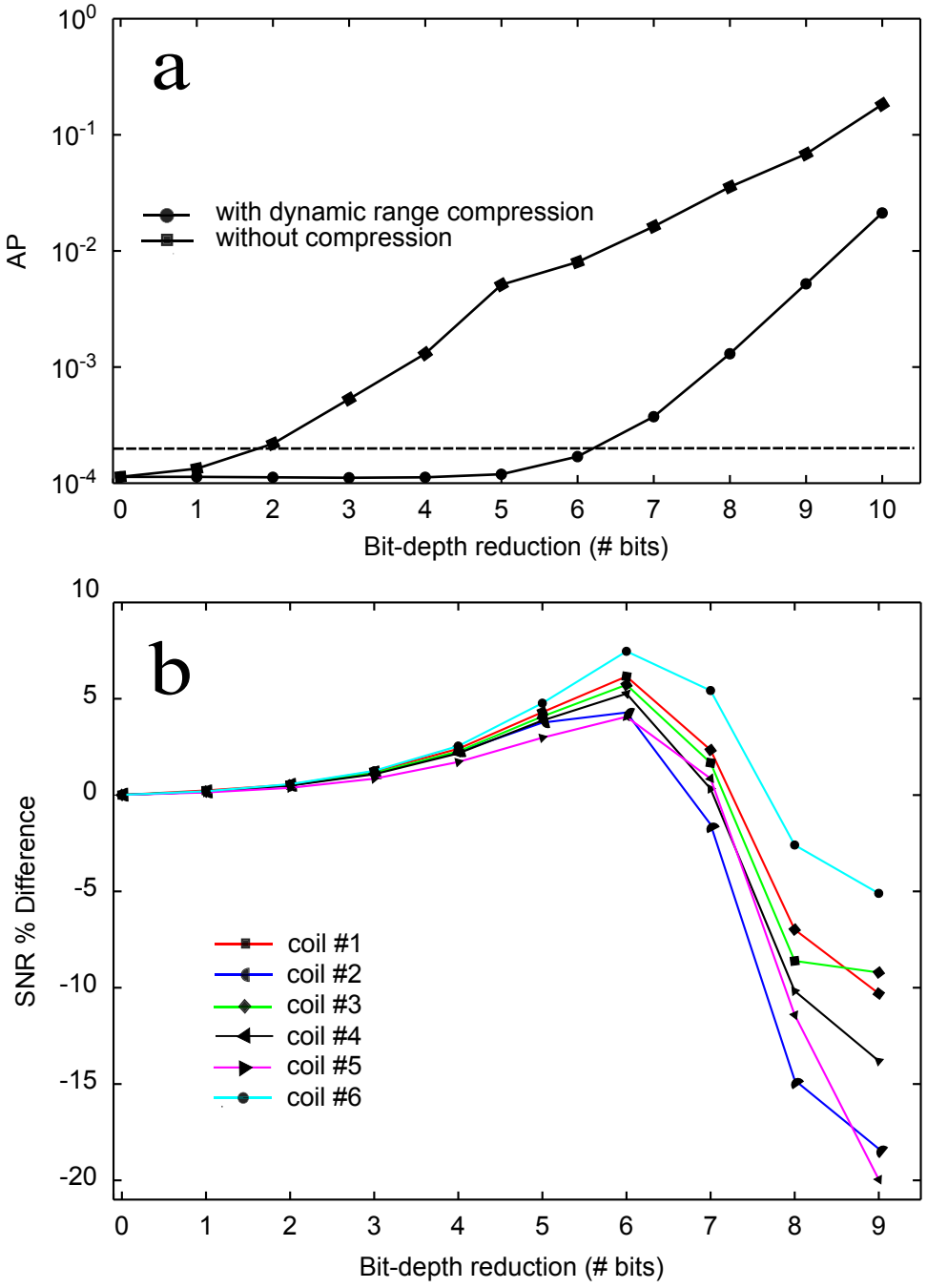

Figure 4.12: In (a), a plot of artifact power versus bit-depth reduction (number of zeroed bits) for the image of Fig. 4.10 with (circles) and without dynamic range compression (squares). In (b), a plot of relative SNR difference between a full bit-depth image and a reduced bit-depth image for various degrees of bit-depth reduction. Slight improvements in SNR are possible due to the rounding effects of setting least-significant bits to zero (see text).

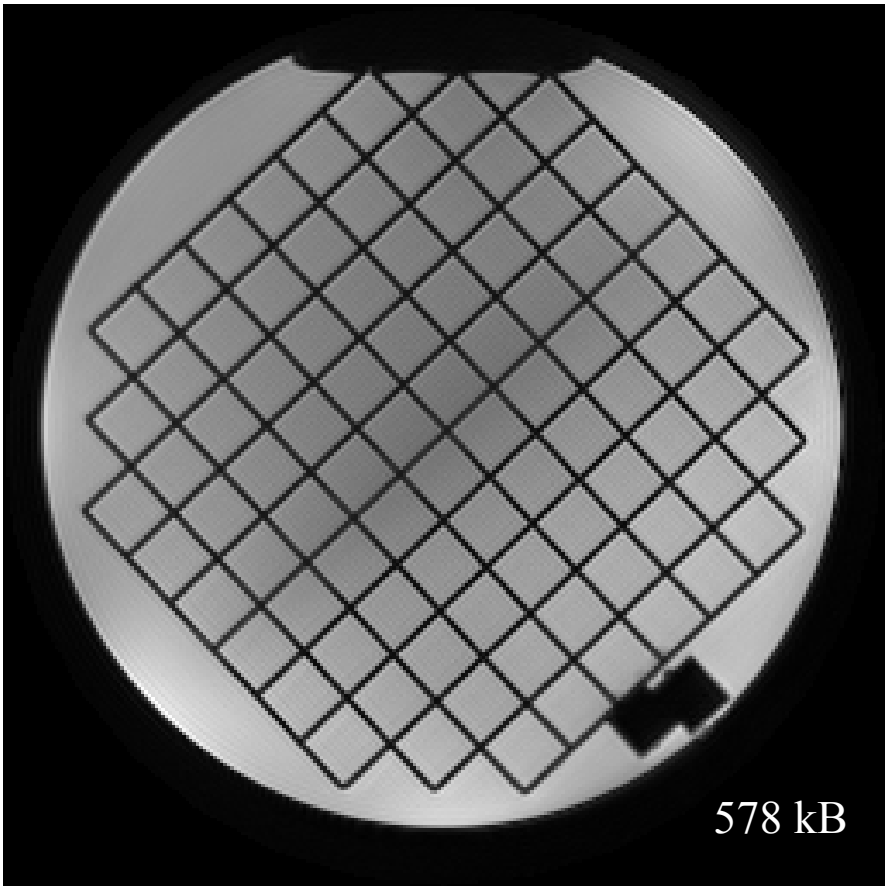

Figure 4.13: RSS image reconstructed using both types of data compression: spectral compression with downsampling $M = 0.55$ and a reduction in bit depth from 16 to 10 bits per scalar sample component. Only 578 kB of data was used in reconstructing the image, compared to the original 1,682 kB of Fig. 4.9(a), hence a 66% decrease in the amount of data is obtained. Artifact power is a negligible 3.51×10^{-4}.

demodulation of the MR signal using a variable carrier frequency that depends on the sampling trajectory in κ-space. Dynamic range compression is implemented by removing the least significant bits of the data following sampling density compensation in the case of non-Cartesian trajectories.

While our calculations were performed by post-processing data acquired from a standard MRI spectrometer, they could equally be performed by dedicated processing devices following direct digitization within dedicated receiver units at each coil (i.e., a "distributed" spectrometer). After transmission through the wireless link, simple recovery operations can retrieve most of the image information without visible degradation in quality.

Our results show that with as few as six channels, a 45% spectral compression can be achieved while maintaining AP to negligible levels and with some improvement in SNR at the periphery of the FOV. With more coils and more localized coil sensitivity profiles, higher compression factors are achievable. Dynamic range compression followed by bit-depth reduction yielded a further 37.5% reduction in data with a slight increase in SNR over the full FOV. When combined the two approaches result in a data set of only one-third the original size with a negligible impact on image quality.

While the methods in this work were applied to spiral κ-space trajectories, they are equally applicable to Cartesian trajectories, in which case the density compensation function can be replaced by a heuristic function (including profile-dependent amplification) or nonlinear compression. Spiral or other radially symmetric trajectories, however, offer better compression properties than Cartesian trajectories in common cases where coil elements are arranged in an approximately circular pattern around the FOV.

Implementation of these algorithms in a distributed wireless spectrometer is still years away. Remaining engineering challenges include in silico implementation of the compression methods and miniaturization; power delivery and cooling of the digital acquisition modules required for each coil; synchronization to the timings of the main imaging sequence; and choice of a robust, high-capacity wireless transmission technology that is reliable in the hostile electromagnetic environment of an MRI scanner bore.

CHAPTER 5

Conclusion

The purpose of this project was to demonstrate the efficient data acquisition, transmission and post-processing of spiral MRI for obtaining high-quality images (i.e., high SNR, resolution, and geometrical accuracy). The first step towards quality spiral MR images involves carefully selecting appropriate scan parameters given the desired resolution and image size. If the static magnetic field is not sufficiently shimmed, it may be necessary to acquire an additional spiral scan at two different echo-times for the purpose of obtaining an off-resonance map. The map can be unwrapped efficiently in 2D and used with a FSORC algorithm for deblurring the spiral images. A number of tips were provided for reducing both the total scan time and the image post-processing time when dealing with a large spiral MRI dataset, such as would be typical of a RTP MRI-based exam.

The second result of this thesis is a simulated study of the compressibility of spiral MRI data transmitted from a high-density array. This research was motivated by the present technological push towards high-density detector arrays, which can achieve higher SNR or reduced scan time, but also come with more stringent data storage and transmission speed requirements. Traditional analog transmission by coaxial cables becomes less suitable with an increasing number of channels, due to bulkiness and possible cable-to-cable interference, making digital transmission by optical fiber or wireless links a better alternative. Two types of data compression methods were investigated. The first, known as spectral compression, exploits the finite sensitivity region of the coil to reduce the bandwidth by assigning a separate FOV to each coil, which is equivalent to sampling κ-space using coarser spacing $\Delta\kappa$. The total required amount of data is reduced by almost half without affecting the image quality. The second method exploits the non-uniform sampling density pattern of the spiral acquisition, using the sampling density compensation as a inherent non-linear gain for compressing the dynamic range of the signal. The dynamic range of the transmitted signal

may thus be compressed from 16 to 10 bits without resulting in any image degradation. Combining both types of compression could reduce the data by 66% for a 6-channel array coil, and by up to 75% for a 16-channel array coil, which would be greatly beneficial in wireless data transmission, which supports much lower bit-rates than optical fiber cables.

Bibliography

[1] M. A. Bernstein, K. F. King, and X. Joe Zhou. *Handbook of MRI Pulse Sequences*. Elservier Academic Press, 2004.

[2] K. Herrlin, L. Bi Ling, H. Pettersson, H. Willen, and A. Rydholm. Gadolinium-DPTA enhancement of soft tissue tumors in magnetic resonance imaging. *Acta Radiologica*, 31:233–236, 1990.

[3] S. Peungjesada, P. R. Bhosale, A. Balachandran, and R. B. Iyer. Magnetic resonance imaging of endometrial carcinoma. *Journal of Computer-Assisted Tomography*, 33:601–608, 2009.

[4] C. S. Kidwell, J. A. Chalela, J. L. Saver, S. Starkman, M. D. Hill, A. M. Demchuk, J. A. Butman, N. Patronas, J. R. Alger, L. L. Latour, M. L. Luby, A. E. Baird, M. C. Leary, M. Tremwel, B. Ovbiagele, A. Fredieu, S. Suzuki, J. P. Villablanca, S. Davis, B. Dunn, J. W. Todd, M. A. Ezzeddine, J. Haymore, J. K. Lynch, L. Davis, and S. Warach. Comparison of MRI and CT for detection of acute intercerebral hemorrhage. *Journal of the American Medical Association*, 292:1823–1830, 2004.

[5] A. Techawiboonwong, H. K. Song, M. B. Leonard, and F. W. Wehrli. Cortical bone water:In vivo quantification with ultrashort echo-time MR imaging. *Radiology*, 248(3):824–833, 2008.

[6] A-K. Bracher, C. Hofmann, A. Bornstedt, E. Hell, J. Ulrici, B. Haller, and V. Rasche. Accurate in vivo assessment of caries lesion extent by UTE MRI. In *Annual Meeting of the International Society for Magnetic Resonance in Medicine, Montreal*, page 2611, 2011.

[7] T. Stanescu, H. S. Jans, K. Wachowicz, and B. G. Fallone. Investigation of a 3D system distortion correction method for MR images. *Journal of Applied Clinical Medical Physics*, 11:2961, 2010.

[8] L. N. Baldwin, K. Wachowicz, S. D. Thomas, R. Rivest, and B. G. Fallone. Characterization, prediction and correction of geometric distortion in 3T MR images. *Medical Physics*, 34:388–399, 2007.

[9] A. Johansson, M. Karlsson, and T. Nyholm. CT substitute derived from MRI sequences with ultrashort echo time. *Medical Physics*, 38:2708–2714, 2011.

[10] M. Schmitt, A. Potthast, D. E. Sosnovik, J. R. Polimeni, G. C. Wiggins, C. Triantafyllou, and L. L. Wald. A 128-channel receive-only cardiac coil for highly accelerated cardiac MRI at 3 tesla. *Magnetic Resonance in Medicine*, 59:1431–1439, 2008.

[11] C. J. Hardy, R. O. Giaquinto, J. E. Piel, K. W. Rohling, L. Marinelli, D. J. Blezek, E. W. Fiveland, R. D. Darrow, and T. K. Foo. 128-channel body MRI with a flexible high-density receiver-coil array. *Journal of Magnetic Resonance Imaging*, 28:1219–1225, 2008.

[12] G. C. Wiggins, J. R. Polimeni, A. Potthast, M. Schmitt, V. Alagappan, and L. L. Wald. 96-channel receive-only head coil for 3 tesla: Design optimization and evaluation. *Magnetic Resonance in Medicine*, 62:754–762, 2009.

[13] I. I. Rabi, J. R. Zacharias, S. Millman, and P. Kusch. A new method of measuring nuclear magnetic moment. *Physical Review*, 53(4):318, 1938.

[14] E. M. Haacke, R. W. Brown, M. R. Thompson, and R. Venkatesan. *Magnetic Resonance Imaging Physical Principles and Sequence Design*. John Wiley & Sons, Canada, 1999.

[15] R. R. Ernst and W. A. Anderson. Application of Fourier transform spectroscopy to magnetic resonance. *Review of Scientific Instruments*, 37(1):93, 1966.

[16] J. Mattson and M. Simon. *The pioneers of NMR and magnetic resonance in medicine: The story of MRI*. Bar-Ilan University Press, Israel, 1996.

[17] P. C. Lauterbur. Image formation by induced local interactions:Examples employing nuclear magnetic resonance. *Nature*, 242(5394):190–191, 1973.

[18] P. Mansfield. Multi-planar image: Formation using NMR spin echoes. *Journal of Physics C-Solid State Physics*, 10(3):L55–L58, 1977.

[19] D. J. Griffiths. *Introduction to Quantum Mechanics*. Pearson Education, Upper Saddle River, NJ, 2nd edition, 2005.

[20] C. P. Slichter. *Principles of Magnetic Resonance*. Springer-Verlag, Berlin, Germany, 1978.

[21] D. B. Twieg. The k-trajectory formulation of the NMR imaging process with applications in analysis and synthesis of imaging methods. *Medical Physics*, 10(5):610–621, 1983.

[22] O. Ocali and E. Atalar. Ultimate intrinsic SNR in MRI. *Magnetic Resonance in Medicine*, 39:462–473, 1998.

[23] P. B. Roemer, W. A. Edelstein, C. E. Hayes, S. P. Souza, and O. M. Mueller. The NMR phased-array. *Magnetic Resonance in Medicine*, 16:192–225, 1990.

[24] C. H. Meyer, B. S. Hu, D. G. Nishimura, and A. Macovski. Fast spiral coronary artery imaging. *Magnetic Resonance in Medicine*, 28:202–213, 1992.

[25] K. T. Block and J. Frahm. Spiral imaging: A critical appraisal. *Journal of Magnetic Resonance Imaging*, 21:657–668, 2005.

[26] B. M. Delattre, R. M. Heidemann, L. A. Crowe, J. P. Vallee, and J. N. Hyacinthe. Spiral demystified. *Magnetic Resonance Imaging*, 28:862–881, 2010.

[27] P. Bornert, M. Stuber, R. M. Botnar, K. V. Kissinger, P. Koken, E. Spuentrup, and W. J. Manning. Direct comparison of 3D spiral vs Cartesian gradient-echo coronary magnetic resonance angiography. *Magnetic Resonance in Medicine*, 46:789–794, 2001.

[28] M. Klarhofer, M. Barth, and E. Moser. Comparison of multi-echo spiral and echo planar imaging in functional MRI. *Magnetic Resonance Imaging*, 20:359–364, 2002.

[29] P. Bornert, H. Schomberg, B. Aldefeld, and J. Groen. Improvements in spiral MR imaging. *MAGMA*, 9:29–41, 1999.

[30] K. F. King, A. Ganin, X. J. Zhou, and M. A. Bernstein. Concomitant gradient field effects in spiral scans. *Magnetic Resonance in Medicine*, 41:103–112, 1999.

[31] L. Greengard and J. Y. Lee. Accelerating the nonuniform fast Fourier transform. *SIAM Review*, 46:443–454, 2004.

[32] A. Dutt and V. Rokhlin. Fast fourier transforms for nonequispaced data. *SIAM Journal of Scientific Computing*, 14:1368–1393, 1993.

[33] J. D. O'Sullivan. A fast sinc function gridding algorithm for fourier inversion in computer tomography. *IEEE Transactions on Medical Imaging*, 4:200–207, 1985.

[34] J. I. Jackson, C. H. Meyer, D. G. Nishimura, and A. Macovski. Selection of a convolution function for Fourier inversion using gridding. *IEEE Transactions on Medical Imaging*, 10:473–478, 1991.

[35] G. E. Sarty, R. Bennett, and R. W. Cox. Direct reconstruction of non-Cartesian k-space data using a nonuniform fast Fourier transform. *Magnetic Resonance in Medicine*, 45:908–915, 2001.

[36] J. G. Pipe and P. Menon. Sampling density compensation in MRI: Rationale and an iterative numerical solution. *Magnetic Resonance in Medicine*, 41:179–186, 1999.

[37] D. Mitsouras, R. V. Mulkern, and F. J. Rybicki. Fast, exact k-space sample density compensation for trajectories composed of rotationally symmetric segments, and the SNR-optimized image reconstruction from non-Cartesian samples. *Magnetic Resonance in Medicine*, 60:339–349, 2008.

[38] V. Rasche, R. Proksa, R. Sinkus, P. Bornert, and H. Eggers. Resampling of data between arbitrary grids using convolution interpolation. *IEEE Transactions on Medical Imaging*, 18:385–392, 1999.

[39] F. Aurenhammer. Voronoi diagrams: A survey of a fundamental data structure. *ACM Computing Surveys*, 23:345–405, 1991.

[40] J.-Y. Lee and L. Greengard. The type 3 non-uniform FFT and its applications. *Journal of Computational Physics*, 206:1–5, 2005.

[41] L. N. Baldwin, K. Wachowicz, and B. J. Fallone. A two-step scheme for distortion rectification of magnetic resonance images. *Medical Physics*, 36:3917–3926, 2009.

[42] L. C. Man, J. M. Pauly, and A. Macovski. Multifrequency interpolation for fast off-resonance correction. *Magnetic Resonance in Medicine*, 37:785–792, 1997.

[43] D. C. Noll, C. H. Meyer, J. M. Pauly, D. G. Nishimura, and A. Macovski. A homogeneity correction method for magnetic resonance imaging with time-varying gradients. *IEEE Transactions on Medical Imaging*, 10:629–637, 1991.

[44] W. Chen and C. H. Meyer. Fast automatic linear off-resonance correction method for spiral imaging. *Magnetic Resonance in Medicine*, 56:457–462, 2006.

[45] H. Eggers, T. Knopp, and D. Potts. Field inhomogeneity correction based on gridding reconstruction for magnetic resonance imaging. *IEEE Transactions on Medical Imaging*, 26:374–384, 2007.

[46] M. K. Makhijani and K. S. Nayak. Exact correction of sharply varying off-resonance effects in spiral MRI. *2006 3rd IEEE International Symposium on Biomedical Imaging: Macro to Nano, Vols 1-3*, pages 730–733, 2006.

[47] H. Moriguchi, B. M. Dale, J. S. Lewin, and J. L. Duerk. Block regional off-resonance correction (BRORC): A fast and effective deblurring method for spiral imaging. *Magnetic Resonance in Medicine*, 50:643–648, 2003.

[48] W. Chen, C. T. Sica, and C. H. Meyer. Fast conjugate phase image reconstruction based on a Chebyshev approximation to correct for B0 field inhomogeneity and concomitant gradients. *Magnetic Resonance in Medicine*, 60:1104–1111, 2008.

[49] D. C. Noll, J. M. Pauly, C. H. Meyer, D. G. Nishimura, and A. Macovski. Deblurring for non-2D Fourier transform magnetic resonance imaging. *Magnetic Resonance in Medicine*, 25:319–333, 1992.

[50] E. Schneider and G. Glover. Rapid in vivo proton shimming. *Magnetic Resonance in Medicine*, 18:335–347, 1991.

[51] W. Chen and C. H. Meyer. Semiautomatic off-resonance correction in spiral imaging. *Magnetic Resonance in Medicine*, 59:1212–1219, 2008.

[52] R. M. Goldstein, H. A. Zebken, and C. L. Werner. Satellite radar interferometry: Two-dimentional phase unwrapping. *Radio Science*, 23:713–720, 1988.

[53] D. C. Ghiglia and M. D. Pritt. *Two-Dimentional Phase Unwrapping: Theory, Algorithms and Software*. Wiley-Interscience, New York, 1998.

[54] T. Stanescu, H. S. Jans, N. Pervez, P. Stavrev, and B. G. Fallone. A study on the magnetic resonance imaging (MRI)-based radiation treatment planning of intracranial lesions. *Physics in Medicine and Biology*, 53:3579–3593, 2008.

[55] J.-D. Jutras, B. G. Fallone, and N. De Zanche. Efficient multichannel coil data compression: A prospective study for distributed detection in wireless high-density arrays. *Concepts in Magnetic Resonance Part B*, 39B:64–77, 2011.

[56] D. K. Sodickson and W. J. Manning. Simultaneous acquisition of spatial harmonics (SMASH): Fast imaging with radiofrequency coil arrays. *Magnetic Resonance in Medicine*, 38:591–603, 1997.

[57] K. P. Pruessmann, M. Weiger, M. B. Scheidegger, and P. Boesiger. SENSE: Sensitivity encoding for fast MRI. *Magnetic Resonance in Medicine*, 42:952–962, 1999.

[58] M. A. Griswold, P. M. Jakob, R. M. Heidemann, M. Nittka, V. Jellus, J. Wang, B. Kiefer, and A. Haase. Generalized autocalibrating partially parallel acquisitions (GRAPPA). *Magnetic Resonance in Medicine*, 47:1202–1210, 2002.

[59] J. Wei, Z. Liu, Z. Chai, J. Yuan, J. Lian, and G. X. Shen. A realization of digital wireless transmission for MRI signals based on 802.11b. *Journal of Magnetic Resonance*, 186:358–363, 2007.

[60] S. B. King, S. M. Varosi, and G. R. Duensing. Eigenmode analysis for undersampling phased array coils and their limits. *Concepts in Magnetic Resonance Part B*, 29B:42–49, 2006.

[61] M. Buehrer, K. P. Pruessmann, P. Boesiger, and S. Kozerke. Array compression for MRI with large coil arrays. *Magnetic Resonance in Medicine*, 57:1131–1139, 2007.

[62] H. Fujita. New horizons in MR technology: RF coil designs and trends. *Magnetic Resonance in Medical Sciences*, 6:29–42, 2007.

[63] G. Scott and K. Yu. Wireless transponders for RF coils: Systems issues. In *13th Annual Meeting of the International Society for Magnetic Resonance in Medicine, Miami*, page 330, 2005.

[64] J. Yuan, J. Wei, and G. X. Shen. A direct modulated optical link for MRI RF receive coil interconnection. *Journal of Magnetic Resonance*, 189:130–138, 2007.

[65] W. S. Yamanashi, M. A. Nyman, C. M. Luke, and P. D. Lester. Preliminary study on the use of fiberoptics in the coil to receiver linkage. In *Annual Meeting of the International Society for Magnetic Resonance in Medicine, San Fransisco*, page 860, 1988.

[66] R. E. Gabr, M. Schar, A. D. Edelstein, D. L. Kraitchman, P. A. Bottomley, and W. A. Edelstein. MRI dynamic range and its compatibility with signal transmission media. *Journal of Magnetic Resonance*, 198:137–145, 2009.

[67] G. Giovannetti, V. Hartwig, V. Viti, G. Gaeta, R. Francesconi, L. Landini, and A. Benassi. Application of undersampling technique for the design of an NMR signals digital receiver. *Concepts in Magnetic Resonance Part B*, 29B:107–114, 2006.

[68] J. A. Massner, N. De Zanche, and K. P. Pruessmann. Stretchable coil arrays. In *15th Annual Meeting of the International Society for Magnetic Resonance in Medicine, Berlin*, page 1051, 2007.

[69] P. Perez, A. Santos, and J. J. Vaquero. Potential use of the undersampling technique in the acquisition of nuclear magnetic resonance signals. *MAGMA*, 13:109–117, 2001.

[70] M. Kasal, J. Halamek, and V. Husek. Signal processing in transceivers for nuclear magnetic resonance. *Review of Scientific Instrumentation*, 65:1897–1902, 1994.

[71] J. H. Lee, G. C. Scott, J. M. Pauly, and D. G. Nishimura. Broadband multicoil imaging using multiple demodulation hardware: A feasibility study. *Magnetic Resonance in Medicine*, 54:669–676, 2005.

[72] M. A. Griswold, P. M. Jakob, M. Nittka, J. W. Goldfarb, and A. Haase. Partially parallel imaging with localized sensitivities (PILS). *Magnetic Resonance in Medicine*, 44:602–609, 2000.

[73] V. J. Wedeen, Y. S Chao, and J. L. Ackerman. Dynamic range compression in MRI by means of a nonlinear gradient pulse. *Magnetic Resonance in Medicine*, 6:287–295, 1988.

[74] Y. Otake, K. Kose, and T. Haish. A solution to the dynamic range problem in MRI using a parallel image acquisition. *Concepts in Magnetic Resonance Part B*, 29B:161–167, 2006.

[75] S. Biber, P. Baureis, J. Bollenbeck, P. Hocht, and H. Fischer. Analog optical transmission of 4 MRI receive channels with high dynamic range over one single optical fiber. In *16th Annual Meeting of the International Society for Magnetic Resonance in Medicine, Toronto*, page 1120, 2008.

[76] C. H. Oh, Y. C. Ryu, J. H. Hyun, S. H. Bae, S. T. Chung, H. W. Park, and Y. G. Kim. Dynamic range expansion of receiver by using optimized gain adjustment for high-field MRI. *Concepts in Magnetic Resonance Part A*, 36A:243–254, 2010.

[77] V. Rasche, R. W. de Boer, D. Holz, and R. Proksa. Continuous radial data acquisition for dynamic MRI. *Magnetic Resonance in Medicine*, 34:754–761, 1995.

[78] N. Nguyen and Q. H. Liu. The regular Fourier matrices and nonuniform fast Fourier transforms. *Siam Journal on Scientific Computing*, 21:283–293, 1999.

[79] J. Park, Q. Zhang, V. Jellus, O. Simonetti, and D. Li. Artifact and noise suppression in GRAPPA imaging using improved k-space coil calibration and variable density sampling. *Magnetic Resonance in Medicine*, 53:186–193, 2005.